



INSTITUTO SUPERIOR TÉCNICO
Universidade Técnica de Lisboa



Design and construction of a multi-rotor with various degrees of freedom

Nelson dos Santos Fernandes

Dissertação para a obtenção de Grau de Mestre em
Engenharia Aeroespacial

Júri

Presidente: Prof. Fernando José Parracho Lau

Orientador: Prof. Filipe Szolnoky Ramos Pinto Cunha

Vogal: Prof. João Manuel Gonçalves de Sousa Oliveira

Outubro de 2011

Aos meus pais e à minha irmã.

Agradecimentos

Em primeiro lugar quero agradecer ao professor Filipe Cunha por todo o apoio, esclarecimentos, ideias, alternativas e especialmente paciência que teve ao longo de toda a tese.

Ao Engenheiro Severino Raposo, pela conceção do ALIV original e pela génese do conceito base do quadrirotor com vários graus de liberdade. Ao Filipe Pedro pelo projeto preliminar que culminou na presente tese e ao professor Agostinho Fonseca por toda a ajuda, ideias e material, indispensáveis para o projeto.

Ao Alexandre Cruz pelas mãos extra, na fase fulcral da construção. Ao André João pelas dicas de SolidWorks®, ao João Domingos pelos grafismos profissionais, e à Helena Reis pelas dicas de inglês mais que correto.

Ao José Vale e aos elementos séniores da S3A por toda a ajuda no laboratório de Aeroespacial, quer em pormenores quer em técnicas de construção, conceitos teóricos importantes ou apenas que tornaram o trabalho no laboratório mais leve.

Aos meus amigos e colegas que me aturaram e aturam e que de uma maneira ou de outra contribuíram para a minha sanidade mental e por conseguinte para a conclusão deste projeto.

Por último à minha família, em especial aos meus pais e à minha irmã, por tudo, pois sem eles eu não seria.

Resumo

Os quadrirotores são uma das plataformas atualmente em maior desenvolvimento no mundo da investigação, devido à sua grande mobilidade, mas também ao seu potencial desenvolvimento como aeronaves não tripuladas capazes de pairar.

O objetivo deste projecto foi a construção de uma aeronave de pequena dimensão, da fusão dos conceitos de quadrirotor, com o de rotor inclinável, possibilitando a sua movimentação nos seis graus de liberdade, com a vantagem de manter a sua zona central nivelada, independente da sua movimentação e velocidade, que possibilita ainda uma redução do arrasto aerodinâmico através da otimização da superfície que enfrenta o escoamento. Esta possibilidade resulta da adição de inclinação em dois rotores opostos em duas direções que não a da sua rotação.

Inicialmente foram exploradas algumas alternativas para o conceito de rotores inclináveis e foram explanadas as restantes componentes da aeronave. Tratando-se de um conceito de aeronave ainda inexplorado as suas capacidades de movimentação foram totalmente determinadas. Um rotor ótimo foi desenhado para a aeronave e todos os componentes necessários para a sua construção e implementação foram avaliados, selecionados ou desenhados e construídos, sendo que a construção foi feita em compósitos laminados. Por fim, análises de funcionamento dos atuadores, de performance em voo e de arrasto aerodinâmico foram efetuadas.

Esta tese contribuiu então para a criação desta plataforma inovadora para futuros trabalhos, especialmente plataformas de controlo, no contexto de quadrirotores com rotores de inclinação variável.

Palavras-chave: Quadrirotor, Rotores de inclinação variável, Compósitos laminados, Rotor ótimo, ALIV3

Abstract

Quadrotors are currently one of the platforms under greater development in the academic world, because of their great mobility but also the potential to develop unmanned aircrafts capable of hovering.

This project's goal was to build a small-scale aircraft from the fusion of the quadrotor and tiltrotor concepts, enabling it to move in all six degrees of freedom with the advantage of maintaining its central core levelled, regardless of its movement and speed, which also allows a reduction in drag by optimizing the surface facing the airflow. This possibility results from adding a tilting movement in two opposed rotors in two directions, other than their rotation.

A few alternatives to the tilting rotors concept were explored, and the remaining components of the aircraft were fully explained. Since this is an original aircraft concept, all its motion possibilities were fully determined. An optimum rotor was designed for the aircraft and all the components needed for its construction and implementation were evaluated, selected or designed and constructed. The construction was done in laminated composites. Finally, analysis of servo's operation, flight performance and aerodynamic drag were conducted.

This thesis contributed to the creation of this innovative platform for future works, especially control platforms, in the context of quadrotors with rotor tilting ability.

Keywords: Quadrotor, Tilting rotors, Laminated composites, Optimum rotor, ALIV3

Contents

- Agradecimientos v
- Resumo vii
- Abstract ix
- List of Tables xvi
- List of Figures xix
- Abbreviations and Acronyms xxi
- Nomenclature xxiii

- 1 Introduction 1**
- 1.1 Concepts 1
 - 1.1.1 Quadrotor 1
 - 1.1.2 Tiltrotor 2
- 1.2 Historical Overview 2
- 1.3 State-of-the-art 4
 - 1.3.1 Previous Work 6
- 1.4 Motivation 9
- 1.5 Objective and Requisites 9
- 1.6 Thesis Structure 10

- 2 Preliminary Design 11**
- 2.1 Principal Structural Dimensions 11
- 2.2 Swivel Arm Concept 12
 - 2.2.1 The U-arm 13
 - 2.2.2 The Slim-arm 14
 - 2.2.3 The two-dimensional-servo-arm 15
 - 2.2.4 Arm's evaluation 16
- 2.3 Central Area 17
- 2.4 Landing Gear 19
- 2.5 Motion Control 19
 - 2.5.1 Levelled motions 20
 - 2.5.2 Rebalancing operations 23

2.5.3	Combined motions	26
3	Rotor Optimization	27
3.1	Theoretical principles	27
3.1.1	Panel Method	27
3.1.2	Blade Element Momentum Theory	30
3.1.3	Genetic Algorithm	36
3.2	Aerofoil selection	38
3.3	Optimum rotor	40
4	Off-the-shelf Components	43
4.1	Propulsion Components	43
4.2	Servos	46
4.3	Avionics	49
4.4	Communication	51
4.5	Battery	52
4.6	Structural Components	55
4.7	Extra Components	56
5	Design and Construction	57
5.1	Theoretical principles	57
5.1.1	Laminated composites	57
5.1.2	Finite Element Method (FEM)	59
5.1.3	Laminated composite manufacturing process	60
5.2	Structural project	61
5.2.1	Fixed arm	61
5.2.2	Swivel arm	62
5.2.3	Servo board	65
5.2.4	Electronic board	66
5.2.5	Central board and remaining central parts	67
5.2.6	Landing gear	70
5.3	Final design	72
6	Performance	75
6.1	Drag Analysis	75
6.1.1	SolidWorks® CFD analysis verification and validation	76
6.1.2	Flight drag analysis	76
6.2	Servo testing	77
6.3	Flight performance	78

7 Conclusions	81
7.1 Future Work	82
Bibliography	86
A Centre of mass	87
A.1 ALIV	87
A.2 ALIV3	87
B BEMT.m	88
C GA.m	91
D Tested aerofoils	96
E Servo calculations	97
F Analytical determination for laminated composites displacement	98
G Detailed weight of every component	99

List of Tables

1.1	ALIV3 project requisits	10
2.1	Arm's weighted decision matrix	17
3.1	Reynolds related properties for small rotors	33
3.2	Testing rotors' properties	35
3.3	C_T results comparison	35
3.4	C_P results comparison	36
3.5	Small scale rotor's results comparison	36
3.6	BEMT properties	40
3.7	Limits of the parameters to be estimated	41
3.8	Optimum rotor properties and results	41
4.1	Motor properties	44
4.2	Selected motors test results	45
4.3	ESC properties	46
4.4	Servo properties	49
4.5	Avionic component properties	51
4.6	Communication component properties	52
4.7	Battery properties	54
4.8	PDB properties	55
4.9	Material properties	55
4.10	Arm section determination	56
4.11	Camera properties	56
5.1	Composite elements properties	58
5.2	Laminae properties	58
5.3	Validation of maximum displacement between ANSYS® and the theoretic formulations	60
5.4	Thickness evaluation for the U-arm	63
5.5	Thickness evaluation for the servo support	64
5.6	Thickness evaluation for the servo board	66
5.7	Thickness evaluation for the electronic board	67

5.8	Thickness evaluation for the central boards	68
5.9	Thickness evaluation for the landing gear	72
6.1	Drag analysis	77
6.2	Servo testing	78
E.1	Inertia and angular derivatives for maximum servo torque estimation	97
G.1	U-arm model detailed weight	99
G.2	Slim-arm model detailed weight	100

List of Figures

1.1	Possible motions of a regular quadrotor	2
1.2	Wilco's tiltrotor concept	3
1.3	Bréguet's 1907 Gyroplane [1]	3
1.4	Maryland Univ. 2011 Gamera [2]	3
1.5	Oehmichen 2 [3]	3
1.6	de Bothezat [4]	4
1.7	Bell XV-3 [5]	4
1.8	Convertawings Model A [6]	4
1.9	Curtiss-Wright X-19 in 1963 [7]	4
1.10	Mesicopter [8]	5
1.11	Starmac 2 [9]	5
1.12	X-4 Flyer Mark II	5
1.13	IST's Mec. Department quadrotor [10, 11]	5
1.14	UAVision's U4-300 [12]	5
1.15	DraganFlyer X4 [13]	5
1.16	Parrot AR Drone with indoor hull [14]	6
1.17	Arducopter [15]	6
1.18	Mono Tiltrotor [16]	6
1.19	Bell Boeing Quad Tiltrotor Concept [17]	6
1.20	Severino Raposo's ALIV	7
1.21	ALIV's ABC Frame	7
1.22	ALIV's principal motions	8
1.23	Filipe Pedro's ALIV (ALIV2)	8
1.24	Designer concept of a pilotable size tilting quadrotor	8
2.1	Raposo's ALIV swivel arm	12
2.2	Pedro's ALIV2 swivel arm	12
2.3	Possible motor connections for the U-arm	13
2.4	Slim-arm configuration	14
2.5	2D-servo-arm configuration	15
2.6	Crank mechanism simplification	15

2.7	Arducopter electronics[15]	18
2.8	ALIV3's climb motion control	21
2.9	ALIV3's forward motion control	21
2.10	ALIV3's lateral motion control	22
2.11	ALIV3's yaw motion control	23
2.12	ALIV3's roll rebalancing	24
2.13	ALIV3's pitch rebalancing	25
3.1	XFLR5 Validation using L/D curve	29
3.2	Rotor disk annulus for a local momentum analysis of the hovering rotor(top and lateral view)	30
3.3	Blade Element Theory	31
3.4	NACA0012 C_L versus α for a range of Reynolds numbers	33
3.5	BEMT code verification	35
3.6	L/D versus α for $Re = 35000$ for the NACA aerofoils	38
3.7	L/D versus α for $Re = 35000$ for the selected aerofoils	38
3.8	C_L and C_D versus α curves for $Re = 35000$	39
3.9	Selected aerofoil MA409 profile, C_L and C_D versus α curves for several Re	39
3.10	PL comparison for real and theoretical rotors	42
3.11	Optimum rotor model	42
4.1	Gyroscope motion axis	47
4.2	Moments the servos have to overcome	49
4.3	Maximum current discharge rate limit	53
4.4	Battery capacity versus its weight for various C values (Real values and tendency lines)	54
5.1	ANSYS® convergence	60
5.2	Embracing plate	61
5.3	Tube sockets connectors	62
5.4	U-arm Construction	63
5.5	U-arm FEM analysis	64
5.6	Slim-arm construction	64
5.7	Servo support FEM analysis	65
5.8	Servo board models	66
5.9	Servo board FEM analysis	66
5.10	Electronic board FEM analysis	67
5.11	Central upper board FEM analysis	68
5.12	Bearing support models	69
5.13	Bearing board models	69
5.14	Pitch (θ) landing analysis	70
5.15	Roll (ϕ) landing analysis	71

5.16 Landing gear FEM analysis	72
5.17 ALIV3 final models	73
6.1 ALIV3 simplifications	76
6.2 SolidWorks® validation and verification	76
6.3 ALIV3's required total power	80
6.4 Power divisions for both alternatives	80
6.5 First-servo roll angle θ for forward flight	80

Abbreviations and Acronyms

ABC	Aircraft-Body-Centred (frame, assumed as body fixed frame)
ALIV	Autonomous Locomotion Individual Vehicle
BEMT	Blade Element Momentum Theory
BET	Blade Element Theory
CFD	Computational Fluid Dynamics
CNC	Computer Numerical Control
DC	Direct Current
ESC	Electronic Speed Control
FEM	Finite Element Method
FVM	Finite Volume Method
GA	Genetic Algorithm
GPS	Global Positioning System
HT	High Tenacity
IST	Instituto Superior Técnico
LQR	Linear Quadratic Regulator
MAV	Micro Air Vehicle
NASA	National Aeronautics and Space Administration
NED	North East Down (inertial frame)
PDB	Power Distribution Board
RC	Radio Control

STOL Short Take-Off and Landing

UAV Unmanned Aerial Vehicle

VTOL Vertical Take-Off and Landing

Nomenclature

Greek symbols

α	Effective angle of attack	Ω	Rotor angular speed
β_c	Crank motor plate angle	$\bar{\phi}$	Relative inflow angle
δ	Boundary-layer thickness	ϕ	Roll angle
δ^*	Displacement thickness	ψ	Yaw angle
δ^{**}	Density thickness	ρ	Density
λ	Total inflow ratio	$\bar{\sigma}$	Rotor solidity
λ_c	Climb inflow ratio	σ	Normal stress
λ_i	Induced inflow ratio	τ	Shear stress
λ_{taper}	Blade taper ratio	$\bar{\theta}$	Momentum thickness
μ	Dynamic viscosity	θ	Pitch angle
$\bar{\nu}$	Kinematic viscosity	θ^*	Kinetic energy thickness
ν	Poisson's ratio	θ_c	Crank angle

Roman symbols

A	Full rotor disk area	C_d	Outer layer dissipation coefficient
a	Acceleration	C_{d_0}	Blade drag coefficient
a_w	wake contraction parameter	C_f	Skin-friction coefficient
b	Random value for offspring creation	C_L	Lift coefficient
c	Chord	$C_{L\alpha}$	Slope of CL versus α curve
C_D	Drag coefficient	C_P	Power coefficient

C_{P_0}	Profile power loss coefficient	\tilde{n}	Transition disturbance amplification
C_{P_i}	Induced power loss coefficient	N	Number of nodes is aerofoil
C_T	Thrust coefficient	N_b	Number of blades
D	Drag	N_{gen}	Number of generations
E	Young's modulus	N_{keep}	Population selected for crossover
F	Force	N_{pop}	Size of the population
\bar{G}	Gravity amplification factor	N_w	Number of nodes in wake
G	Shear modulus	P	Power
g	Standard gravity on Earth	P_c	Power in climbing
\bar{H}	Angular momentum	P_h	Power for hovering
H	Shape parameter	P_i	Rotor's induced power
H^*	Kinetic energy shape parameter	P_0	Profile power
H^{**}	Density shape parameter	P_P	Parasitic power
H_k	Kinetic shape parameter	Q	Torque
h	Initial altitude	R	Rotor radius
I	Moment of inertia	R_c	Crank motor plate radius
i	Electric current	r	Dimensionless rotor radius
K, k	Performance empirical constants	r_c	Crank radius
K_v	Motor velocity constant	R_e	Reynolds number
l	Force's arm length	$R_{e_{\bar{\theta}}}$	Momentum thickness Reynolds number
l_c	Crank rod length	R_i	Newton solver residual
M	Moment	S	Cross section area
M_a	Mach number	SF	Safety factor
\dot{m}	Mass flow rate	T	Thrust
\tilde{m}	Local gradient of the mass defect	\tilde{T}	Rotation matrix
m	Mass	t	Time

U	Electrical potential difference	W	Weight
V	Velocity	w	Deflection
V_f	Fibre volume fraction	X,Y,Z	Cartesian components in the NED frame
V_m	Matrix volume fraction	x,y,z	Cartesian components in the ABC frame
V_c	Climb velocity	x_c	Crank piston position
v_i	Induced velocity in the rotor's plane	\bar{y}	Rotor position relative to its center
v_h	Induced velocity for hovering	z_s	Cross section position
v_w	Induced velocity at the wake's end		

Subscripts

Al	Aluminium	$root$	Rotor blade root
c	Compression	T	Transversal
e	Boundary-layer edge	t	Traction
INV	Inviscid	tip	Rotor blade tip
L	Longitudinal	U	U-arm model
max	Maximum	X,Y,Z	Cartesian components in the NED frame
$S.S.$	Stainless Steel	x,y,z	Cartesian components in the ABC frame
$slim$	slim-arm model	w	Wake
R	Rupture	$wall$	Wall boundary

Chapter 1

Introduction

The present Master's dissertation arises in sequence of Filipe Pedro's work [18] from 2009, in which the author envisioned an upgraded version of Severino Raposo's Autonomous Locomotion Individual Vehicle (ALIV) [19], an unconventional quadrotor, able to manoeuvre in all the six degrees of freedom such as the conventional quadrotor, adding the advantageous ability to maintain the central core of the aircraft in a levelled position, independent of the aircraft's movement and velocity, such improvement resulting from the addition of a tilting movement in two opposed rotors in two directions, other than their rotation.

1.1 Concepts

Firstly a few key concepts must be introduced, for a better understanding of the underlying idea behind this project, such as the Quadrotor itself and the tilting mechanism of a motor-rotor couple.

1.1.1 Quadrotor

The principles of the quadrotor, also known as a quadrotor helicopter or even quadcopter, date back to 1907 by the French Bréguet brothers, with what they called "Gyroplane" (figure 1.3), which according to Leishman [20], *"carried a pilot off the ground, albeit briefly. [...] Clearly, the machine never flew completely freely because [...] it lacked stability and a proper means of control"*.

A quadrotor is an aircraft heavier than air, capable of vertical take-off and landing (VTOL), which is propelled by four rotors, positioned in the same plane, parallel to the ground. Unlike standard helicopters, a quadrotor uses fixed-pitch blades in its rotors and its motion through the air is achieved by varying the relative speed of each propeller as is shown in figure 1.1. In a standard quadrotor, opposed rotors turn in the same direction, rotors one and three turn clockwise whereas rotors two and four spin in a counter-clockwise manner. This characteristic is mandatory so that the torque produced by each couple is cancelled by the other pair, making the control of a quadrotor symmetric, and this aspect leads to the necessity of absolute symmetry in a quadrotor, and the neutrality of its centre of mass, perfectly centred in a plane parallel to the rotors' plane.

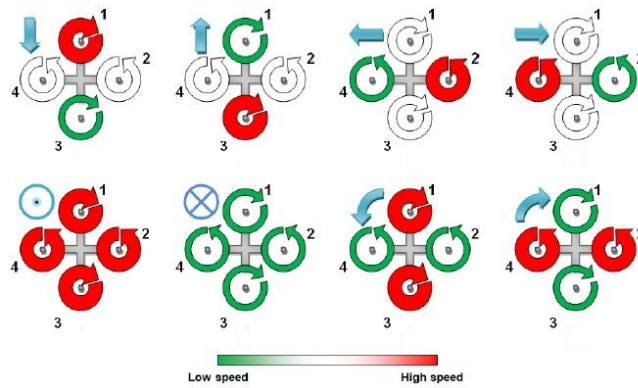


Figure 1.1: Possible motions of a regular quadrotor

The translational motion (except for altitude changes) of the quadrotor is achieved by a pitching or rolling angle, resultant from the change in speed of a single pair of opposite rotors, maintaining the other couple its pre-movement rotational speed. This leads to the conclusion that both directions in the plane of motion are fully independent and each direction is controlled by a pair of opposing rotors, uncoupling the longitudinal and lateral motions. The yaw movement and altitude alterations are made by an adjustment in all rotors angular speed.

1.1.2 Tiltrotor

The tiltrotor came from the need of combining helicopter properties, such as VTOL, hover and high manoeuvrability, with the abilities of airplanes, long range, lower consumption and heavier payloads, and so is generally classified as a tiltrotor an aircraft that has a pair (or more) of its rotors mounted on rotating surfaces (shafts, nacelles). This way the rotor can be responsible solely for the forward thrust, like in a regular plane, when it is parallel to the wing, but can also contribute solely to the lifting motion, like an helicopter, when it is perpendicular to the wing. The tiltrotor aircrafts are generally capable of VTOL or at least STOL (short take-off and landing) with an in-between rotor angle.

1.2 Historical Overview

In the first years of the twentieth century, the goal of every aeronautical inventor was to lift a person from the ground with a heavier than air apparatus, and remain the maximum time possible airborne. According to Leishman [1] and as presented in section 1.1.1 the first quadrotor ever envisioned was the Gyroplane (figure 1.3). This pioneer quadrotor had rotors of 8.1 metres in diameter, each one consisting of four light fabric covered biplane-type blades, giving a total of thirty two separate lifting surfaces. The Gyroplane made a brief and low flight (reportedly 1.5 metres above ground), which was most certainly achieved by the "ground effect". A 578kg aircraft with its rotor design and the rudimentary technology available would need at least 50hp delivered, which was the limit of Gyroplane's combustion engine [1]. Leishman also states that this result, due to the lack of controllability available, was assured "by the assistance of several men, one at each corner of the cross-like structure, stabilizing and perhaps even

lifting the machine". Curiously a team from the University of Maryland, to compete for the Sikorsky prize¹, built and flew what they called "Gamera"[2], a human powered quadrotor, with a design inspired by, and similar to the Gyroplane. The first flight was attempted on May 12th, 2011 and it was a success².



Figure 1.2: Wilco's tiltrotor concept



Figure 1.3: Bréguet's 1907 Gyroplane [1]



Figure 1.4: Maryland Univ. 2011 Gamera [2]

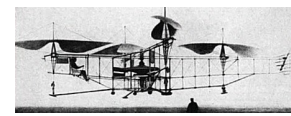


Figure 1.5: Oehmichen 2 [3]

In 1920 Etienne Oehmichen, a French engineer and helicopter designer, created what became the first quadrotor able to perform a controlled and stable flight, the Oehmichen 2 [3]. With more than a thousand test flights completed, had a 1Km range, an autonomy of more than seven minutes, and could hover at about three metres above the ground. The Oehmichen 2, figure 1.5, had a cruciform steel-tube frame, and a rotor at the end of each arm, these rotors and a fifth centred, above the pilot, all of them on the horizontal plane were responsible for the stabilization and lifting of the aircraft. The Oehmichen 2 also had three smaller propellers for translational purposes, a frontal propeller for steering, much like the tail rotor of a helicopter, and two more propellers for forward propulsion, similar to a plane.

All this complexity in design made the quadrotor perfectly stable horizontally but still capable of manoeuvring with a considerable higher freedom than any machine of its time. Despite the success, Oehmichen was not totally pleased with his creation, due to the very low altitude it could reach, mostly due to the engine's low capacities at the time, rendering the ground effect as a major contributor for the lifting of the quadrotor.

About the same time Dr. George de Bothezat and Ivan Jerome sponsored by the United States Army Air Service, developed the "*de Bothezat*" or "Flying Octopus" (figure 1.6) whose first flight occurred in 1922. The "*de Bothezat*" had four six-bladed rotors with 8.1 metres of diameter in a X-shaped, 20 metres structure and was capable of lifting up to five people at a maximum altitude of 5 metres. The X-shape differs from the regular quadrotor structure because the motors' arms are not 90° apart [4]. Despite the compliments by Thomas Edison who called the *de Bothezat* "*the first successful helicopter*", a favourable wind was necessary to achieve forwards flight and with the addition of its unresponsiveness, complexity of controls for the pilot and lack of power, the project was cancelled in 1924 [21].

It was not until 1930 that a significant fully controlled, without ground effect lifting bonus, hovering flight was achieved, by Corradino d'Ascanio's coaxial helicopter and quadrotors were forgotten until the late 1950's due to major advancements in uni-axial helicopters. Meanwhile George Lehberger in May 1930 registered the first patent of a tiltrotor, but the concept was only developed in 1942 by Focke-Achgelis although a final model of that exact patent was never built.

In 1955 Bell XV-3 [5] (figure 1.7) became the first tiltrotor to fully accomplish its goal, be able of VTOL and also cruise flight. It was powered by a 450hp radial engine and had a maximum speed of 296Km/h, with 411km of autonomy and a maximum ceiling of 4600 metres. This aircraft was indispensable as a

¹<http://vtol.org/awards/HPHCBooklet.pdf>

²<http://www.youtube.com/watch?v=q70tM5sDQhc>

prove of concept and many others followed it, including tilt-winged models.



Figure 1.6: de Bothezat [4]



Figure 1.7: Bell XV-3 [5]



Figure 1.8: Convertawings Model A [6]



Figure 1.9: Curtiss-Wright X-19 in 1963 [7]

One year later, in 1956, the first quadrotor capable of a truly controlled and without ground effect flight was achieved by D. H. Kaplan, designer and pilot of the Convertawings Model A Quadrotor, figure 1.8. This was the first quadrotor controlled solely by varying the hingeless rotors' speed and proving the quadrotors simplified movement concept, as shown in figure 1.1. This simplified version of a rotating wing aircraft was an innovation almost regressive for its time, because the complexity of standard helicopters was increasing. However served as the precursor of all quadrotors, because it eliminated complex cyclic-pitch-control systems typical of standard helicopters [6].

Since then more quadrotors for heavy payloads were developed but an entirely new concept was idealized by the Curtiss-Wright Corporation, a transporter plane (up to $500kg$) with two sets of wings and a rotor that could rotate 90° mounted at the tips of both wings, creating the innovative idea of a tilting quadrotor in their Curtiss-Wright X-19 [7] (figure 1.9). This aircraft did its first flight in 1963 and was capable of a range of $523Km$ and a maximum speed of $730Km/h$. Two aircrafts were built but the project was cancelled after a crash in 1965.

More models of quadrotors and tiltrotors where developed since then, without any inventive new solutions until the concept of an UAV (Unmanned Aerial Vehicles) was possible due to technological advancements, such as microelectronics, high definition sensors and even the global positioning system (GPS). Most UAVs are fixed-winged, typically small undetectable planes for aerial surveillance, but with the increasing necessity for hovering scenarios, the quadrotors got a new window for innovation and resurgence, and so since 2004 a large number of quadrotor (generally radio controlled) models were introduced, both in the military background as much as for civilian use, in universities and companies, as a platform for control engineering or even as a recreational model for the average consumer.

1.3 State-of-the-art

As stated before quadrotors had a shift in size and thus becoming again a source of interest for universities and companies. For universities quadrotors are a wonderful source for researchers to test new and improved control systems, that can afterwards be implemented in real life situations. Most projects come to life as a result of PhD programmes or partnerships between universities and companies; as an example the Mesicopter (2000) [8] (figure 1.10) is a Micro Air Vehicle (MAV) resultant from a partnership between Stanford University and NASA (National Aeronautics and Space Administration), with rotors of $10mm$ in diameter. Although very ambitious the project was cancelled because in all test flights it was never able to lift the weight of its own energy source, mainly due to the constrains of its scale.

In Stanford the mesicopter was later replaced by the Starmac 2 (2004)[9], in result of a partnership with Berkeley. It had the intention of demonstrating a multi agent control for quadrotors of about 1100g to 1500g with a 750mm structure, as shown in figure 1.11 and its primary result was accomplished. Another important contribution was from Pounds *et al.* (2004)[22] from Australian National University with their X-4 Flyer Mark II (figure 1.12), a 4kg quadrotor capable of 11 minutes of autonomy, with a blade flapping mechanism that introduced significant stability effects, furthermore this study concluded that positioning the rotors under the structure had benefits in the lifting properties of the quadrotor.

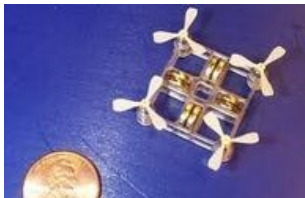


Figure 1.10: Mesicopter [8]



Figure 1.11: Starmac 2 [9]

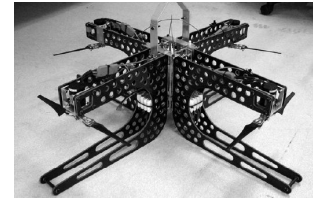


Figure 1.12: X-4 Mark II [22]

At Instituto Superior Técnico (IST) two major projects are being developed, both conventional, after an attempt on the original ALIV's control [23]. The first is from the Mechanical Department [10, 11], an off-the-shelf model with a 580mm structure and in its final stages of attitude control and with an autonomy of 10 minutes (figure 1.13). The other model belongs to the Electrical and Computer department, it has an 800mm structure built from scratch model and is capable of short low controlled flights. A final IST project, which is the final objective of this work will be presented in the next subsection. The structure dimension cited above refers to the distance between opposing rotors' centroids, and since the quadrotors are usually symmetric this dimension refers to both quadrotors arms.



Figure 1.13: IST's Mec. Department quadrotor [10, 11]



Figure 1.14: UAVision's U4-300 [12]



Figure 1.15: DraganFlyer X4 [13]

In the business world several models are being introduced, generally for recreational purposes, such as the Ardupcopter Models, the Parrot AR.Drone, the DraganFlyer models or the Portuguese UAVision's U4-300. The U4-300 [12] (figure 1.14) is a 2010 quadrotor model, developed by UAVision, has 1050mm structure, 1450g and an autonomy of 15 minutes, and is advertised for aerial surveillance or live coverage of sporting events and similar situations. DraganFlyer™ is a company specialized in Innovative UAV Aircraft and Aerial Video Systems, and one of its major consumers are the military. Their major asset, in what quadrotors are concerned, is the DraganFlyer X4 in figure 1.15, weighing a maximum of 980g (with payload) has a 1020mm structure and supposedly an autonomy of 30 minutes. Its major purpose is to acquire long range photographs [13].

Another commercial quadrotor project, rapidly expanding in popularity is the Parrot AR.Drone shown (in figure 1.16 with its indoor hull mounted), this being the first model with a simple addable plastic cover

(hull) to avoid damage in indoor flight, of the quadrotor itself as much as in the surroundings of the aircraft. The Parrot AR.Drone consist of an augmented reality flying quadrotor, that can be connected to any portable Apple™device (iPhone, iPad), seeing through the screen what the quadrotor's camera films in real time and thus enabling the creation of augmented reality games. The Parrot AR.Drone has a structure of $520mm$, can fly for 12 minutes, weights $420g$ with its indoor hull ($380g$ without) and has a maximum speed of $5m/s$ [14].

With all this market options, a lot of model aircraft enthusiasts started to envision their own quadrotors, resulting in the open source arduino based model, the Arducopter [15] (figure 1.17), consisting of a simple $600mm$ airframe weighting $1000g$ with payload and with a maximum autonomy of 10 minutes.



Figure 1.16: Parrot AR Drone with indoor hull [14]



Figure 1.17: Arducopter [15]



Figure 1.18: Mono Tiltrotor [16]



Figure 1.19: Bell Boeing Quad Tiltrotor Concept [17]

An alternative concept with similar principles to the ALIV was created by Baldwin Technologies [16], shown in figure 1.18, the Mono Tiltrotor. This is an innovative concept that merges tiltrotor with airplane, capable of VTOL but being much more efficient than regular tiltrotors and theoretically capable of matching fixed wing plane speeds. Still in the prof-of-concept stage, the prototype has achieved its designed purposes, and the company is preparing to create a full scale model. The main features of this aircraft are the coaxial main rotor, that rotates to a plane configuration for cruise flight, and the wing that can be deflected, for less drag in hover and return to its position for cruise. Finally, innovative new ideas were not only in the smaller scale. Bell in conjunction with Boeing had resurrected the Curtiss-Wright X-19 idea in a new conceptualized aircraft, in figure 1.19, the new Bell Boeing quad tiltrotor, able to perform VTOL and with as expected cruise speed of $463Km/h$ and a permitted maximum payload of up to $26tons$ [17].

1.3.1 Previous Work

As mentioned previously, the mentor of the small size multirotor with rotors of variable inclination, was Eng. Severino Raposo [19], with his ALIV (figure 1.20), a fully aluminium structure of $1811g$ and yet lacking stabilization software, which was semi-attempted with several approximations by Sérgio Costa in his 2008 master's thesis [23]. Costa developed and materialized a Linear Quadratic Regulator (LQR) for ALIV which was fully functional in flightgear's flight simulator, however the implementation in the real model was never attempted.

The definition of the frames and notations used in the ALIV are introduced at this point, for a better understanding of its movements and a possible cause for Costa's control malfunctioning. Figure 1.21 shows a representation of the ALIV with its rotors' identification. The front is defined by a marking in the fixed arm. For an accurate description of the ALIV's movements two right-hand orthogonal frames are needed, a reference inertial frame, called the North East Down (NED) frame, also known as local



Figure 1.20: Severino Raposo's ALIV

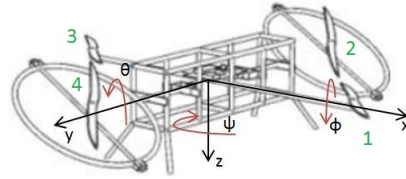


Figure 1.21: ALIV's ABC Frame

tangent plane (to Earth's surface) which as the name suggests points towards North, East and Down as X , Y and Z -axis respectively. The second frame is the body-fixed frame usually used in aeronautics known as Aircraft-Body-Centred (ABC) frame, both frames are centred in the ALIV's centre of mass. The ABC frame is identified by the subscripts (x, y, z) , corresponding to the front, right and down of the aircraft and the NED frame is identified by the subscripts (X, Y, Z) .

The major factor that made Costas's control not able to function in the real ALIV, was the principle behind Costa's work, in which he tried to control the ALIV as a regular quadrotor, and in future work enabling the tilting of the rotors. This problem will be detailed in the motion control section (sec. 2.5). Another important factor for the absence of a working control for the ALIV is due to its asymmetry. Of course for a complex structure like this it was impossible to make the four arms identical, mostly because only two of the four rotors are able to tilt in two directions, nevertheless the centre of mass should be in the geometrical centre of the structure, like regular quadrotors, where a virtual line drawn between opposing rotors intersects. By direct inspection of figure 1.20 it is noticeable that both servos mounted in the edge of the arms are on the same side, shifting the centre of mass in that same direction. With a technique similar to the one employed by Henriques [11] the centre of mass was found in the horizontal plane (xy plane in the ABC frame, fig. 1.21) as being decentred $37.06mm$ in the x coordinate and $9.88mm$ along y .

The total weight of the ALIV, without avionics, is $1811g$ and its dimensions are $563mm$ between motors in the fixed arm and $689mm$ between swivel arm's motors. The structure of the swivel arm is full on around the rotor, with $336mm$ in diameter allowing for an up to $330.2mm$ rotor diameter and leading to $1025mm$ of total span in the swivel arms axis (y).

The ALIV's forward motion is along the x -axis, the lateral motion is along the y -axis and the yaw movement is defined by a rotation along the z -axis. The rotation of the ABC frame relatively to the NED frame defines the attitude of the aircraft and the angles in the figure are defined according to Euler's notation [24]. The rolling motion (ϕ) corresponds to a quadrotor rotation about the x -axis, a rotation along the y -axis is called a pitching motion (θ), and a rotation along the z -axis is known as yaw (ψ). The introduction of two additional degrees of freedom in two of its rotors adds new possibilities for the ALIV's motion, theoretically making it faster and more stable than standard quadrotors [19]. Unlike regular quadrotors, by tilting its rotors, the ALIV can maintain its centre core levelled and have any kind of translational motion desired, or even yaw movement as shown in figure 1.22.

And this is the aspect of ALIV where Costa [23] and its concept creator Raposo [19] do not agree upon, both creating a major problem when the motors are tilted because none of them considered the

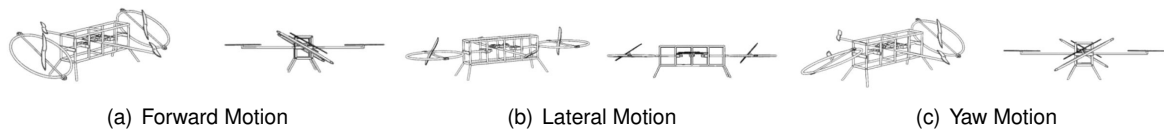


Figure 1.22: ALIV's principal motions

torque from the motors in other axis than z when the motors are tilted. According to Costa the ALIV's movement is possible in two different fashions, like a normal quadrotor, without any tilting of motors, making obsolete the concept, which was the point of his master's thesis, a control for the ALIV with a standard quadrotor configuration, and by tilting the motors like previously shown, that would be a subsequent work to his master's thesis. And so Costa makes the rotors turn like a standard quadrotor, as shown in figure 1.1, with opposing rotors turning in the same direction. However Raposo considered a different solution. Using figure 1.21 as a numeric reference for the motors, Raposo uses motors one and four to turn clockwise, according to the ABC's frame positive z -axis, and to cancel the z -axis torque, motors two and three rotate in a counter-clockwise manner.

In hover both alternatives would cancel the torque, however just by observing figures 1.22 (a) and (c) it is clear that neither of the alternatives are viable. When both motors pitch (θ) in the same direction (forward motion case), the torque of the rotor will not only be present, considering the ABC frame, in the z -axis but also in the x -axis, and so to nullify the effect only using the motors they need to be turning in opposite directions, like in Raposo's work; in Costa's scenario as adverse rolling moment is created. In the yaw motion scenario the motors pitch in opposite directions, and so Costa's alternative is the one that nullifies the torque, whereas Raposo's creates the adverse rolling moment. In the lateral motion Raposo's alternative also nullifies the torque, on the other hand, Costa's alternative produces an adverse pitching motion. This contradictory aspect will be approached in the next chapter.

Due to the dimension and symmetry problems of the original ALIV, an upgrade of the concept was envisioned by Filipe Pedro in his master's Thesis [18]. In his work he planned a new and lighter version of ALIV concept (figure 1.23), aiming its construction, mainly in carbon fibre. Pedro also made a Genetic Algorithm (GA) for the estimate of a optimum rotor for his ALIV2, did a study in the electronic and mechanical components necessary to build the device and finally employed a structural project of the ALIV2, nonetheless the problem of rotor tilting and torque anullement was never approached.



Figure 1.23: Filipe Pedro's ALIV (ALIV2)

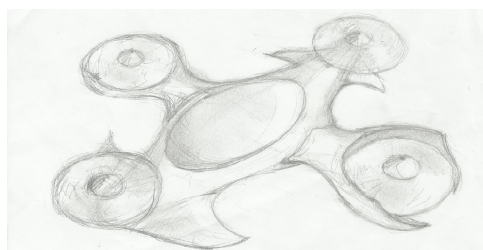


Figure 1.24: Designer concept of a pilotable size tilting quadrotor

1.4 Motivation

In a society where time is of the utmost relevance, mobility is the greatest asset anyone can desire. In overpopulated cities, even the shortest distances can become problematic. That is where airborne vehicles are at the vanguard, especially helicopters, which in situations of emergency are of most importance, either to save a life transporting a patient swiftly to a nearby hospital or even aiding in a fire-fight. Quadrotors can also play a very relevant role, because such as an helicopter, it has the ability to fly over any obstacle but it can also hover and land in a wide variety of locations, thus gaining a major advantage over fixed wing aircrafts. Moreover a quadrotor in relation to a helicopter adds some major advantages, considering the same hypothetical dimensionality:

- Absence of tail rotor, hence making it more energy efficient, instead of the usual helicopter's tail yaw control;
- Division of the propelling mechanisms, from one to four, this way making the quadrotor safer in case of a malfunction in one of the motors, and in case of accident. The division also simplifies the mechanical complexity, enabling the absence of gearing between motors and rotors;
- Finally, and in accordance with the above arguments, a payload increase can be achieved.

This innovative rotor tilting concept in comparison with a standard quadrotor, by the substitution of two normal rotors for two tilting ones, adds the advantage of maintaining a payload totally stable in its interior, perpendicular to gravity, and independent of its motion or velocity, and thus contributing to a drag reduction, because in all translations the surface facing the airflow does not change, while for standard quadrotors, its velocity is proportional to the roll or pitch angle of all the quadrotor.

Respecting all the topics cited above a design similar to figure 1.24 is achieved, in which a designer's concept of a quadrotor with two tilting rotors and capacity for an inboard pilot is illustrated. The small wings under the fixed rotors were designed so the rotors could retract into them for cruise flight. Such an apparatus could be a major asset aiding emergency crews, providing all the purposes of today's helicopters, plus, thanks to the tilting mechanism of two of its rotors, enabling total stability of its payload, reducing the flight drag and even allowing greater payloads through the existence of four motors.

All these advantages of the quadrotors regarding regular helicopters could not come without some drawbacks, such as some weight penalty, which can be minimized by more energy efficient sources than the ones presently available, and lighter and stronger materials. Although this pilotable size aircraft would be an interesting new face in the aviation market, that goal is quite far-fetched, and a prototype should be created as a proof-of-concept. Since the ALIV is external to the IST, the main goal of this thesis is to design and build a prototype of this innovative concept, as well as fully define its motion and design an optimum rotor for the constructed aircraft, the ALIV3.

1.5 Objective and Requisites

In every quadrotor project there are two major aspects to be accounted for, the platform project and the aircraft's control. In this thesis only the platform project will be materialized, laying the foundations for

the implementation of a control via a correct and applicable conceptualized motion, through rotor tilting, and never forgetting the rotor's torque.

As said previously, the goal of this thesis is to improve Pedro's concept when possible, and build a quadrotor with tilting movements in two directions in a pair of opposing rotors. A structural analysis should be conducted and the design of an optimum rotor should be achieved. Finally a full determination of the possible movements of the aircraft shall be completed. The quadrotor itself, the ALIV3, should be built with the following considerations, in accordance with Pedro's [18] and Raposo's [19] works:

Maximum weight (without payload)	1800g
Minimum endurance	10 minutes
Maximum translational and climb speed needed	$10m.s^{-1}$ and $5m.s^{-1}$
Payload	Camera (Video, Infra-red, Night vision)

Table 1.1: ALIV3 project requisits

1.6 Thesis Structure

In this chapter the key concepts used for this project, namely the quadrotor and tiltrotor are introduced. An historical overview and a state-of-the-art review of these concepts are conducted and the previous versions of the ALIV3's concept, to be fully designed and constructed, are described. Lastly this chapter enlightens the motivation, objectives and requisites for the ALIV3.

Chapter 2 is focused on the preliminary design of the ALIV3, its components maximum dimensions as well as their initially envisioned shapes are explained. A few swivel arm alternatives are introduced and a full motion determination is conducted with all possible movements of the ALIV3 are fully explained.

Chapter 3 is dedicated to the creation of an optimum rotor for the ALIV3. The choice of its aerofoil and all the remaining crucial geometric or operational variables are acquired, using the blade element momentum theory and a genetic algorithm solver, with the intention of building the virtual three-dimensional model in a rapid prototyping process.

All ALIV3 components that do not demand a precise design, or are very hard, or almost impossible to create, such as electronics, motors, and servos are selected in chapter 4, with a thorough and concise selection process for every component.

In chapter 5 all original designed components, and respective casts are depicted, and some dimensional decisions are sustained by a finite element method analysis.

The ALIV3 constructed models are evaluated and a performance analysis to the forward flight and climbing motion are executed in chapter 6. The servo's maximum torque and the drag of both alternatives is also studied to determine which arm alternative is the most suited to accomplish the design goals more efficiently. Also the drag analysis will study the gains of adding a cover to the ALIV3's central area.

The conclusions and a future work section close this thesis in chapter 7.

Chapter 2

Preliminary Design

The creation of the ALIV3 structure started with a revision of Filipe Pedro's [18] concept (figure 1.23), as well as of all the other relevant models previously depicted, with the aim of redesigning and building a working quadrotor. The structural concepts were divided in three major areas: the central area, where all the avionic components are located and where the arms and the landing gear converge; the swivel arm, the most important issue of this project, and what makes the ALIV3 unique; and finally the landing gear, to prevent any damage to the other ALIV3's components.

2.1 Principal Structural Dimensions

The first step was the definition of the prototype's dimensions. The original ALIV had $563mm$ between rotors in the fixed arm and $689mm$ between swivel arm's rotors, making it very unstable dynamically [19] while Pedro's ALIV2 had an $800mm$ by $800mm$ structure. There is no specific method for choosing these dimensions, nonetheless in standard quadrotors their greatest impact is in the pitching or rolling angular speeds, the longer the arm, the larger the moment and so the greater the angular speed. On the other hand with a larger arm, the greater the tensions in the structure, thus obliging for a more robust structure and therefore more structural weight. In ALIV3's case angular speed for rolling or pitching movements is not of great importance, because the translational motion is achieved by the motor-rotor couple tilt and not by aircraft tilting, and so the $800mm$ structure seems to be too large for what the ALIV3 requires or an optimal structure needs.

Referring to the most recent quadrotors [23, 10, 11, 15], all have a smaller, symmetrical structure. The Arducopter, the open source quadrotor has $600mm$, the Parrot AR.Drone has $520mm$ and IST's Mechanical Department quadrotor has $580mm$. In accordance with this dimensions, it was decided that the ALIV3 structure would have $600mm$, firstly to make it compatible with the Arducopter software, and secondly, in the absence of a theoretically strong principle behind this option, analysing the evolution of recent quadrotor models, all exhibit smaller dimensions, around the $520mm$ to $600mm$ range, whereas previous models had roughly $1000mm$. The ALIV3's total height will depend on the space needed for electronic components and landing gear design, while the final weight will depend on the arms and

landing gear design, and also the weight of all the indispensable components.

2.2 Swivel Arm Concept

The most important aspects of the ALIV3, mainly what makes the ALIV3 unique, are its swivel arms, capable of tilting the rotor in two directions.

In the original Raposo's concept (figure 2.1) the motor was placed inside a full circle aluminium frame, with the motor connected to a tube in turn connected to the frame in two positions, 180° apart. These connections allowed the rotation of the motor in the tube axis, referred in section 1.3.1 as the responsible for the lateral motion. This rotation is allowed by a servo, known as the second-servo, which is mounted in the circular aluminium.

Perpendicular to this tube, 90° from the its connections with the circular aluminium frame, a tube runs from the outer side of the circle, towards the central area of the ALIV, this tube is also connected to a servo (defined as the first-servo) and tilts the motor-rotor couple, and all the rest of the arm, allowing the previous described forward motion. Pedro realised that a full circle, while protecting the rotor in case of accident was an excess of weight that could be averted, and so in his design the full circle is replaced by a half circle (figure 2.2).

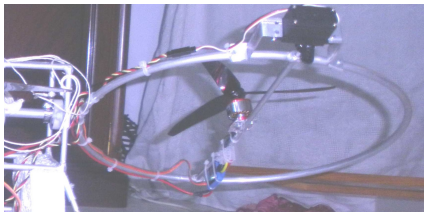


Figure 2.1: Raposo's ALIV swivel arm



Figure 2.2: Pedro's ALIV2 swivel arm

Some alternatives to Pedro's design were envisioned and will be depicted in the next subsections. Firstly it is necessary to determine the maximum rotor size and also the maximum tilt of the rotor (and motor) as dimension limitations for the arm. According to Aeroquad [25] (from the Arducopter family), for a general use, the standard rotor has 10 inches ($254mm$), while for heavy payloads a 12 inch ($304.8mm$) rotor is more appropriate, nonetheless in the ALIV2 the arm had just $220mm$ and in the ALIV $336mm$. So to accommodate the best option ($254mm$) and still have a margin for the servo, the maximum rotor size which will determine the size of an arm similar to the one from ALIV2 will be $11in$ ($279.4mm$).

The maximum tilting angle of the rotor has two consequences, firstly it will influence the servo needed for such a rotation and secondly it could prevent different designs where a 360° rotation cannot be achieved, but the goal of tilting rotors is accomplished. In Pedro's work is referred that the maximum tilting angle with the vertical in any direction is 62° , and so this will be the angle to take into consideration in the next subsection where alternatives to the ALIV2 swivel arm, also known as U-arm, will be depicted.

2.2.1 The U-arm

Figure 2.2 represents the U-arm, that as the the name states is a U shaped form, connected by its middle to a servo, the first-servo, which is attached to the main structure, and through that servo's rotation pitches (θ) the arm to achieve the forward flight motion. The lateral motion is acquired by another servo action, placed in the tip of the U, the second-servo, that is connected to the other U's end with a tube, while free to rotate. This rotation will roll (ϕ) the motor-rotor couple, that must stand on this connection. Two different alternatives for its placement were envisioned.

The first alternative is a simple connection with a carbon plate embracing the tube (glued or screwed to it) (figure 2.3(a)) which is the simplest way to connect efficiently the motor to the rest of the arm without many technical or construction abnormalities. This simplistic junction has exactly that in its favour, its simplicity, nonetheless the major torque producer, the rotor, is placed far from both servo's tilting axis, what would increase the torque that the servo needed to do, to tilt the motor and rotor.



Figure 2.3: Possible motor connections for the U-arm

To avoid this situation an alternative was envisioned, that could place the rotor's center of rotation closer to the tube. This solution places the motor inside a box, cut the tube where a hypothetical line from the first-servo would intersect it and place the box in its place, see figure 2.3(b). This alternative would decrease the moment effect from the rotor's rotation because the rotor itself would be closer to the rotating axis from both servos. On the other hand the structural complexity is increased as well as the construction problems. Instead of one tube with a motor in the middle, now two smaller tubes and a box need to be perfectly balanced and rotated by servo action.

Both alternatives will be exploited in the design and construction phase, in chapter 5. In the ALIV2 project this connection was made with the motor clamped to a very slim rod and such a connection would be very difficult to produce with the technology available in the Aerospace Laboratory.

The other aspect of importance in the U shaped design is the U itself. Its dimensions are mainly determined by the maximum rotor size previously set as $279.4mm$. Since the servo needs to be attached to the arm's end, that same section cannot be curved, as well as the the U's opposite tip for symmetry reasons. So as is shown in figure 2.2, both ends of the U are straight and the maximum distance between the arm tips should never surpass $279.4mm$, and the tip's straight section must be slightly larger than the selected servo's height. The middle of the U needs to be straight as well to allow a connection to the main structure, and its dimension equals the tip straight section so that the U curvature remains a quarter circle.

The distance between the middle of the U and the connection of the second-servo is supposed to be

half the size of the rotor, about $139.7mm$. The thickness of this structure (as well as all possible designs envisioned from henceforth) will be designed with a Finite Element Method (FEM) analysis in chapter 5. The width of the model is decided based on the servo's width. The maximum tilting angle of the motor and rotor in this design is not important because both servos' movement are not constrained by any structural component and so the rotor is free to tilt 360° from both servos' action.

2.2.2 The Slim-arm

The slim-arm has a very similar configuration to the U-arm, in the sense that it has a first-servo in the main structure pitching all the arm in the ABC frame's θ angle, and a second-servo in that arm that rolls the rotor (and motor) in the ABC frame's ϕ angle. This slim-arm configuration is illustrated in figure 2.4.

The slim-arm concept generated from the idea that 360° are not necessary in the tilt of the rotor and more than 180° are obsolete, because in case the rotor reaches an angle of 90° vertically there will be no lift provided by the rotor, just forward or lateral thrust, depending on the axis concerned. A tilt greater than 90° would have a negative lift and that is of no interest whatsoever.

So if 180° degrees is the reasonable maximum value for the tilting motions, the second-servo can be placed closer to the rotor, which in a way is better to decrease the first-servo's necessary torque, because the mass from the second-servo is closer to the first-servo's rotational axis, on the other hand hinders construction due to servo placement and motor stability.

The first-servo, like in the U-arm alternative, is placed in the main structure and tilts all the arm 360° . This arm is the slenderest it can be and has three 90° bends so the rotor's 180° tilt from the second-servo would not make it hit the arm. This configuration has the advantage to allow the placement of the rotor closer to the first-servo's rotational axis, but creates an inertial asymmetry. This design can also hide all the electric connections inside the arm and is lighter than the previous U-arm but its asymmetry can pose complications to both the servo selection and the ALIV3's operations.

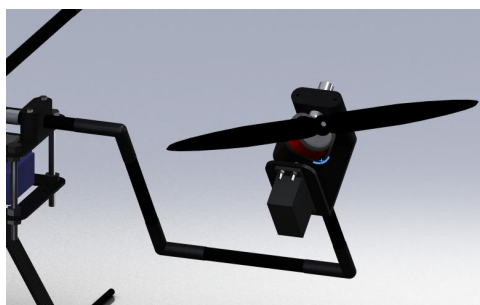


Figure 2.4: Slim-arm configuration

As the figure 2.4 illustrates the slim-arm consists of four small tubes connected through 90° elbows with a motor and servo support in the top. The dimension of the tubes corresponds to half the rotor's size and so $140mm$ should be considered for the second and third tubes, starting the numbering in the main structure. The first tube dimension is determined in relation to the first-servo's position and the $600mm$ total span decided earlier. The last tube's size is so that in conjunction with the servo support, the rotor is placed as close as it can be to the first-servo's rotational axis. The servo support size follows the same

rule as the straight portion of the U-arm. It needs to be as large as the servo selected needs it to be, and the motor is placed in a similar fashion to the U-arm, with a simple embracing plate or with the motor in box configuration. This second arm approach has the advantage of the motor positioning regarding the first-servo's rotational, however regarding the second-servo the situation is exactly the same as in the U-arm.

This slim-arm alternative can rotate the rotor 360° in the θ angle and 180° in the ϕ angle, is lighter than the U-arm but has an asymmetry that can jeopardise the servo selection, nonetheless is a valid and executable solution.

2.2.3 The two-dimensional-servo-arm

The final solution for the rotor tilting mechanism in two directions studied, was to create some kind of a two-dimensional servo, where the concept of first and second-servo would not matter. Based on the simple crank mechanism applied to two servos, the two-dimensional-servo-arm was conceived and is showed in figure 2.5.

It is important to note that the servos and the motor plate are only connected by the two cranks and connecting rods, and by the spherical bearing on top of the structural rod. The servos sit on a lower plate, the servo plate, which is embedded in the structural tube that comes from below. The spherical bearing stabilizes the motor place, but also enables the tilting of the rotor. This takes all the stresses out of the crank mechanisms from the servos, which are responsible for the separate orthogonal tilting movements. The size of both plates is determined by the size of the servo needed to produce the required torque. The crank mechanism is as large as the necessary tilt angle, and is ruled by the following trigonometric law, usually applied for piston motion.

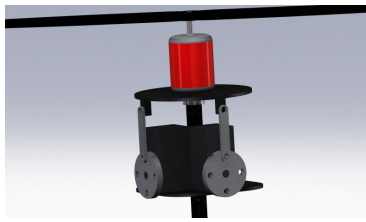


Figure 2.5: 2D-servo-arm configuration

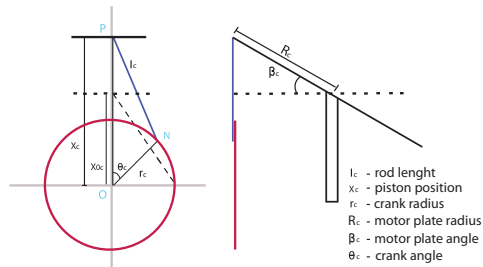


Figure 2.6: Crank mechanism simplification

Figure 2.6 represents a simplification of the crank mechanism applied to the rotor tilting, in one direction. The motion of the crank mechanism is determined by $l_c^2 = r_c^2 + x_c^2 - 2r_c x_c \cos(\theta_c)$, and rearranging $x_c = r_c \cos(\theta_c) + \sqrt{l_c^2 - r_c^2 \sin^2(\theta_c)}$. For the tilting angle:

$$\tan(\beta_c) = \frac{R_c}{x_c - x_{0_c}} \Big|_{x_{0_c} = x_c(\theta_c = 90^\circ) = \sqrt{l_c^2 - r_c^2}} \Rightarrow \beta_c = \arctan \left(\frac{R_c}{r_c \cos(\theta_c) + \sqrt{l_c^2 - r_c^2 \sin^2(\theta_c)} - \sqrt{l_c^2 - r_c^2}} \right) \quad (2.1)$$

Yet a major problem arises from this. For small β_c angles (tilting angle in one of the tilting orthogonal directions) this equation is valid, but for larger β_c angles the connecting rod would deform, because the

motor plate would maintain its dimension. This can be averted by letting the link of the connecting rod with the motor plate slide along the plate, maintaining the crank and connecting rod in the same plane, without deformation.

Another problem is the spherical bearing. While it increases the structural integrity of the concept, it also decreases its tilting ability. This is explained because its rotation is limited by its size in comparison with the tube that it is connected to, and the bigger the bearing the heavier the structure.

The connection to the main structure is done by an elbow junction at the end of the connecting tube, that has a dimension determined by the maximum tilting angle possible and the motor plate size. The advantage of this design is that the connection to the main structure is static, embedded in all degrees of freedom and so structurally simpler than the servo connections of the previous alternatives.

The two-dimensional-servo-arm configuration is an innovative concept, but very hard to build, its servos can rotate the motor through a crank mechanism that enables them to a tilting motion in both directions however inferior to 180° .

2.2.4 Arm's evaluation

A weighted decision matrix is employed, and shown in table 2.1, to choose which alternative is the best, or what alternatives, if more than one, should be built for a real prototype comparison. The factors for the evaluation will be:

- Arm weight, the lightest the better;
- Ease of construction, the most important factor, since the objective is to create a real model of the arm;
- Ease of control, if the design permits an easy control of the ALIV3;
- Servo size, proportional to the maximum torque needed to rotate the arm, if the maximum torque needed is very large the servo will increase in size and weight.

When a first and second-servo configuration is used, to standardise the selection process the first-servo maximum torque is the value considered for all servos' selection. All categories have a 0 to 10 evaluation and are weighted in accordance with the factor's importance or relevance to the final implementation of the ALIV3 in comparison with the original Raposo's ALIV. It is never enough to reinstate that all the values above, are purely qualitatively, and based on historical or empirical factors.

Concerning the arms' weight the original ALIV's arm is expectedly the heaviest of all alternatives, and the two-dimensional-servo-arm being the alternative with less material is the lightest. The remaining models are evaluated in comparison with these two statements.

The ease of construction, the most important factor, has its worst alternative in the two-dimensional-servo-arm, due to the tolerances and constraints imposed to enable a correct functionality of the arm. In terms of construction the slim-arm presents itself as the easiest alternative due to possible off-the-shelf incorporation in the arm structure.

Regarding the ease of control, for future implementation of a control software for the ALIV3, the slim-arm presents a few setbacks mainly due to the accentuated asymmetry of the concept; the two-dimensional-servo-arm presents a sinusoidal position distribution along servo functionality and the ALIV's

Arm alternative	Attributes (Relative Weighting)				Total
	Weight (25%)	Ease of Construction (45%)	Ease of Control (30%)	Servo Size (10%)	
ALIV's arm	5	5	5	5	5
U-arm	6	7	7	6	6.65
Slim-arm	8	8	3	3	6.5
2D-arm	10	1	3	10	4.85

Table 2.1: Arm's weighted decision matrix

arm, its simplification, the U-arm presents a clear improvement due to the underlying weight loss. Finally in terms of servo size, the two-dimensional-servo-arm is obviously the best option, since both servos are located near the motor. Its maximum torque requisites, will be much lower than all the other options. The slim-arm first-servo will have the worst result, due to the asymmetry of the arm itself.

As expected the two-dimensional-servo-arm is the most penalized design, mainly because the construction of such model would exceed the conditions of the laboratory where the work would be done, and thereby its fully realization in working conditions would be very hard to achieve, so its further design and construction shall not be pursued. The other two designs, the U-arm and the slim-arm, will be further studied in chapter 5 with the ultimate goal of construction.

2.3 Central Area

The central area is the core of the ALIV3, where all the mechanical and electronic components are located or are fixed to. The most important components of the central area, are the electronic ones, also known as avionics, necessary for the ALIV3's control. As an example, depicted in figure 2.7 are the Arducopter's [15] avionics, where both essential and non-essential components are shown. The essential components are:

- A battery, the energy storage system;
- Four Electronic Speed Control (ESC) to control each of the motor's angular velocity;
- A decision platform, usually a micro-controller where the control software would be, in this case an Ardupilot Mega;
- A set of sensors (magnetometer, accelerometers and gyroscopes), to aid the decision platform;
- Communication hardware, shown as a wireless connection to a computer (XBee) that could be replaced by a radio controller receiver;
- A Power Distribution Board (PDB) that is connected to the battery and redistributes its power to all the other electronic components.

A video camera can also be considered a part of the avionics, but since it is not a binding component, it will be considered as payload. As an addition a GPS receiver is presented, that can be used to turn a radio controlled quadrotor in a UAV quadrotor. Since the arm models selected for further study respect

the first and second-servo configuration, two servos plus all the avionics must be accommodated in this central area. All these electronic or mechanical components' selection will be addressed in chapter 4.

To accommodate all these components a strong yet light structure must be created. Its dimensions and number of levels will depend on the size and organization of the supra-cited components, and a spheroid aerodynamic cover shall also be taken into consideration, to decrease the drag from the ALIV3 in forward flight but also in lateral flight or even in climbing movements. In Pedro's ALIV2 [18] the central cover had a maximum radius of $113mm$ but since the limit proposed for the ALIV3's rotors distance was $600mm$ ($300mm$ of radius) and the maximum length of the selected arm design was $140mm$, considering a $50mm$ gap in both sides, the maximum radius for the central area cover will be $150mm$, and all components plus the structure, should fit inside that radius. The fixed arm will need to have at least $600mm$ and must also be connected to this central area.

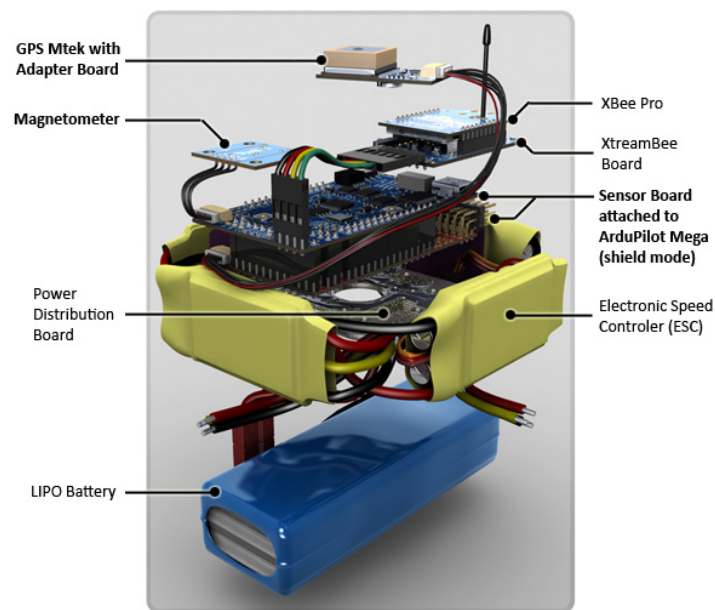


Figure 2.7: Arducopter electronics[15]

Regarding the position of the central components, usually the heavier equipment, the battery, is placed in the lowest position possible, firstly because in case of malfunction and a subsequent accident, the risk of damage to other components is seriously diminished, being the lowermost component. Secondly it lowers the centre of mass, Hoffmann *et al.* [26] suggests that the centre of mass should be in the rotor's plane, if not, adverse moments will be created. Nonetheless to prevent the unwanted tilt of the ALIV3 in a hard landing situation, a low centre of mass position is recommended.

Since the battery is the lowest of the essential components, and to prevent the entanglement of electric wiring the PDB and ESCs must be placed in its vicinity, so those components shall be placed as a second level of the central area, as figure 2.7 depicts. Finally the remaining components such as sensors, communications and first-servos shall be placed near the controller, and to assure a safe distance from the battery and the ESC's (high voltage components, comparing with the controller), and also to allow a barrier-free communication they shall be placed in the uppermost level of the central area. The fixed arm must also intersect this region so that its rotor's plane is at the same height as the swivel

arm's. Below the battery, the central board shall be connected to the landing gear, and the placement of the payload shall also be in this region.

2.4 Landing Gear

The landing gear is one of the most important aspects of the ALIV3, because it protects the ALIV3 from damaging any component when landing, by being the lowermost point of the ALIV3 in a regular balanced landing, and it should also be robust enough to withstand large accelerations on rough landings. Furthermore must not allow any component other than the landing gear to hit the ground and must prevent the ALIV3's rotation due to an high centre of mass in unexpected tilted landings.

Its design will be inspired by the shape of a skier's legs, with two skis pointing forward and a inverted V structure connecting the skis to the main ALIV3 frame. Its dimensions must be decided after all the other components are fully developed, because it needs to be large enough, taking into account the previous cited tilted or tilting situations, but cannot have a large opening angle, or it will intersect the swivel arm, and also because it should not be too large or it will compromise the total weight. As a first rule for the landing gear's dimensions it was decided that in tilted landings with the rotors at zero degrees, on hovering condition, the maximum landing angle for design reasons is 30° .

2.5 Motion Control

In a standard quadrotor, the control is achieved by varying symmetrically the thrust of opposite rotors, and every translation is obtained by roll or pitch angles. In the ALIV3 configuration that is impossible and a more complex operation needs to be conducted and will be explained next.

As previously reported, in the first version of the ALIV two separate control alternatives were attempted, neither of them fully functional in the real model, and thus this section serves as control guidelines for future implementation. It is important to emphasize that the main problem with both Raposo's [19] and Costa's [23] motion alternatives, was that neither of them really considered the rotor's torque effects due to the tilting of the motor-rotor couple, and thus unexpected adverse roll and pitch moments were created when that same tilt was conducted.

The control alternative chosen as a guideline is Severino's, because in longitudinal or lateral motion, the opposite rotors' symmetric rotation cancels the motor-rotor torque in all axis, and the main objective of any aircraft is to move. Of course the easy equilibrium that can be achieved from standard quadrotors decoupled motions is lost, and an alternative for rebalancing the ALIV3 in the case of a gust or some unexpected rolling or pitching movement will be explained next, as well as the lateral or longitudinal motions, the yaw movement and the climb and descent motions.

In Severino's alternative, rotors one and four had a negative rotation while rotors two and three rotated positively, in the ABC frame, where the z -axis points down and the motions directions described are in accordance with that fact. Rotors (and motors) two and four are the ones able to tilt. It is important to introduce a few notations in the ALIV for a better understanding of the motions themselves. Referring

to figure 1.21 and respecting the numbering of the rotors, θ_2 and θ_4 will be the pitch of the rotors through action of the first-servo. They are responsible for the forward motion, with the pitch of the swivel arm, positive according to the right hand rule. The roll of the rotors, resultant from the action of the second-servo, responsible for the lateral motion, will be depicted as ϕ_2 and ϕ_4 . All these angles equal zero when the rotor points upwards, in the hovering position, in the opposite direction of the ABC frame's z -axis, nonetheless the angle's signals always respect the ABC frame. Each rotor's torque is represented by Q_i with the corresponding subscript for every rotor or motor, the rotor's thrust is represented by T_i , both torque and thrust from the rotor are proportional to the motor's power output. This leads to a total of eight independent output variables, $T_1, T_2, T_3, T_4, \phi_2, \theta_2, \theta_4$ and ϕ_4 .

2.5.1 Levelled motions

In all levelled motions (all translations and rotation along z) the ALIV remains parallel to the ground. The simplest levelled motion in any quadrotor is hovering, where all rotors must provide the same thrust and accordingly the same torque. Since all the motors are similar the same power is delivered from all of them equally. For a hovering scenario the total thrust must match the weight of the ALIV3 and that is accomplished by the following equations:

$$\sum F_z = 0 \Rightarrow 0 = -(T_1 + T_2 + T_3 + T_4) + mg |_{T_1=T_2=T_3=T_4} \quad (2.2a)$$

$$\sum M_z = 0 \Rightarrow 0 = Q_1 + Q_2 + Q_3 + Q_4 |_{Q_1=-Q_2=-Q_3=Q_4} \quad (2.2b)$$

From now on \bar{T} is defined as the thrust necessary for a rotor to lift a quarter of the ALIV3's weight ($\bar{T} = \frac{mg}{4}$) and \bar{Q} as the torque necessary to produce the supra-cited thrust. Also the moments in x and y -axis produced by \bar{T} equal to $\bar{T} \frac{b}{2}$ are omitted but always present.

In the following examples a simplified ALIV is shown with the direction of rotation of the rotors, and viewed from above. The axis shown respects the ABC frame's axis directions and the rotors' turning directions also respect the descriptions above, appearing the opposite because z is pointing downwards. The alteration or maintenance of the rotors' thrust in relation to \bar{T} is displayed by mathematical signs (+, - or =), and the tilting of the rotors is represented by an arrow alongside the rotor illustrating the directional extra thrust provided by the rotor's tilting.

Climb motion

After hovering, climbing is the simplest of the ALIV3's possible operations. As figure 2.8 suggests, by increasing evenly all motors' power the balance of the aircraft is maintained and the increased thrust when greater than the drag force results in upwards acceleration. The climb speed will depend of the thrust increase (ΔT) and all these aspects are described in the following expressions:

$$\sum F_z = ma_z \Rightarrow -ma_z = -4(\bar{T} + \Delta T) + mg + D_z |_{T_1=\bar{T}+\Delta T=T_2=T_3=T_4} \quad (2.3a)$$

$$\sum M_z = 0 \Rightarrow 0 = Q_1 + Q_2 + Q_3 + Q_4 |_{Q_1=-Q_2=-Q_3=Q_4} \quad (2.3b)$$

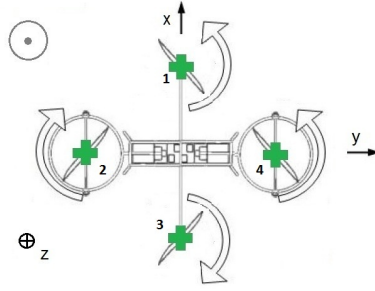


Figure 2.8: ALIV3's climb motion control

To descent it is only necessary to decrease the total thrust evenly: the higher the decrease the faster the descent. To maintain a steady climb or descent, with constant velocity, a_z must be null with $4\Delta T = D_z$ to maintain the z -axis velocity.

Forward motion

In forward levelled motion, the tilting of the rotors is responsible for the motion itself, through an increase in thrust and a pitching angle (θ_i) of both rotors, two and four. The increase in thrust must be such that the lift (z -axis) component must remain as it was before tilting, for two reasons: to maintain the ALIV3 levelled its total weight must remain equal to the lift, and secondly to maintain the torque in the z -axis null. The x -axis torque is symmetric in both tilted rotors and thus null, and the moment created through the forward thrust is symmetric for both rotors and thus cancelled. The distance between rotors (or motors), from now on is represented as l , and was defined previously as $600mm$. The following equations rule the forward motion case:

$$\sum F_x = ma_x \Rightarrow ma_x = T_2 \sin \theta_2 + T_4 \sin \theta_4 - D_x \Big|_{T_2 \sin \theta_2 = T_4 \sin \theta_4 = \Delta T, \theta_2 = \theta_4} \quad (2.4a)$$

$$\sum F_z = 0 \Rightarrow 0 = -(T_1 + T_2 \cos \theta_2 + T_3 + T_4 \cos \theta_4) + mg \Big|_{T_1 = \bar{T} = T_2 \cos \theta_2 = T_3 = T_4 \cos \theta_4} \quad (2.4b)$$

$$\sum M_x = 0 \Rightarrow 0 = Q_2 \sin \theta_2 + Q_4 \sin \theta_4 \Big|_{Q_2 = -Q_4} \quad (2.4c)$$

$$\sum M_z = 0 \Rightarrow 0 = Q_1 + Q_2 \cos \theta_2 + Q_3 + Q_4 \cos \theta_4 + \frac{b}{2}(T_2 \sin \theta_2 - T_4 \sin \theta_4) \Big|_{Q_1 = \bar{Q} = -Q_3} \quad (2.4d)$$

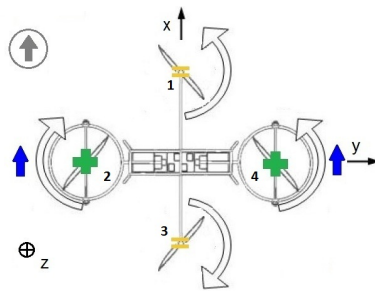


Figure 2.9: ALIV3's forward motion control

For a forward motion, figure 2.9 θ_i angles must be negative, according to the ABC frame; for a backwards motion it is only necessary to perform a positive shift in both rotors' θ_i . For a constant velocity with forward motion already achieved, a_x must be zero, with $2T \sin \theta = D_x$ to maintain a constant x -axis velocity.

Lateral motion

The lateral motion (figure 2.10) is almost identical to the forward one, but instead of a pitch angle in the rotors, a rolling (ϕ_i) movement is necessary in the tilting rotors. The y -axis torque is symmetric in both tilted rotors and thus null. As in forward motion the increase in thrust must be such that the lift (z -axis) component must remain as it was before tilting, and the ruling equations for lateral motion are also similar to the previously shown forward motion case:

$$\sum F_y = ma_y \Rightarrow ma_y = T_2 \sin \phi_2 + T_4 \sin \phi_4 - D_y |_{T_2 \sin \phi_2 = T_4 \sin \phi_4 = \Delta T, \phi_2 = \phi_4} \quad (2.5a)$$

$$\sum F_z = 0 \Rightarrow 0 = -(T_1 + T_2 \cos \phi_2 + T_3 + T_4 \cos \phi_4) + mg |_{T_1 = \bar{T} = T_2 \cos \phi_2 = T_3 = T_4 \cos \phi_4} \quad (2.5b)$$

$$\sum M_y = 0 \Rightarrow 0 = Q_2 \sin \phi_2 + Q_4 \sin \phi_4 |_{Q_2 = -Q_4} \quad (2.5c)$$

$$\sum M_z = 0 \Rightarrow 0 = Q_1 + Q_2 \cos \phi_2 + Q_3 + Q_4 \cos \phi_4 |_{Q_1 = \bar{Q} = -Q_2 \cos \phi_2 = -Q_3} \quad (2.5d)$$

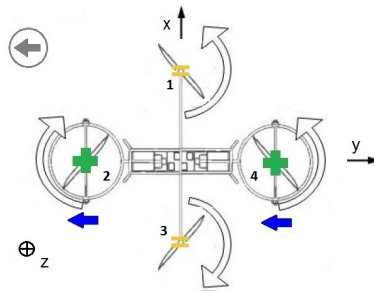


Figure 2.10: ALIV3's lateral motion control

To move left, as the figure 2.10 shows, the rotors' roll angles (ϕ_i) must be negative, on the other hand to achieve a lateral motion to the right the roll of the moments must be positive. As for the previous examples, for a constant velocity a_y must be zero and $2T \sin \phi = D_y$.

Yaw motion

The yaw motion is a little more complex than the previous motions described. In standard quadrotors the yaw motion is achieved by varying evenly and symmetrically each couple of rotors, but with these rotors' rotation configuration such a solution is impossible. So the yaw motion for the ALIV3 is simply achieved through the increase of thrust in one rotor, and a pitch of that same rotor to increase the yaw speed by both alterations. This creates a slight backwards adverse motion, but the main goal is achieved nonetheless. Both yaw movements (positive and negative rotations) are shown in figure 2.11 and the

following equations describe the movement for a positive yaw. From now on rotational drag is considered negligible and ΔT_i is the increase in thrust of rotor i .

$$\sum F_x = ma_x \Rightarrow ma_x = T_4 \sin \theta_4 - D_x \quad (2.6a)$$

$$\sum F_z = 0 \Rightarrow 0 = -(T_1 + T_2 + T_3 + T_4 \cos \theta_4) + mg \Big|_{T_1=T_2=T_3=\bar{T}-\frac{\Delta T_4 \cos \theta_4}{3}} \quad (2.6b)$$

$$\sum M_x = 0 \Rightarrow 0 = Q_4 \sin \theta_4 - \left[T_4 \cos \theta_4 - \left(\bar{T} - \frac{\Delta T_4 \cos \theta_4}{3} \right) \right] \frac{b}{2} \quad (2.6c)$$

$$\sum M_z = I_z \ddot{\psi} \Rightarrow I_z \ddot{\psi} = Q_1 + Q_2 + Q_3 + Q_4 \cos \theta_4 + T_4 \sin \theta_4 \frac{b}{2} \Big|_{Q_1=-Q_2=-Q_3 < Q_4 \cos \theta_4} \quad (2.6d)$$

For small rotor pitching angles the acceleration in the x -axis is null, and thus the ALIV3 remains in a stationary yaw motion. To obtain an equilibrium along the z -axis the tilted rotors increase in thrust is balanced by a decrease in the other three rotors thrust and thus maintaining the ALIV3 levelled. In this case the y moments created by the lift of rotors one and three, usually \bar{T} , in this case $\bar{T} - \frac{\Delta T_4 \cos \theta_4}{3}$ is omitted because they cancel each other and that's the reason why in the $\sum M_x$ the expression is as shown.

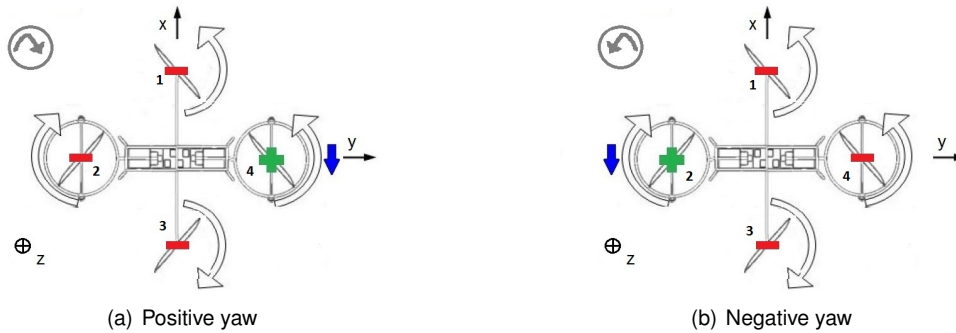


Figure 2.11: ALIV3's yaw motion control

To rotate in the opposite direction, every alteration regarding an hovering status is mirrored (figure 2.11), and instead of altering rotor four thrust and roll angle, these alterations are made in rotor 2 and all the rotors thrust are decreased.

2.5.2 Rebalancing operations

All the previous situations are necessary to complete every possible mission scenario, nonetheless they would only work if no oscillations occurred, and all components behaved as expected, but that does not happen, and so it is necessary to rebalance the ALIV3 to a levelled position when it rolls or pitches in an unexpected and uncontrolled manner. In all the cases presented henceforth the NED frame will be used to fully correspond to translational motions; for rotations the ABC frame is used, and all rebalancing operations are transient and take only fractions of a second.

Roll rebalancing

For a positive roll tilt angle ϕ of the ALIV3 (meaning a negative roll rebalancing), the following equations serve as guidelines. For the rebalancing, a negative roll of the rotors is necessary (ϕ_i) to cancel the lateral motion; in the following expressions ϕ_i should always be positive and so $-\phi_i$ is used, the same applies for θ_4 . An increase in rotor four thrust is mandatory to create the roll rebalancing; to cancel the z torque created, that same rotor is pitched (negatively in the ABC frame). Finally rotors one and three need to increase their thrust to balance the ALIV3's weight, and their increase must be equal, to cancel each other's torque.

$$\sum F_X = ma_X \Rightarrow ma_X = T_4 \sin \theta_4 \cos \phi_4 - D_X \quad (2.7a)$$

$$\sum F_Y = 0 \Rightarrow 0 = (T_1 + T_3) \sin \phi - T_2 \sin(\phi_2 - \phi) - T_4 \cos \theta_4 \sin(\phi_4 - \phi) \quad (2.7b)$$

$$\sum F_Z = 0 \Rightarrow 0 = -((T_1 + T_3) \cos \phi + T_2 \cos(\phi_2 - \phi) + T_4 \cos \theta_4 \cos(\phi_4 - \phi)) + mg \quad (2.7c)$$

$$\sum M_x = I_x \ddot{\phi} \Rightarrow I_x \ddot{\phi} = Q_4 \cos \phi_4 \sin \theta_4 + [T_4 \cos \theta_4 \cos \phi_4 - (\bar{T} + \Delta T_2)] \frac{b}{2} \quad (2.7d)$$

$$\sum M_y = 0 \Rightarrow 0 = Q_2 \sin \phi_2 + Q_4 \cos \theta_4 \sin \phi_4 \quad (2.7e)$$

$$\sum M_z = 0 \Rightarrow 0 = Q_1 + Q_2 \cos \phi_2 + Q_3 + Q_4 \cos \theta_4 \cos \phi_4 - T_4 \cos \phi_4 \sin \theta_4 \frac{b}{2} \quad (2.7f)$$

As for the adverse translations, for small rotor pitch angles the acceleration in the x -axis is null which results in 5 equations and 7 variables $T_1, T_2, T_3, T_4, \phi_2, \phi_4$ and θ_4 , so to simplify the system it is defined that $T_2 = \bar{T}$ and as said before with $T_1 = T_3$, the system has a total of 5 independent variables and is solvable. The second rotor's thrust is maintained and all the others are increased, the remaining variables are changed according to the speed in which the manoeuvre must be preformed, as well as the undesired initial roll angle. Figure 2.12(a) represents the scenario described above.

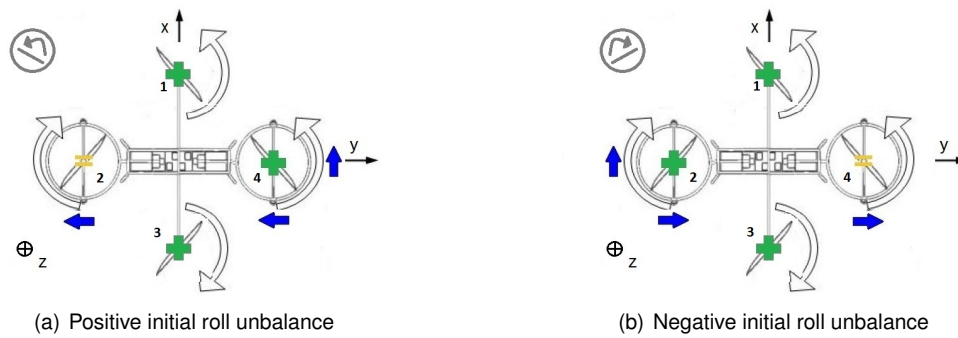


Figure 2.12: ALIV3's roll rebalancing

To obtain the rebalancing from a negative initial roll angle it is just a matter of reversing the concept as figure 2.12(b) illustrates. Rolling the rotors in the opposite direction and this time pitching rotor two instead of rotor four in the same direction as before. Mathematically the negative initial roll is identical to the case described above and the real value of ϕ_i is used. θ_2 is used instead of θ_4 and so it is just a question of switching all the 2 subscripts by 4 and vice-versa.

Pitch rebalancing

The pitch rebalancing is maybe the most complex manoeuvre of the ALIV3, because all 8 output variables are used, yet the rebalancing is quite simple.

Referring to figure 2.13(a), for a positive initial pitch angle, both tilting rotors are forced to move, they pitch (in the negative angle in the ABC frame) to cancel the backwards motion the unexpected roll creates and roll symmetrically to create a pitching moment and rebalance the quadrotor. The fixed arm's rotors speed (one and three) should be decreased but that would depend on the power available and that is not mandatory, their speed can be maintained, however the thrust in both rotors must remain equal. Rotors two and four should also have the same thrust between them as well as roll angle (θ_i), the pitch angle must be symmetric, $-\phi_2 = \phi_4$ because ϕ_4 is positive in the ABC frame in this situation. The following equations represent a positive initial pitch angle unbalance and are constructed in a way that θ_i should always be positive, and so $-\theta_i$ shall be used.

$$\sum F_X = 0 \Rightarrow 0 = (T_1 + T_3) \sin \theta - T_2 \cos \phi_2 \sin(\theta_2 - \theta) - T_4 \cos \phi_4 \sin(\theta_4 - \theta) |_{T_1=T_3, T_2=T_4} \quad (2.8a)$$

$$\sum F_Y = 0 \Rightarrow 0 = T_2 \cos \theta_2 \sin \phi_2 - T_4 \cos \theta_4 \sin \phi_4 |_{\theta_2=\theta_4, -\phi_2=\phi_4} \quad (2.8b)$$

$$\sum F_Z = 0 \Rightarrow 0 = -((T_1 + T_3) \cos \theta + T_2 \cos \phi_2 \cos(\theta_2 - \theta) + T_4 \cos \phi_4 \cos(\theta_4 - \theta)) + mg \quad (2.8c)$$

$$\sum M_y = I_y \ddot{\theta} \Rightarrow I_y \ddot{\theta} = Q_2 \cos \theta_2 \sin \phi_2 + Q_4 \cos \theta_4 \sin \phi_4 \quad (2.8d)$$

$$\sum M_z = 0 \Rightarrow 0 = Q_1 + Q_2 \cos \theta_2 \cos \phi_2 + Q_3 + Q_4 \cos \theta_4 \cos \phi_4 + T_2 \cos \phi_2 \sin \theta_2 \frac{b}{2} - T_4 \cos \phi_4 \sin \theta_4 \frac{b}{2} \quad (2.8e)$$

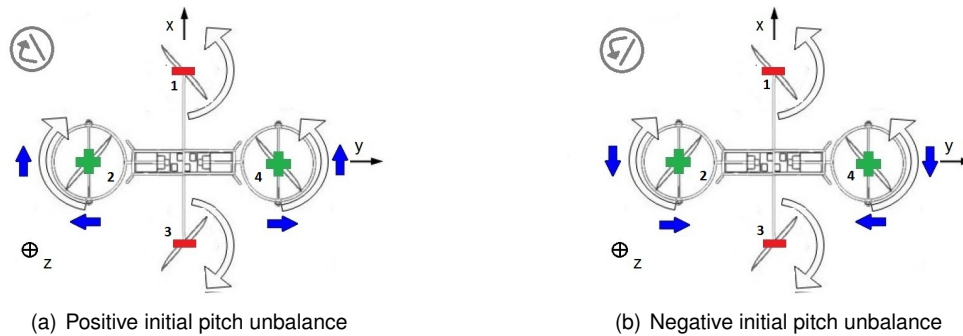


Figure 2.13: ALIV3's pitch rebalancing

In this case $\sum M_x$ is omitted because all opposed thrusts and torques cancel each other, resulting in four independent variables that will be determined in relation to the initial pitch angle and the speed in which a levelled position needs to be reached. If the initial pitch angle is negative (figure 2.13(b)) it is only necessary to invert the tilting of the rotors, do an inwards roll and a backwards pitch, which mathematically is identical to equations 2.8, with a positive θ_i used.

By making the rotors' roll angles null, it is interesting to note that the ALIV3 can remain in hover with a pitch angle in a stable position, and thus with a mounted camera a wide variety of imagery is possible with the ALIV3, because a rebalancing of the pitch angle or a transition to a desired pitch angle is the

same operation, and then to remain in hover in that position, is just a case of making all equations in 2.8 equal zero by imposing $\phi_2 = \phi_4 = 0$ and thus the global pitch angle ϕ is maintained and the ALIV3 maintains its position.

2.5.3 Combined motions

Up until now all possible motions were only shown isolated, however in a real flight situation more than one of the described manoeuvres may need to be executed at the same time, and that can be done simply by combining the wanted motions simultaneously. In the previous rebalancing subsection the autonomous ALIV3's motions were described, those are the manoeuvres that the control should be responsible for, without any interference from the pilot, and should activate immediately when necessary, to rebalance the ALIV3.

In subsection 2.5.1 (levelled motions) the motions described were supposed to be controlled by the user, yet all of those motions are subjected to oscillations and so the control software needs to be aware of what the motion, or motions, the pilot desires and disable all other, applying the necessary compensations in case of unwanted and unexpected oscillations both for translations as for rotations.

Chapter 3

Rotor Optimization

One of the key components of every quadrotor are its rotors, responsible for the transmission of the motor's power to the air and subsequently responsible for the force production in the aircraft, to counteract its weight or to move it through the air. In our case the rotors are fixed to the motors and do not need additional degrees of freedom in that connection, they just need to produce a lifting force in the motor's direction. A wide variety of rotor options are available in the market, but usually only for right-hand rotation, to serve as an airplane's propeller. The nomenclature difference is based on historic reasons, where a propeller is solely responsible for the production of horizontal thrust, where a rotor is usually responsible for the lifting of helicopters but latter adapted to moving propeller with the inception of tiltrotors.

In every quadrotor right-hand (pusher) and left-hand (puller) propellers are necessary due to the torque cancellation requisite, but the market does not provide a wide variety of puller options, and so the creation of an optimum rotor for the ALIV3 is an interesting and challenging alternative. In Pedro's work [18] a Genetic Algorithm (GA) implemented in Octave based on the Blade Element Momentum Theory (BEMT) was created to preform this task, and in this chapter an improved version, this time in MatLab®, of this solution will be presented since Pedro's alternative had a few problems that needed revision, and an improved code was necessary to create a new *de facto* optimum rotor for the ALIV3.

A few aspects are of major importance for the optimum rotor creation, such as the selection of the perfect aerofoil for the situation at hand, choosing a rotor theory to estimate the rotor's behaviour and finally assemble the genetic algorithm to determine the maximum of the function coming from the selected rotor theory. The theoretical principles behind these aspects need to be presented first.

3.1 Theoretical principles

3.1.1 Panel Method

To analyse what aerofoil should be selected for an ideal rotor the Computational Fluid Dynamics (CFD) XFLR5¹ program will be used. The XFLR5 is the evolution of the two-dimensional panel method

¹<http://xflr5.sourceforge.net/xflr5.htm>

implementation by Drela, 1989 [27] in his XFOIL which was an interactive program that utilized a two-dimensional panel method code with integral boundary layer theory to analyse aerofoils in viscous or inviscid flow fields.

The origins of the panel method date back to 1967 when a three-dimensional panel method was introduced to estimate the drag of a ship hull [28]. After that all the major aerospace companies developed their own kind of programmes, meanwhile the two-dimensional realm also evolved and a number of panel method codes have been developed for aerofoil analysis and design. The panel method codes with more acknowledgement are Professor Richard Eppler's (of the University of Stuttgart) PROFIL code, developed partly funded by NASA, in the early 1980s, and MIT Professor Mark Drela's XFOIL code, the one that served as base for XFLR5 used in this thesis.

The viscous formulation [29] which is the one used in XFLR5, is ruled by the following standard compressible integral momentum and kinetic energy shape parameter equations, where the streamwise coordinate is ξ .

$$\frac{d\bar{\theta}}{d\xi} + (2 + H - M_{a_e}^2) \frac{\bar{\theta}}{V_e} \frac{dV_e}{d\xi} = \frac{C_f}{2} \quad (3.1)$$

$$\bar{\theta} \frac{dH^*}{d\xi} + (2H^{**} + H^*(1 - H)) \frac{\bar{\theta}}{V_e} \frac{dV_e}{d\xi} = 2C_d - H^* \frac{C_f}{2} \quad (3.2)$$

Being V the velocity, M_a the Mach number, C_f the skin-friction coefficient equal to $2\tau_{wall}/\rho_e V_e^2$, with τ_{wall} as the shear stress of the wall and ρ as the density. The subscript e refers to the boundary-layer edge. The momentum thickness $\bar{\theta}$ is given by $\int \left(\frac{\rho V}{\rho_e V_e} \right) \left[1 - \left(\frac{V}{V_e} \right) \right] d\eta$ where η is the perpendicular direction to ξ on the aerofoil plane. The shape parameter is $H = \frac{\delta^*}{\bar{\theta}}$ with δ as the boundary layer thickness and δ^* as the displacement thickness $\delta^* = \int \left[1 - \left(\frac{\rho V}{\rho_e V_e} \right) \right] d\eta$. Finally H_k is the kinematic shape parameter equal to $\int [1 - (V/V_e)] d\eta / \int (V/V_e) [1 - (V/V_e)] d\eta$. H^* is defined as the kinetic energy shape parameter ($H^* = \theta^*/\bar{\theta}$) and H^{**} the density shape parameter, defined by $\delta^{**}/\bar{\theta}$, where δ^{**} is the density thickness $\int (V/V_e) [1 - (\rho/\rho_e)] d\eta$ and θ^* the kinetic energy thickness $\int (\rho V / \rho_e V_e) [1 - (V/V_e)^2] d\eta$.

A rate equation for the maximum shear stress coefficient (C_τ) is used to account for deviations of the outer layer dissipation coefficient ($C_d = (1/\rho_e V_e^3) \int \tau (\partial V / \partial \eta) d\eta$) from the local equilibrium value, known as the shear stress lag equation, however in this case it is only important to consider laminar cases ($Re < 5 \times 10^5$) [30], since the Reynolds number ($Re = Vc/\bar{\nu}$) for the rotor size in study (in table 3.2 $Re \simeq 35000$) is very low, the value of the rotor cord (c) is very small, (whereas $\bar{\nu}$ is the kinematic viscosity of the air) and so the stress lag equation is substituted by:

$$\frac{d\tilde{n}}{d\xi} = \frac{d\tilde{n}}{dRe_\theta} (H_k) \frac{dRe_\theta}{d\xi} (H_k, \theta) \quad (3.3)$$

that models the growth of amplitude in \tilde{n} (transition disturbance amplification variable) of the most amplified Tollmien-Schlichting wave, with $Re_{\bar{\theta}}$ as the momentum thickness Reynolds number equal to $\rho_e V_e \bar{\theta} / \mu_e$ and μ as the dynamic viscosity.

Using $\bar{\theta}$, δ^* and \tilde{n} as governing variables and using equations 3.1, 3.2, 3.3 and adding V_e , as an external unknown that does not constitute an additional system unknown it is just a matter of discretizing those equations using two-point central differences, e.g. the trapezoidal rule, to create a non-linear

system with three coupled equations. Introducing the local gradient of the mass defect ($\tilde{m} = V_e \delta^*$) and considering that the flow inside the aerofoil is stagnated, is necessary to relate V_e to the free-stream and a sum of all the vorticity and sources on the aerofoil. Simplifying all these concepts Drela arrived at:

$$V_{e_i} = V_{IN} V_i + \sum_{j=1}^{N+N_w-1} d_{ij} \tilde{m}_j, \quad 1 \leq i \leq N + N_w \quad (3.4)$$

which provides the potential flow solution about the aerofoil for any distribution of mass defect on the aerofoil and wake. Note that d_{ij} embodies the effect of the local gradient of the mass defect near the trailing edge on the global boundary-layer edge velocity distribution by the effect of the Kutta condition. N represents all nodes in the aerofoil, and N_w the nodes in the wake. The discrete boundary layer equations are now closed and the system is solved by a full Newton method with variables $\partial\theta_j$, $\partial\tilde{m}_j$ and $\partial\tilde{n}_j$, the Newton system results in a jacobian matrix (J_{ij}) the cited variables and a residual (R_i):

$$\left[\begin{array}{c} J_{ij} \end{array} \right] \left\{ \begin{array}{c} \partial\bar{\theta}_j \\ \partial\tilde{m}_j \\ \partial\tilde{n}_j \end{array} \right\} = \left\{ \begin{array}{c} -R_i \end{array} \right\}, \quad 1 \leq i \leq N + N_w \quad (3.5)$$

By solving this Newton system to a negligible residual, the XFLR5 software provides a reliable solution for both the lift coefficient (C_L) and the drag coefficient (C_D) of a specific aerofoil which will be needed for the optimum rotor design, and should be validated next.

XFLR5 validation

To validate the results provided by the XFLR5 software, it is necessary to compare real wind test tunnel data with the results provided by the software. Using Laitone's research [31] as a reference point, in which the author performs a series of tests to the NACA0012 aerofoil in a wind tunnel, with the goal to determine the aerofoil's reaction to Reynold numbers below 70000.

In Laitone's work the most relevant aspect regarding the validation required for the XFLR5 is shown in its figure 1, where the L/D versus angle of attack (α) curve for a NACA0012 aerofoil is presented for a Reynolds number of 20700, and overlapping this result with the XFLR5 results for the same aerofoil at the same 20700 Reynolds number, figure 3.1 is obtained. The choice of the L/D curve is made in accordance with the need of both C_L and C_D 's variation with the angle of attack (α).

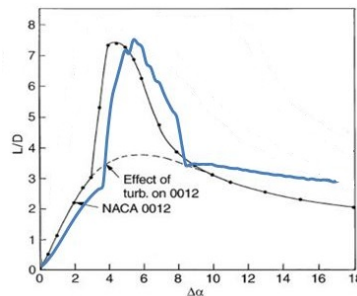


Figure 3.1: XFLR5 Validation using L/D curve

The Latoine original results are in black and XFLR5 solution in blue, and apart from the slight offset in terms of the aerofoil's angle of attack, the two solutions are almost identical and with a very diminished error, with a maximum of 25% for angles of attack greater than 15° , disregarding the slight angle of attack offset, that has a maximum of 1° , but with no major consequences in the latter analysis where the lift and drag shall be analysed separately.

3.1.2 Blade Element Momentum Theory

The BEMT was first introduced by Gustafson and Gessow in 1946 and it is a hybrid theory for hovering rotors that combines the basic principles from the Momentum Theory and from the Blade Element Theory (BET), in an attempt to estimate the inflow distribution along the blade [20]. In the momentum theory the rotor is modelled as an actuator disc and the theory is developed around the conservation of mass, momentum and energy. In contrast the BET divides a blade in a finite number of sections and analyses that section as a bi-dimensional profile. In the BEMT the conservation laws are applied to an annulus with a $d\bar{y}$ width, shown in figure 3.2, being \bar{y} the annuli position in relation to the rotor's centre.

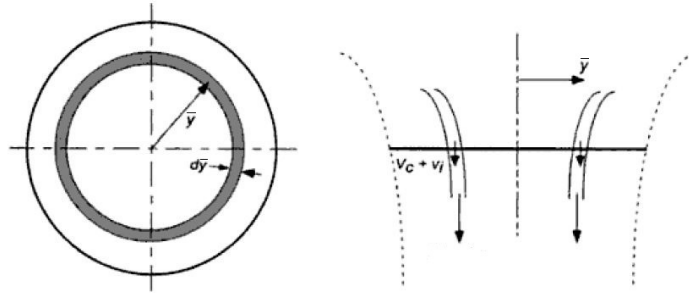


Figure 3.2: Rotor disk annulus for a local momentum analysis of the hovering rotor (top and lateral view)

Assuming that the successive rotor annuli have no mutual effects on each other, the incremental thrust dT , may be computed based on a simple momentum theory, the mass flow rate (\dot{m}), with the area given by $dA = 2\pi\bar{y}d\bar{y}$ is:

$$d\dot{m} = \rho dA(V_c + v_i) = \rho 2\pi\bar{y}d\bar{y}(V_c + v_i) \quad (3.6)$$

V_c being the climb velocity and v_i the induced velocity in the rotor's plane.

Two key notions from the momentum theory are necessary at this point, the velocity at the end of the wake (v_w) and the wake contraction parameter (a_w). Using the conservation of mass principles between the rotor's disc and the wake's end the following is obtained:

$$\dot{m} = \rho A(V_c + v_i) = \rho A_w(V_c + v_w) = \rho A(V_c + v_i) = \rho(a_w A)(V_c + v_w) \quad (3.7a)$$

$$\Rightarrow v_w = \frac{v_i + V_c(1 - a_w)}{a_w} \quad (3.7b)$$

It is now convenient to define the non-dimensional quantities by dividing the lengths by the rotor's radius R , and the velocities by the tip speed ($V_{tip} = \Omega R$), resulting in the total inflow ratio λ , the induced

and climb inflow ratios (λ_i and λ_c) and the rotor's adimensional radius (r):

$$r = \frac{\bar{y}}{R} \quad (3.8a)$$

$$\lambda = \frac{V_c + v_i}{\Omega R} \quad (3.8b)$$

$$\lambda_i = \frac{v_i}{\Omega R} \quad (3.8c)$$

$$\lambda_c = \frac{V_c}{\Omega R} \quad (3.8d)$$

By the conservation of momentum and equation 3.7:

$$dT = d\dot{m}v_w = \rho 2\pi \bar{y} d\bar{y} (V_c + v_i) \frac{v_i + V_c(1 - a_w)}{a_w} \quad (3.9a)$$

$$= \frac{2}{a_w} \rho \pi (V_c + v_i) (V_c + v_i - a_w V_c) \bar{y} d\bar{y} \quad (3.9b)$$

Introducing the thrust coefficient ($C_T = T/(\rho V_{tip}^2 A) = T/(\rho(\pi R^2)(\Omega R)^2)$):

$$dC_T = \frac{\frac{2}{a_w} \rho \pi (V_c + v_i) (V_c + v_i - a_w V_c) \bar{y} d\bar{y}}{\rho(\pi R^2)(\Omega R)^2} = \frac{2}{a_w} \left(\frac{V_c + v_i}{\Omega R} \right) \left(\frac{V_c + v_i - a_w V_c}{\Omega R} \right) \left(\frac{\bar{y}}{r} \right) d \left(\frac{\bar{y}}{R} \right) \quad (3.10a)$$

$$= \frac{2}{a_w} \lambda (\lambda - a_w \lambda_c) r dr \quad (3.10b)$$

So far the flow was assumed as bi-dimensional, however the real flow is three dimensional, especially near the tip of the blade, where the blade tip vortices have a negative effect in the lift force, and so a correction to thrust force needs to be introduced. The best suited alternative is Prandtl's tip-loss function given by:

$$F = \frac{2}{\pi} \arccos e^{-\frac{N_b}{2} \left(\frac{1-r}{r\bar{\phi}} \right)} \quad (3.11)$$

with N_b as the number of blades in the rotor, $\bar{\phi}$ the relative inflow angle and combining with the thrust coefficient:

$$dC_T = F \frac{2}{a_w} \lambda (\lambda - a_w \lambda_c) r dr \quad (3.12)$$

It is now important to introduce a few concepts from the BET. As said previously the BET divides a blade in a finite number of sections and analyses that section as a bi-dimensional profile (figure 3.3).

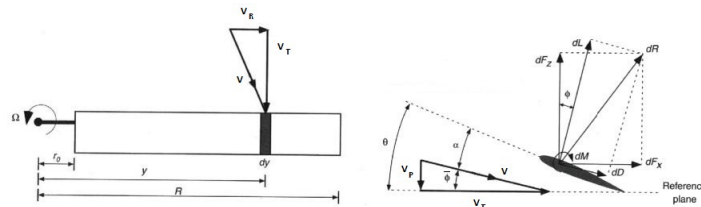


Figure 3.3: Blade Element Theory

A few definitions are important, such as the relative inflow angle ($\bar{\phi} = \arctan \frac{V_P}{V_T} = \frac{\lambda}{r}$), the pitch angle of the blade (θ), the effective angle of attack ($\alpha = \theta - \bar{\phi}$) resulting in $C_L = C_{L_\alpha} \alpha = C_{L_\alpha} (\theta - \bar{\phi}) = C_{L_\alpha} (\theta - \frac{\lambda}{r})$ and finally the rotor solidity ($\bar{\sigma} = \frac{N_b c}{\pi R}$). Since the Lift and Drag forces are orthogonal and

defined in a blade fixed angle, it results that the forces in the reference frame of figure 3.3 are:

$$dF_x = dL \sin \bar{\phi} + dD \cos \bar{\phi} \quad (3.13a)$$

$$dF_z = dL \cos \bar{\phi} + dD \sin \bar{\phi} \quad (3.13b)$$

And by definition:

$$dL = \frac{1}{2} \rho V^2 c C_L dy \quad (3.14a)$$

$$dD = \frac{1}{2} \rho V^2 c C_D dy \quad (3.14b)$$

$$dT = \rho A (\Omega R)^2 dC_T = N_b dF_z \quad (3.14c)$$

$$dP = \rho A (\Omega R)^3 dC_P = N_b dF_x \Omega \bar{y} \quad (3.14d)$$

For the thrust and power coefficients (C_T, C_P) and assuming $\bar{\phi}$ as a small angle with the approximations $\cos \bar{\phi} = 1$ and $\sin \bar{\phi} = \bar{\phi}$ and that the drag is at least one order of magnitude smaller than the lift, resulting in $dD \sin \bar{\phi} = dD \bar{\phi} \simeq 0$. Finally V can be defined as $\Omega \bar{y}$:

$$dC_T = \frac{N_b dF_z}{\rho A (\Omega R)^2} = \frac{N_b dL \cos \bar{\phi} + dD \sin \bar{\phi}}{\rho (\pi R^2) (\Omega R)^2} = \frac{N_b dL}{\rho (\pi R^2) (\Omega R)^2} \quad (3.15a)$$

$$dC_P = \frac{N_b dF_x \Omega \bar{y}}{\rho A (\Omega R)^3} = \frac{N_b (dL \sin \bar{\phi} + dD \cos \bar{\phi}) \Omega \bar{y}}{\rho (\pi R^2) (\Omega R)^3} = \frac{N_b (dL \bar{\phi} + dD) \Omega \bar{y}}{\rho (\pi R^2) (\Omega R)^3} \quad (3.15b)$$

Simplifying:

$$dC_T = \frac{1}{2} \left(\frac{N_b c}{\pi R} \right) \frac{(\Omega \bar{y})^2}{(\Omega R)^2} C_L d \frac{\bar{y}}{R} = \frac{1}{2} \bar{\sigma} C_L r^2 dr \quad (3.16a)$$

$$dC_P = \frac{1}{2} \left(\frac{N_b c}{\pi R} \right) \frac{(\Omega \bar{y})^3}{(\Omega R)^3} (\bar{\phi} C_L + C_D) d \frac{\bar{y}}{R} = \frac{1}{2} \bar{\sigma} r^3 (\bar{\phi} C_L + C_D) dr \quad (3.16b)$$

And finally introducing the notions of induced power loss factor and (C_{P_i}) profile power loss factor (C_{P_0}), which are due to the viscous drag forces on the rotor blade and the aerofoil shape, respectively:

$$dC_T = \frac{1}{2} \bar{\sigma} C_{L_\alpha} (\theta r^2 - \lambda r) dr \quad (3.17a)$$

$$dC_P = \frac{1}{2} \bar{\sigma} r^2 \lambda C_L dr + \frac{1}{2} \bar{\sigma} r^3 C_D dr = dC_{P_i} + dC_{P_0} \quad (3.17b)$$

it is noticeable that $dC_{P_i} = dC_T \lambda$.

Now combining the C_T equations 3.12 and 3.17:

$$F \frac{2}{a_w} \lambda (\lambda - a_w \lambda_c) r dr = \frac{1}{2} \bar{\sigma} C_{L_\alpha} (\theta r^2 - \lambda r) dr \quad (3.18)$$

$$\lambda = \frac{\sqrt{16 a_w^2 \lambda_c^2 F^2 + 16 a_w C_{L_\alpha} r \bar{\sigma} \theta F - 8 a_w^2 C_{L_\alpha} \lambda_c \bar{\sigma} F + a_w^2 C_{L_\alpha}^2 \bar{\sigma}^2}}{8 F} - \frac{a_w C_{L_\alpha} \bar{\sigma}}{8 F} + \frac{a_w \lambda_c}{2} \quad (3.19)$$

It is fundamental to introduce the Power Loading (PL) parameter, that represents the non-dimensional

ratio of thrust produced to the power required and is the variable to maximize in the GA implementation to achieve the optimum rotor:

$$PL = \frac{T}{P} = \frac{W}{P} = \frac{C_T}{C_P(\Omega R)} \quad (3.20)$$

BEMT implementation

Based on the previous equations, and with C_T calculated from eq.3.17, the BEMT code is constructed. However it is noticeable that C_T and C_P depend on λ , C_L and C_D , that depends of F and α , that are dependent of $\bar{\phi}$ that depend on λ and so an iterative process is required to achieve a solution.

In Pedro's work [18] a BEMT code was created, however some key aspects were approximated, and no iterative process was implemented. The major shortcomings were the non-implementation of the tip-loss factor, assuming the flow along the rotor disc as perfectly two dimensional, the other major drawback was the approximation of $C_L = 2\pi\alpha$ which is valid for high Reynolds numbers (*i.e.* 1×10^5) and angles of attack below 10° for symmetric aerofoils. It is important to determine, for small scale rotors, what is the magnitude of the Reynolds numbers in place, so considering the following properties achieved by Pedro in his optimum rotor estimation:

Average Properties	
ρ	1.225 kg.m^{-3}
μ	$1.8 \times 10^{-5} \text{ kg.m}^{-1}.\text{s}^{-1}$
$V = \Omega \bar{y}$	60 m.s^{-1}
c	8.5 mm
$Re = \frac{\rho V c}{\mu}$	34708.3

Table 3.1: Reynolds related properties for small rotors

And so for the real situation presented, the average Reynolds number magnitude is one order of magnitude smaller than the validity of the C_L approximation. To confirm this aspect in figure 3.4 is shown how the lift coefficient versus α behaves, varying the Reynolds number for the NACA0012 aerofoil:

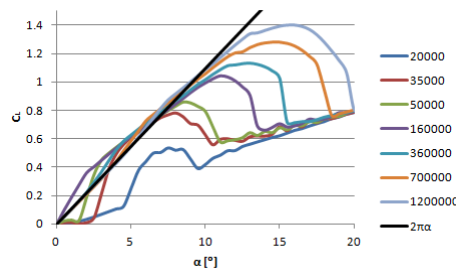


Figure 3.4: NACA0012 C_L versus α for a range of Reynolds numbers

Analysing figure 3.4 it is confirmed that the C_L values should be taken into consideration to a thorough and correct implementation of the BEMT theory. For a Reynolds number of 35000 the linear $C_L = 2\pi\alpha$ approximation is valid for an angle below 8° . This could mean that for angles below 8°

the approximation was acceptable, however this is the average Reynolds number of the rotor, and both above and below Reynolds numbers do exist, and for a $Re = 20000$ the approximation has an enormous error. So the values of both C_L and C_D will be obtain in XFLR5 and then organized for the BEMT theory computation.

Although these two simplifications were made to permit a non iterative computation of the BEMT theory, in this upgraded version of the software those simplification will not be used and an iterative calculation will be implemented. All these contribute to the rebuilding and improvement of the previous BEMT code, as well as its transfer to the MatLab[®] software, for a faster computation.

The new improved BEMT.m code is provided in appendix B, but since a few important alterations were made, a new verification and validation is mandatory; however is also necessary to clarify how it works. Starting from the top the rotor properties need to be inserted in order to calculate the chord (c) and torsion, that will, in fact, be the local blade pitch angle (θ) along the radius of the blade, as well as the local Reynolds number (Re) and rotor solidity ($\bar{\sigma}$) in all divisions created. Then the inflow rate (λ) is computed by equation 3.19, as it was done in the original version of the code, with the $F = 1$ and $C_{L_\alpha} = 2\pi$ approximations, and then the alterations arrive with the iterative process beginning.

The iteration starts by calculating the relative inflow angle ($\bar{\phi} = \lambda/r$) and the effective angle of attack ($\alpha = \theta - \bar{\phi}$) followed by the computation of C_{L_α} , which comes from the C_L versus α table for several Reynolds numbers provided by the XFLR5 software, divided by α . When the values of α or Re are not present on the table, the required C_L value is interpolated using the surrounding table values, and the same is valid for the later needed C_D value. After this the Prandtl's tip-loss function F is acquired, by equation 3.11 and finally the new inflow rate λ is computed, with equation 3.19. When the iterative process has converged the C_T (eq. 3.12) and C_P values are calculated, through a sum of every division's contribution. For simplicity C_P is divided in $C_{P_i} = C_T\lambda$ and C_{P_0} determined by equation 3.17. Finally the power loading, thrust and power are calculated through equations 3.20 and the first member of equations 3.14 c) and d). The optimum wake contraction parameter (a_{w0}) value was determined by Leishman [20] to be 0.61, and Pedro [18] also confirmed this result, and so it is the value used here.

Verification and validation of the new BEMT code

For a precise and thorough implementation of the BEMT theory it is important to verify what will be the number of divisions in the blade shall be, and the number of iterations described previously need to achieve a reliable solution, never losing sight of the ultimate goal, which is the implementations of the BEMT theory in a GA to obtain an optimum rotor, without a hard penalization on computation time.

To verify the convergence of the BEMT code solutions with the number of iteration the Squire *et al.* [32] rotor were used. For the convergence with the number of rotor blade's divisions both the previous and the Meyer and Falabella [33] rotors were used. Both the cited works address wind tunnel testing of helicopter rotors, having perfectly rectangular blades without torque, and behaving as almost hinge-less in a hover situation. Their principal properties are presented in table 3.2.

The first part of the verification process, is to determine the number of blade elements needed for a reliable results' convergence, so Squire *et al.* rotor is analysed with a pitch angle of the blades (θ) of 8°

	Meyer and Falabella	Squire <i>et al.</i>
R	0.762m	1.829m
c	0.0762m	0.1524m
Ω	800rpm	600rpm
N_b	2	3
root-cut-out	0.124m	0.178m
Aerofoil	NACA0015	NACA0012

Table 3.2: Testing rotors' properties

and various division alternatives with three iterations. The thrust coefficient will be the variable used for the verification and the results for its relative error are present in figure 3.5(a). It can be confirmed that with more than 150 elements the error is inferior to 0.2% and so 150 elements will be used from here on.

The verification of the BEMT code with the number of iterations is showed in figure 3.5(b), where 150 divisions in the blade were used. For more than 3 iterations the error is negligible and so 3 iterations and 150 divisions will be introduced in the future implementation of the BEMT function in the GA.

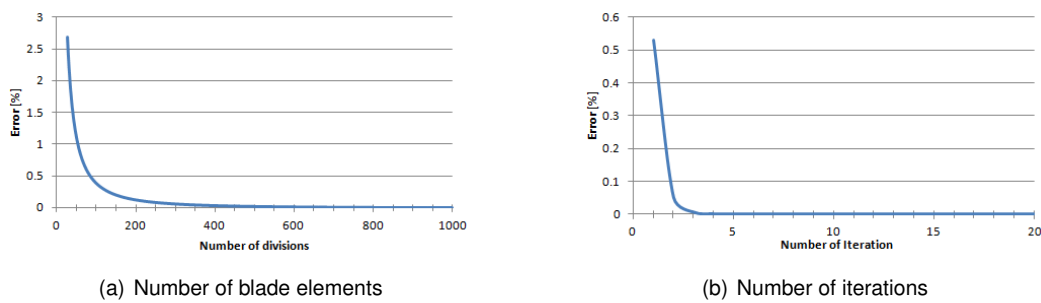


Figure 3.5: BEMT code verification

The validation is then performed comparing the wind-tunnel results by Squire *et al.* [32] and Meyer and Falabella [33] with the BEMT code obtained results for the thrust coefficient (C_T in table 3.3) and power coefficient (C_P in table 3.4), and results will be compared with Pedro's [18] results as well to prove the improvement in the final results by the iterative process implementation.

C_T						
Rotor	θ	Experimental	Pedro's BEMT	Error [%]	new BEMT	Error [%]
Squire <i>et al.</i>	1°	0.00017	0.000181	6.471	0.000181	6.471
	8°	0.00442	0.004720	6.787	0.004686	6.018
	15°	0.01078	0.010914	1.243	0.011198	3.878
Meyer and Falabella	8°	0.00380	0.004048	6.526	0.003907	2.816

Table 3.3: C_T results comparison

We can conclude that the results are somewhat random, in terms of differences between the previous

C_P						
Rotor	θ	Experimental	Pedro's BEMT	Error [%]	new BEMT	Error [%]
Squire <i>et al.</i>	1°	0.000079	0.000066	16.456	0.000017	78.481
	8°	0.000336	0.000361	7.440	0.000356	5.952
	15°	0.001123	0.001140	1.514	0.001211	7.836
Meyer and Falabella	8°	0.000290	0.000297	2.414	0.000294	1.379

Table 3.4: C_P results comparison

BEMT code and the new pseudo-improved one, however this can be easily explained by the validity of the implementations. As the previous tables show for a θ of 1° the power coefficient error provided by the new code has a very large error margin, but this can easily be explained because of the aerofoil's symmetry, for low θ angles and symmetric aerofoils the XFLR5 software does not have a very good definition for the drag coefficient, and thus the large error in the power coefficient remains.

For high θ angles (15°) the error augmented slightly, but for medium angles ($\theta = 8^\circ$) the region where the C_L/C_D has its maximum, as shown in figure 3.1 to be $\theta = 6^\circ$, the new code provides improved results with a smaller error and so it is conclusive that the new code, in the region that is important for this work, near the C_L/C_D maximum proves to be a better option than its predecessor. Mainly because it is around this region that the GA will most likely place the blade's θ distribution.

To finalize the validation the code is tested for Pedro's rotor 5 [18], a small scale 202mm diameter rotor, which was proved the best in the rotor trials performed in his work. And comparing the results in table 3.5 provided by the new BEMT code, the validation is again proved.

	Experimental	Pedro's BEMT	Error [%]	new BEMT	Error [%]
C_T	0.01070	0.01013	5.327	0.010656	0.411
C_P	0.00290	0.001049	63.828	0.001364	52.966

Table 3.5: Small scale rotor's results comparison

As in the original work the C_P value has a large error, resulting from the power measurement being made in the battery, and by the aerofoil's C_D not corresponding to the original rotor's C_D , nonetheless for small rotors, the thrust results have an almost negligible error, between the experimental results and the new BEMT code results, proving that the new BEMT provides reliable and improved results and shall be implemented in the genetic algorithm.

3.1.3 Genetic Algorithm

To find the maximum of a function several methods can be used. In the one variable function case, a simple derivative can provide the solution's coordinate and thus the solution can be easily achieved, however for multi variable functions the gradient methods can become very expendable in terms of computational time and can only find local maximums, instead of the real function maximum, and so

alternative methods were created, being the most successful the genetic algorithm.

The Genetic Algorithm (GA) method was developed by Holland in 1975 [34] and provided a basis for a series of other works such as DeJong's [35] or Wright's [36]. The genetic algorithm can be classified as a heuristic search that emulates the natural evolution process based on the Darwinian principle of survival of the fittest, and is routinely used to generate useful solutions to optimization and search problems. The usual GA starts with the generation of a population of individuals (N_{pop}) with vectorial chromosomes where each variable is generated randomly. Each individual has an associated fitness measure, typically representing an objective value, e.g. the maximum value of the function. The concept that fittest (or best) individuals in a population will produce fitter offspring is then implemented in order to reproduce the next population.

The process starts in the selecting process where an elitism rule can be applied, so that a percentage of the last generation produces offspring (N_{keep}). The most common rules are ranking (choosing the most fitted), roulette-wheel (a value is associated to each individual and they are selected in a weighted process), and tournament (two individuals are randomly selected and the fittest proceeds, the process is repeated until N_{keep} is achieved). The next process is pairing, to form couples from the previous selected individuals; the alternatives used are adjacent fitness pairing, that sorts the individuals by their fitness and mates them in sequence, or best-mate-worst, where the fittest individual mates the worst selected individual, the second mates the last but one and so forth. After the pairing, begins the crossover stage, where new individuals are created to fill the place of the eliminated population in the selecting process, and two alternatives can be used: the arithmetical crossover 3.21(a) and (b) or the intermediate crossover 3.21(c).

$$Son_i = b \times father_i + (1 - b) \times mother_i \quad (3.21a)$$

$$Daughter_i = (1 - b) \times father_i + b \times mother_i \quad (3.21b)$$

$$Son_i = father_i + (b \times (mother_i - father_i)) \quad (3.21c)$$

In both processes a random value b is generated to determine how much of each parent the offspring will receive, the arithmetical crossover creates two descendants from the parents and limits the code usage to $N_{keep} = N_{pop}/2$. The intermediate crossover evades this problem because each pair of parents can have as many descendants as needed to complete the population. The gender chosen is just to illustrate the crossover process, no gender is associated with any of the individuals. Finally a mutation process is used to add new genetic material to the new created population in the crossover stage. The process ends when a predetermined number of generations (N_{gen}) is achieved and the final variable results correspond to the chromosome from the best (fittest) individual from the last generation.

GA implementation

Since Pedro [18] created and validated a working GA with all the processes described above, that same code will be used to find the maximum of the Power Loading function (equation 3.20) for the optimum rotor. A minor alteration was added, because the original code introduced the mutation factor

in all the population, instead of just in the offspring. Being the mutation a random process, the maximum achieved during processing was sometimes erased, and this problem was corrected without altering the rest of the code in any sense, and thus Pedro's validation still applies. The original code was in Octave, and like for the BEMT code a transference to the MatLab[®] language was done, and is shown in appendix C. The code requires the input of the number of generations (N_{gen}), the size of the population (N_{pop}), the percentage of individuals to keep for the next generation (N_{keep}/N_{pop}) and finally the mutation rate. It is then necessary to input what processes (from the described above) shall be used for the in the GA process, what function's variables shall be considered, and also the limits for those variables.

3.2 Aerofoil selection

As defined previously, the average Reynolds number for small rotors is 3.5×10^4 , and so the possible aerofoils suited for the required purpose shall be analysed in this Reynolds number spectrum. The first selection was based on aerofoil's databases, such as the University of Illinois at Urbana-Champaign (UIUC) aerofoil database [37] where high L/D for low Reynolds numbers airfoils were selected for further study, information from Pounds *et al.*[22, 38] was also crucial since an aerofoil optimisation for small scale rotors was conducted for his X-4 Flyer Mark II. The analysis for the aerofoil selection is performed in XFLR5 for the previously cited $Re = 35000$ and the final selection will be made in accordance with the L/D versus α curves in the first draft and adding the C_D versus α curve for a final selection.

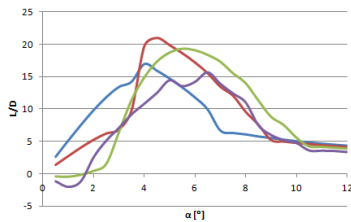


Figure 3.6: L/D versus α for $Re = 35000$ for the NACA aerofoils

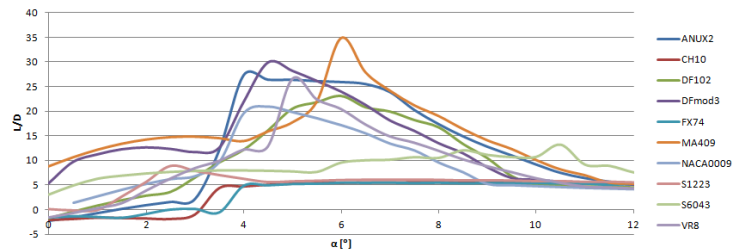


Figure 3.7: L/D versus α for $Re = 35000$ for the selected aerofoils

Since Pedro [18] used a NACA0012 aerofoil, a few NACA aerofoils are tested, with the results for the L/D versus α curve presented in figure 3.6. The NACA0009 provides the best results from all the NACA aerofoils considered, and thus it will be analysed along side with the aerofoils suggested by Pounds, ANUX2, DFmod3, VR8 and MA409sm, as well as the aerofoils provided by UIUC database, CH10sm, FX74-CI5-140MODsm, DF102, S6043 and S1223. All these aerofoils are shown in appendix D and the results are presented in figure 3.7.

The UIUC database although referring to the aerofoils as high L/D for low Reynolds numbers, the results are not as expected; the only exception being the DF102, that like the NACA0009 aerofoil provided good results but 30% inferior to the aerofoils with the best results, MA409, ANUX2 and DFmod3. This was expected since the ANUX2 and DFmod3 aerofoils were created to be utilized in a 4kg quadrotor. To select from these three aerofoils which one is the best alternative, the C_L and C_D versus α curves (figure 3.8) are analysed separately, always with the ultimate goal of building real models in a rapid prototyping

machine of this optimum rotor to be used in the ALIV3.

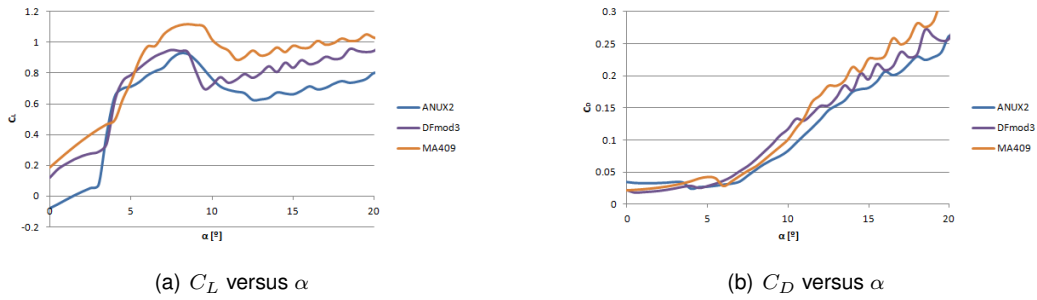


Figure 3.8: C_L and C_D versus α curves for $Re = 35000$

The lowest drag coefficient (C_D) is obtained for the ANUX2 aerofoil, however, all the three aerofoils present very similar results. The higher lift coefficient (C_L) values are clearly achieved by the MA409 aerofoil. The DFmod3 aerofoil has very similar results to ANUX2, yet the thickness of the aerofoil is very small, and so it is very hard to built of a reliable working rotor, and as a result the choice shall be between the ANUX2 and MA409 aerofoils. To make this choice the L/D graphic from figure 3.7 is reanalysis and both aerofoils present advantages.

The ANUX2 has an almost constant baseline maximum, very useful for the GA, while the MA409 has a maximum value of L/D 23% higher than ANUX2 and since the MA409 aerofoil C_L value for low α 's is 0.225 higher than the ANUX2 aerofoil, it was the selected aerofoil for the optimum rotor. The MA409 profile, C_L and C_D versus α curves for several Reynolds number distributions are shown in figure 3.9.

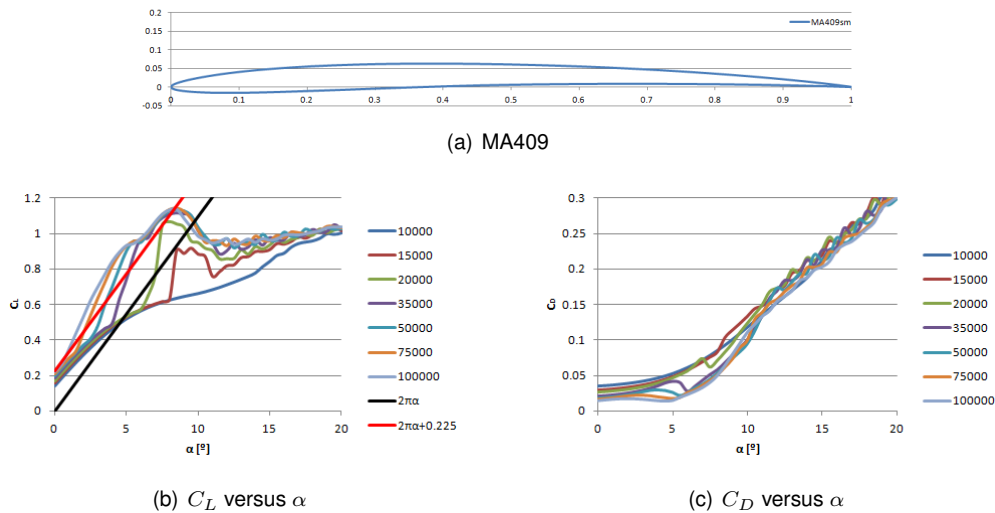


Figure 3.9: Selected aerofoil MA409 profile, C_L and C_D versus α curves for several Re

Analysing the C_L distribution it is confirmed that the implementation of the iterative process was very important, because as shown in figure 3.9(b), the $2\pi\alpha$ line cannot be used to describe accurately the C_L distribution of the selected MA409 aerofoil, instead a $(2\pi\alpha + 0.225)$ would seem more appropriate due to the aerofoil asymmetry, however for low Reynolds numbers neither alternative is viable and acquiring the desired value from XFLR5 is clearly the best option.

3.3 Optimum rotor

For the optimum rotor the new BEMT code is introduced in Pedro's [18] GA. This optimum rotor calculation will be done for hovering conditions ($V_c = \lambda_c = 0$) at a standard sea level ISA atmosphere, and with a root-cut-out of $10mm$, typical of small rotors. The other important aspects required are the variables to estimate, and their limits, since all the other BEMT code properties have been previously determined. Nevertheless here are the BEMT code settings again, presented in table 3.6.

Blade's divisions	150	Number of iterations	3
a_w	0.61	Aerofoil	MA409
λ_c	0	root-cut-out	1cm
ρ	$1.225kg.m^{-3}$	μ	$1.8 \times 10^{-5}kg.(m.s)^{-1}$

Table 3.6: BEMT properties

The variables to be estimated, since the objective is to optimize a rotor, in hovering, will be the geometric and operational parameter of the rotor. Although the BEMT code can generate any kind of rotor, by a polynomial distribution of both the rotor's chord and torsion that option would become very complex, and the convergence to an optimum solution would be hard to achieve and would require many hours of computational time, if not days. So it was decided that the optimum rotor had a linear variation, both in torsion and in chord, to decrease the number of geometric parameter of the rotor to a total of six, the cord at the rotor's blade tip (c_{tip}), the blade taper ratio ($\lambda_{taper} = c_{tip}/c_{root}$), the blade torsion angle at its tip (θ_{tip}) and at its root (θ_{root}), the rotor diameter (D) and the number of blades (N_b) a seventh and final operation parameter will be the rotor's rotation speed (Ω).

The limits for these variables are chosen through empirical data [18, 15, 39], and by analysing existent rotors. In terms of the distribution of chord along the ratio, the small scale rotors usually have between $20mm$ and $40mm$ in the blade's root, diminishing non-linearly to the tip with a blade taper ratio varying from 0.5 to 0.3 that represent $5mm$ and $15mm$ at the blade's tip, however non-conventional rotors can present a parabolic distribution of chord with no blade taper ratio. For the torsion distribution the usual maximum angle is 30° and the small scale rotors usually present linear distributions, as the one considered in this optimization. The diameter will take into account the decisions made in chapter 2 where the swivel arm's dimensions were defined, and considering that the maximum rotor size defined then was $279.4mm$ ($11in$), the maximum diameter possible now is that same dimension. The majority of small scale rotors have two blades, however some models have three-bladed rotors, and so the limits for the number of blades will be placed between 2 and 4 blades. Finally the rotational speed of the rotor will needs to be higher than the minimum for a regular working state ($2000rpm$). In table 3.7 these assumptions are illustrated.

It is also necessary to give the code some restrictions, because if a cold analysis is done regarding what was defined so far, any result could be achieved and the maximization of the PL function would not be accomplished, and so a minimum thrust value must be established, equal to a quarter of the weight

Parameter	Minimum	Maximum
$c_{tip}[m]$	0	0.015
λ_{taper}	0.3	1
$\theta_{root}[^\circ]$	0	30
$\theta_{tip}[^\circ]$	0	30
$D[m]$	0.2	0.279
N_b	2	4
$\Omega[rpm]$	2000	10000

Table 3.7: Limits of the parameters to be estimated

of the ALIV3, that will be considered to be $16N$, because it was the weight the ALIV2 design was aimed to have, and so the thrust of a single rotor must be superior to $4N$. A power limitation should also be imposed to avoid overloads in the avionic components and $100W$ are imposed as the maximum power available for hovering for single motor.

The author of the code suggests that the best alternative for running the GA, and with the fastest convergence, starts with a roulette-wheel selection process, followed by a best-mate-worst pairing with intermediate crossover. To an ideal convergence of the solution the number of generations (N_{gen}) should be as high as possible, but since the total computing time is proportional to N_{gen} this was selected to be 200 as was the size of the population (N_{pop}). The individuals selected for the next generation (N_{keep}) were decided to be 100, and the mutation rate 10%. With these configurations the code takes roughly four hours to complete its run. From the several runs performed, local maximums were sometimes obtained. This was expected due to the large number of variables to estimate, however a result occurred more frequently, and can be considered the true maximum of the PL function, the estimated variables and the important results provided by the optimum rotor are shown in table 3.8.

Parameter	Minimum	Results	
$c_{tip}[m]$	0.011260		
λ_{taper}	0.331147	PL	0.133405
$\theta_{root}[^\circ]$	26.922121	T	4.000238N
$\theta_{tip}[^\circ]$	10.086238	P	29.985481W
$D[m]$	0.278796	C_T	0.016675
N_b	3	C_P	0.002207
$\Omega[rpm]$	3879.928843		

Table 3.8: Optimum rotor properties and results

The optimum rotor obtained follows some tendencies of the market options, like a high blade torsion angle at the root of the blade, decreasing considerably to a final 60% inferior angle at the tip, this result, however expected, was interesting to obtain, since the blade torsion angles (θ) were left completely open

for the code to decide what would be best between 0° and 30° . Another important and expected result was that the diameter approached the scaled limit, as well as the taper ratio. The number of blades converge at three, which can produce more lift than a two-bladed rotor, but also has a more drag, that forces the angular velocity (Ω) to converge at a low value, approximately 40% what would be expected as a maximum rotation limit, making this optimum rotor, a perfect example of a slow flyer rotor.

To compare this optimum rotor with real models or other pseudo-optimum rotors, a power loading comparison varying the total thrust is conducted, for Pedro's experimental rotor 5, which proved to be the best model in his work, and his optimum rotor and the optimum rotor obtained previously. Combining equation 3.20 and 3.14 (c) to take the angular velocity (Ω) out of the equation:

$$PL = \frac{C_T}{C_P R \sqrt{\frac{T}{C_T \rho \pi R^4}}} \tag{3.22}$$

Using equation 3.22 and the properties of the previously used rotors, figure 3.10 is obtained.

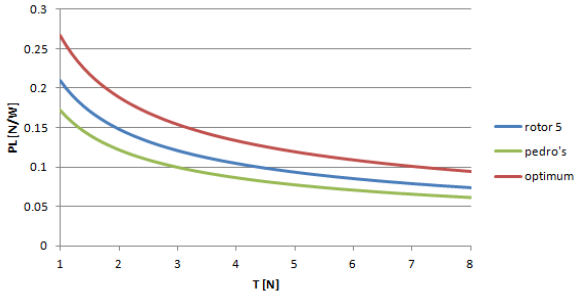


Figure 3.10: PL comparison for real and theoretical rotors

The original Pedro's optimum rotor provided an outstanding improvement of 102.7% in comparison with the best market option tested, his rotor 5, however this optimum rotor had 496mm in diameter, which was impracticable, because as an example, a U-arm (Pedro's ALIV2 had 220mm) of that size would force the total structure span to be greater than one metre. That needed to be corrected to an executable dimension, and his optimum rotor was readjusted to the same diameter as the new optimum rotor, and as the figure demonstrates, the original code was not very useful, since rotor 5 provides better results. Nevertheless the optimum rotor obtained with the new BEMT code has an increase of 27.6% in comparison with rotor 5, proving the added value of the GA process and enabling the execution of the rapid prototyping process for the creation of the optimum rotor's real model as in figure 3.11.

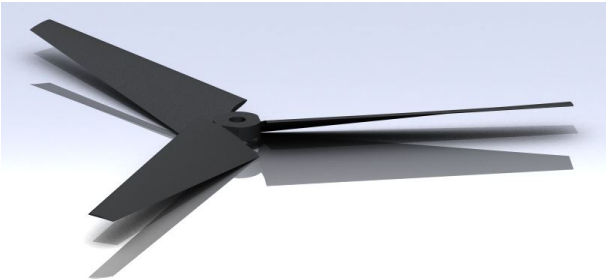


Figure 3.11: Optimum rotor model

Chapter 4

Off-the-shelf Components

Every quadrotor's component can be split in two areas, the electromechanical and the structural. The first area is the one where all components that move, components that command moving parts, components that assist that decision making process or even components that provide power to all other cited parts. In the second area all the structural components of the quadrotor are situated, such as the landing gear, swivel arms or even the central area supports. Although every component can be created, that task is not very practical and the electronic and mechanical components are usually bought (off-the-shelf), and that is the main focus of this chapter. In the structural area a few components were also decided to be off-the-shelf, mainly the fixed arm and swivel arm auxiliaries.

The main objective of this project is to create a functional model in the time frame available, and so in the selection process of the components the main focus for any decision is the price/quality ratio, however national stores should have precedence even with a small penalty in price to any European store, and the European stores should be selected instead of non-European based stores. Nonetheless the whole project must not have an excessive total price, so if a non-European based store presents a better option than all the other competitors that option should have primacy.

4.1 Propulsion Components

The propulsion system is the sole responsible for the lift of the ALIV3, it is composed by a motor, a rotor and its necessary accessory components. As an example for electric brushless motors, an Electronic Speed Control (ESC) is required for every motor. The choice of rotor was already performed in chapter 3, however another rotor option will be necessary because the rapid prototyping process envisioned for the optimum rotor did not materialized, and so a four rotors set, two puller and two pushers should be considered as an alternative solution.

For the motor selection, first it is necessary to decide what technology shall be selected, electric or petrol, and the choice is most obvious, considering the aim of the project. Petrol engines are usually high power engines, for heavy lift and short flights, and another problem is the mass of the fuel they must carry, and so the cheaper, cleaner and lighter electric alternative is the better option. In the electric

market, two new options arise, the brushed motors and the brushless ones. In general, brush-type direct current (DC) motors are commonly used when low system cost is a priority, while brushless motors are used to fulfil requirements such as maintenance-free operation, high speeds, and operation in explosive environments where sparking could be hazardous. On the other hand a brushless DC motor's main disadvantage is higher cost, which arises from two issues. First, brushless DC motors require complex electronic speed control to run. Brushed DC motors can be regulated by a comparatively simple controller, such as a rheostat (variable resistor). However, this reduces efficiency because power is wasted in the rheostat and again the choice becomes simple and the brushless alternative will be the selected one, like other working examples suggest [18, 11, 13, 15, 39, 40].

So three components need to be selected for the ALIV3 propulsion system, a brushless motor, a compatible ESC and an inferior to 279.4mm (11in) rotor, available in the market in both pusher and puller configurations, for the positive and negative rotations needed for the torque annulment. For the motor selection the market provides a wide variety of choices available. The best course of action is to resort to existing functioning models for inspiration and the best alternative for inspiration is the open source quadrotor derivative, the Arducopter [15] that has similar properties, such as mass and span, to the ALIV3's preliminary design. Although useful, using motors from other quadrotors blindly is absurd, and testing several motors and choose the one with best results cannot be considered here due to the budget ceiling, however *FlyBrushless.com* [41] provides a source for comparing different motor models.

The motors for the ALIV3 must be capable to provide the rotor with a thrust $4N$ for hovering, however the ALIV3 must be capable of much more than that and so $8N$ to be able to account manoeuvring and incongruences from the queried results. Three 11.1V motors were the best options from all the other models analysed, and their properties are in table 4.1. In the table are shown the most important aspects of the brushless motors, such as the motor velocity constant (K_v) measured in rpm/V and displays the maximum angular velocity (Ω) the motor is capable of, e.g. an 11.1V motor with a $K_v = 1000rpm/V$ as a maximum $\Omega = 11000rpm$.

	Turnigy 2217 16turn 1050kv 23A Outrunner 	Hacker Style Brushless Outrunner 20-22L 	BP A2217-9 Brushless Outrunner Motor 
$K_v[rpm/V]$	1050	924	950
$i_{max}[A]$	18	17	18
Weight[g]	71	56	73.4
Dimensions (diameter×height)[mm]	36 × 28	32 × 28	34 × 27.8

Table 4.1: Motor properties

All motors present the same generic properties, although the Hacker model has 20% less weight than the Turnigy model that is the one capable of greater rotational velocities, and only with the testing results presented in table 4.2 a reasoned decision can be made. For the test results shown it was tried to present all three motors in the same conditions, *i.e.* with the same rotor, although not possible the rotors selected are very similar, only diverging slightly in the pitch, however the results shown are very much conclusive.

	Turnigy 2217 16turn 1050kv 23A Outrunner	Hacker Style Brushless Outrunner 20-22L	BP A2217-9 Brushless Outrunner Motor
Rotor	9 × 5	9 × 6	9 × 6
Current (i) [A]	12.4	10.5	21.7
Voltage (U) [V]	10	11	11.42
Power (P) [W]	124	115.5	247.8
Thrust (T) [g]	757	600	936
Ω [rpm]	8936	7500	7650
Thrust-to-Power ratio [g/W]	6.105	5.195	3.777
Price [€]	11.30	10.82	15.53

Table 4.2: Selected motors test results

The crucial parameter for the selection is chosen to be the Thrust-to-Power ratio in which the highest value represents the motor that can make the rotor produce the most thrust with less power. The motor with the best result is the Turnigy model, although heavier than the Hacker model, can produce a higher total thrust and since it has a higher Thrust-to-Power ratio will have a better endurance than the competition, and so four Turnigy 2217 16turn 1050kv 23A Outrunner were ordered¹.

Now it is necessary to select a compatible ESC to control the motor rotation. Since these components are known to start burning, a 50% security margin was chosen to avoid any unexpected burnings or malfunctions. The selected model has a maximum current of 18A and so the ESC must support at least a current of 27A, and two models were selected as the best alternatives and are present in table 4.3

Since both ESC's can support the desired current, and have a similar size, the deciding factor for choosing the ESC will be the price and so the Hobbyking SS Series 25-30A ESC² is the best option, furthermore has a slight 12% weight advantage.

The extra rotor set was a very hard component to select, because the market provides a wide variety of options but only in the pusher format, for model airplanes, almost never existing a puller equivalent, and when a pusher-puller set was indeed available, the selling price was very high. So the choice was limited to the store where the other already described components were selected and a set of rotors proved to be the better solution, both in terms of price, and of extra parts, the 10X6 Propellers (Standard

¹http://www.hobbyking.com/hobbyking/store/uh_viewItem.asp?idProduct=5690

²http://www.hobbyking.com/hobbyking/store/uh_viewItem.asp?idProduct=6460

	TURNIGY Plush 30amp 23A Outrunner	Hobbyking SS Series 25-30A ESC
		
Continuous Current [A]	30	25
Burst Current [A]	40	34
Weight [g]	25	22
Dimensions [mm]	$45 \times 24 \times 11$	$52 \times 24 \times 6$
Price [€]	8.96	4.40

Table 4.3: ESC properties

and Counter Rotating) 6pc set³, a pack of three pushers and three pullers 10x6 rotors, was selected for the spare rotors role.

4.2 Servos

Four servos are required for the ALIV3, in both the U-arm or the slim-arm configuration. These control the tilt of the rotors, with two first-servos and two second-servos, and it is expected that the torque the first-servo will be forced to do, to rotate all the arm, to be superior to the torque the second-arm has to do, to just rotate the motor-rotor couple, yet to standardize the selection process, all the four servos will be the same model. To determine the maximum moments a three dimensional rigid body dynamics theory must be introduced, and the MIT Open Course on Dynamics [42] will serve as the theoretical background for the servo's maximum torque determination.

The most similar situation to a rotating motor is a gyroscope, and so in figure 4.1 are shown its body-fixed frame (x'', y'', z'') and its inertial frame (X, Y, Z) , different from all the axis presented do far, with $\dot{\psi}$ representing the rotor's angular speed, θ the angle of rotation induced by the second-servo, the servo that just rotates the rotor and ϕ the arm's rotation angle, induced by the first-servo. The ψ rotation is not considered and so the body-fixed frame can be considered the (x'', y'', z'') frame and the moment in x'' ($M_{x''}$) will be the moment that the second-servo must overcome.

The other moment of interest, the one that the first-servo must overcome is in the inertial frame (X, Y, Z) , and in the Z -axis, so this M_Z moment (theoretically) will be the guideline for the servos selection. To switch from the inertial frame to the body-fixed frame the first rotation is the one by ϕ from the inertial frame (X, Y, Z) to the intermediate frame (x', y', z') . The second rotation, by θ from the intermediate frame to the body-fixed frame (x'', y'', z'') . The corresponding matrices (\tilde{T}_1 and \tilde{T}_2 respectively) can be found in appendix E.

³http://www.hobbyking.com/hobbyking/store/uh_viewItem.asp?idProduct=11333

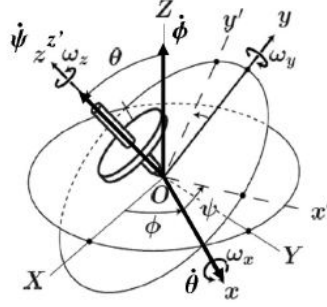


Figure 4.1: Gyroscope motion axis

For the general motion of a three-dimensional body, Euler's equations in the body-fixed axes which rotate with the body, so that the moment of inertia is constant in time are used. The selecting of this body-fixed frame is done to maintain the moments of inertia constant in time ($\frac{d}{dt}I = 0$), however this frame being a rotating coordinate system the application of the Coriolis theorem is mandatory and the applied moments are:

$$\sum \vec{M}_O = \left(\dot{\vec{H}}_O \right)_{Oxyz} + \vec{\Omega} \times \vec{H}_O \quad (4.1)$$

This expression is valid only for the origin of the body-fixed frame and \vec{H} represents the angular momentum given by $\vec{H} = [I]\omega$. The angular velocity in the body-fixed frame (ω) will be:

$$\vec{\omega} = \dot{\theta} \vec{e}_{x'} + \dot{\psi} \vec{e}_{z''} + \dot{\phi} \vec{e}_Z \quad (4.2)$$

Using the rotation matrices the angular velocity in the body-fixed frame is:

$$\vec{\omega} = [\tilde{T}_2] \dot{\theta} \vec{e}_{x'} + \dot{\psi} \vec{e}_{z''} + [\tilde{T}_2][\tilde{T}_1] \dot{\phi} \vec{e}_Z \vec{\omega} = \dot{\theta} \vec{e}_{x''} + (\dot{\phi} \sin \theta) \vec{e}_{y''} + (\dot{\psi} + \dot{\phi} \cos \theta) \vec{e}_{z''} \quad (4.3)$$

$\vec{\Omega}$ is the angular velocity of the body-fixed frame system, and is given by:

$$\vec{\Omega} = \dot{\theta} \vec{e}_{x''} + (\dot{\phi} \sin \theta) \vec{e}_{y''} + (\dot{\phi} \cos \theta) \vec{e}_{z''} \quad (4.4)$$

Using equation 4.1 the moment in the x'' -axis, relevant for the second-servo is:

$$\begin{aligned} M_{x''} = & I_{xx} \ddot{\theta} + I_{xy} (\ddot{\phi} \sin \theta + \dot{\phi} \dot{\theta} \cos \theta + \dot{\theta} \dot{\phi} \cos \theta) + I_{xz} (\ddot{\psi} + \dot{\theta} + \ddot{\phi} \cos \theta - \dot{\phi} \dot{\theta} \sin \theta) \\ & - I_{yz} \dot{\phi} (\cos \theta (\dot{\psi} + \dot{\phi} \cos \theta) + \sin \theta) + I_{yy} \dot{\phi}^2 \cos \theta \sin \theta + (I_{zz} \dot{\phi} \sin \theta (\dot{\psi} + \dot{\phi} \cos \theta)) \end{aligned} \quad (4.5)$$

Simplifying for the axisymmetric case, where I is the moment of inertia around the axis of rotation (I_{zz}) and I_0 the moment of inertia in the transverse axis ($I_{xx} = I_{yy}$). The products of inertia I_{xy} , I_{xz} and I_{yz} are all null.

$$M_{x''} = I_0 (\ddot{\theta} - \dot{\phi}^2 \sin \theta \cos \theta) + I \dot{\phi} (\dot{\psi} + \dot{\phi} \cos \theta) \quad (4.6)$$

As for the moment the first-servo's torque must overcome, it is necessary to transpose the applied

moment equation to the intermediate frame, so that Z and z' coincide.

$$\begin{aligned}
M_Z &= M_{z'} \Rightarrow \{M_I\} = [\tilde{T}^2]^{-1} \{M_{i''}\} \\
M_Z &= \sin \theta M_{y''} + \cos \theta M_{z''} \\
M_Z &= I_{xz}(\cos \theta \ddot{\theta} + \dot{\theta} \dot{\theta} \sin \theta) + I_{xy} \dot{\theta}(\cos \theta \dot{\theta} + \sin \theta \ddot{\theta}) + I_{yy} \sin \theta(\ddot{\phi} \sin \theta + 2\dot{\theta} \cos \theta \dot{\phi}) \\
&\quad + I_{zz}(\cos \theta(\ddot{\psi} + \ddot{\phi} \cos \theta) - \sin \theta \dot{\theta} \dot{\psi}) + I_{yz}(\cos \theta(\cos \theta \dot{\theta}(\dot{\psi} + \dot{\phi}(1 + \cos \theta)) + 2 \sin \theta \dot{\phi}) + \sin \theta \dot{\theta} \dot{\psi}) \quad (4.7)
\end{aligned}$$

Now it is important to determine the moments of inertia for the motor and rotor for the axisymmetric case. The rotor used will be the one determined in the optimum rotor chapter 3, and the motor will be the Turnigy model previously selected. The moment of inertia for the z -axis is given by $I_z = \int (x^2 + y^2) dm$ with $dm = \rho t dx dy$, and for a rotor's blade is:

$$I_{z_{blade}} = \int_{r_0}^R \int_{-c(r)/2}^{c(r)/2} (x^2 + y^2) \rho t dx dy \quad (4.8)$$

With $r = \bar{y}/R$, $r_0 = r_{root.cut.out} = 1cm$, $R = 13.94cm$, $c(r) = c_{tip}(r + \frac{1-r}{\lambda_{taper}})$, $t = .0669c(r)$ and $\rho = 700kg.m^{-3}$ from the optimum rotor. For the motor a cylinder approximation can be performed, with the mass of the motor ($m = 71g$) and $r = 13.8mm$ from table 4.1, the inertia is:

$$I_{z_{motor}} = \frac{mr^2}{2} \quad (4.9)$$

The inertial moment in the rotational axis ($I = I_z$) is:

$$I = 3 \times I_{z_{blade}} + I_{z_{motor}} = 3 \times 1.31 \times 10^{-5} + 6.76 \times 10^{-6} = 4.61 \times 10^{-5} kg.m^2 \quad (4.10)$$

The transverse inertial moment $I_0 = I_x = I_y$ since the rotation centre is not the same as the origin of the axis, it is necessary to use the parallel axis theorem, $I = \bar{I} + md^2$ and in place of the mass, the equivalent thrust produced by the motor will be used, in this case the double of the hovering thrust, to account for a reasonable safety margin, the distance is the height of the rotor ($36mm$).

$$I_0 = \bar{I}_0 + md^2 = \frac{I}{2} + md^2 = 1.06 \times 10^{-3} kg.m^2 \quad (4.11)$$

The previous calculated inertial moments refer to the second-servo maximum torque, for the first-servo is mandatory to determine also the arm's inertial tensor, and for both situations the angular derivatives must be determined. The several angular velocities and accelerations will be the maximum the motor can provide or the maximum medium-size rotors offer, and is expected that in operating situations these magnitudes will never be approached. The inertia tensors for both arm's alternatives were also calculated with the SolidWorks® models from chapter 5 and all these values are presented in appendix E.

Computing all these properties with the theory described, figures 4.2 are obtained to describe the necessary servo's torque. In this figure, a θ angle of 90° corresponds to the hovering position of the

ALIV3, and is noticeable the assumptions made before, about what servo would need a greater torque.

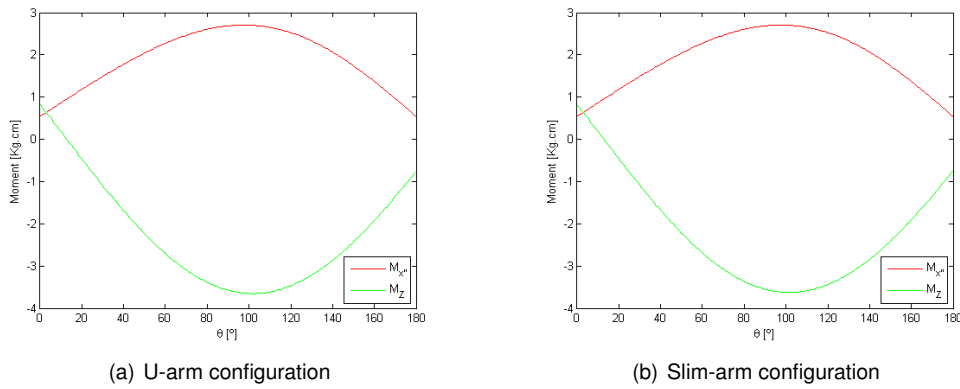


Figure 4.2: Moments the servos have to overcome

As expected the maximum torque required occurs for the first-servo, the servo that must rotate all the arm. Also the U-arm alternative is the arm's configuration that requires a slightly larger, and stronger servo. However since servos are quite expensive components only four servos will be obtained, and with both arm alternatives constructed the servos must be dismantled and reutilized in the other arm. The noticeable offset in the $M_{x''}$ is due to the direction of the force produced by the rotor, while the offset of θ for M_Z is a product of the different angular velocities and accelerations in the system.

Since large tolerances have been applied both in the angular velocities and accelerations estimations and in the rotor's force, the selected servo model must have a torque superior to $3.69kg.cm$, the absolute maximum from figures 4.2. The maximum torque was obtained for the U-arm alternative, but only 1.65% superior to the slim-arm results ($3.63kg.cm$). In accordance with the previous notions Futaba S3003 Standard⁴ was the selected servo, its dimensions and important properties are described in table 4.4.

Futaba S3003 Standard		
	Torque [$kg.cm$]	4.1
	Stall Torque [$s/60^\circ$]	0.19
	Weight [g]	37.2
	Idle current [mA]	8
	Dimensions [mm]	$41 \times 20 \times 36$
	Price [€]	13.53

Table 4.4: Servo properties

4.3 Avionics

The avionics are one of the trickiest choices in the selection process of a quadrotor's components, because this section not only comprise the brains of the aircraft, in the form of a microprocessor, but

⁴http://www.somodelismo.com/product_info.php?cPath=14_68&products_id=2205

also all its senses, in the form of gyroscopes, accelerometers, magnetometers, pressure sensors or even a GPS tracking device, and if the components are not compatible, or if the brains work in a too slow manner, a steady and controlled flight cannot be achieved. So the main focus on this selection has to do with compatibility and complementarity of all the avionics.

Starting with the microprocessing unit, the goal was to have a fast processor with at least eight outputs for the servos and the motors (four each), and that the platform can be easily programmable. The best option available is the ArduPilot Mega⁵, that can provide all the output needs of the project, but also has a strong ATmega2560 16MHz processor, and the decisive factor, to be part of the open-source arduino family, the best in existence so far, capable of uploading software available on-line, and since the quadrotor is a subject of universities investigation as well as many aeronautics enthusiasts, a great number of conventional quadrotor control software is available and can be an advantage for a future ALIV3 control.

Although the Ardupilot Mega can control the direction of movement of the ALIV3, without any sensors the microprocessor is totally flying blind. For attitude control gyroscopes in the three directions are needed for angular velocity determination, a three-dimensional accelerometer is required for the microprocessor calculate the ABC's frame z direction, so the ALIV3 can "know" where down is. For an advance control system, where the real position on Earth is important a GPS device is mandatory to determine the ALIV3's position and finally a magnetometer to determine the true North and assist the GPS.

The arduinos are designed to interact with a shield, placed on top of them, and the selection of the ArduPilot Mega proves quite useful because it has a perfect matching ArduPilot Mega IMU Shield⁶ that was intentionally created, in conjunction with the ArduPilot Mega as a hardware for a conventional quadrotor control platform. This shield has a built in pressure sensor, for redundant altitude determination, a three-dimensional gyroscope for attitude control, a three-dimensional accelerometer, extra entries for a magnetometer connection, a Xbee communication system, direct USB entry and a relay for a camera, dropping objects or other triggered events.

And so a pack⁷ containing both the Ardupilot Mega and its IMU Shield plus a MediaTek MT3329 GPS 10Hz⁸ is obtained for a future control development of the ALIV3, however a magnetometer is missing and since all components have been inspired by the Arducopter project [15] the magnetometer from this model shall be the one selected, the HMC5843 - Triple Axis Magnetometer⁹. The supracited GPS can be directly connected to the Ardupilot Mega. The dimensions and major properties of all these components are described in table 4.5.

⁵http://store.diydrones.com/productdetails_popup.asp?productcode=BR-ArduPilot-01

⁶http://store.diydrones.com/productdetails_popup.asp?productcode=BR-0012-01

⁷http://store.diydrones.com/ArduPilot_Mega_kit_p/kt-apm-01.htm

⁸http://store.diydrones.com/productdetails_popup.asp?productcode=MT3329-02

⁹<http://www.sparkfun.com/products/9371>

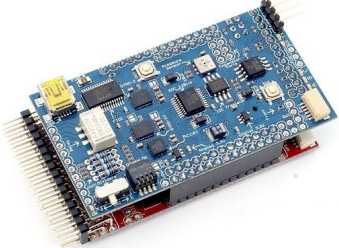
	Ardupilot Mega (red)	ArduPilot Mega IMU Shield (blue)	MediaTek MT3329 GPS 10Hz	HMC5843 - Triple Magnetometer
				
Dimensions [mm]	69 × 40 × 12		16 × 16 × 6	12.7 × 12.7 × 3
Weight [g]	60.7		8	5
Price [€]	236.10			46.68

Table 4.5: Avionic component properties

4.4 Communication

One of the final objectives of every quadrotor project is to transform it into an UAV, however in this stage of the project the ALIV3 must be controlled by an user, and two options will be left open, since the Ardupilot Mega plus IMU Shield has two separate long range communication alternatives available to explore. The first is the most common way to control any model aircraft, via a radio control (RC) receiver connected to the inputs of the Ardupilot Mega, which in addition to the eight outputs described before, also has eight inputs that can be connected to the RC receiver to transmit the information from an RC controller to the ALIV3 and perform the user's desired manoeuvres.

The second alternative is to connect the ALIV3 wireless to a computer and control the aircraft's movements with the aid of one or more joysticks, to complete that connection compatible wireless apparatus are needed in both ends of the connection, and the Xbee wireless system proves the best, mainly because it has a standard, from origin, compatibility with the Ardupilot Mega. So two Xbees are needed, one to connect to the computer, and another one to connect to the ALIV3's Ardupilot Mega, however the so called Xbee regulators are required to complete the connection. This communication system, although expensive is much more practical than the RC communication, because a live feed with the computer is established which open a new range of possibilities, *e.g.* a video camera live feed.

In Pedro's work all the aspects needed for the RC communication (RC controller and RC receiver) were taken care off, here only the second option will be addressed. The choice of the Xbee alternative is mostly based on the range of the communication it allows, being chosen the one mile (1.5Km) radius model, the XBee PRO 60mW Wire Antenna¹⁰, because the inferior models only allowed for 100m range, that considering the price difference (6.15€) the choice was made easier.

The remaining components are a universal one of a kind very similar models. The connection to the computer will be made by a XBee Explorer USB¹¹ that, like the name suggests, enables a USB

¹⁰http://www.inmotion.pt/store/product_info.php?products_id=64

¹¹http://www.inmotion.pt/store/product_info.php?cPath=7&products_id=52

connection with the XBee, the connection with the ALIV3 is made by a XBee Explorer Regulated¹² board. All components chosen are presented in table 4.6 where the XBee Explorer USB properties are also described but not relevant in the ALIV3 projection and construction.

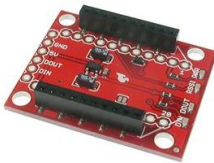
	XBee PRO 60mW Wire Antenna	XBee Explorer Regulated	XBee Explorer USB
			
Dimensions [mm]	33 × 25 × 4	36 × 28 × 6	36 × 28 × 6
Weight [g]	5	6	6.5
Price [€]	42.44	10.39	25.67

Table 4.6: Communication component properties

4.5 Battery

The selection of a battery is made based on two decisive project aspects, the endurance and maximum current needed, and both these variables are directly related to the motor. For the selected Turnigy motor model, the maximum input current required is 18A which leads to a total of 72A that the battery needs to be capable of supplying. For the endurance, the project required a minimum of seven minutes airborne, and using the values for hovering from the optimum rotor, the power needed for a hovering state by just one motor is 29.985W, thus in four motors is obtained 119.94W, that leads to a total current required (using the voltage value of the motor, 11.1V) of:

$$P = Ui \Rightarrow i = \frac{P}{U} = \frac{119.94}{11.1} = 10.805A \quad (4.12)$$

never forgetting that this value was obtained considering a total ALIV3 weight of 1.6kg. It is important to consider a safety power loss factor for all the other components, such as servos, avionics and losses by joule effect in the cabling; also for a hovering situation the ALIV3 will not always be in a perfect stable position, and changes in the motor's velocity or position may need to be executed, and these minor corrections also consume some current and should be also considered for the safety power loss factor.

For each servo a 1A current can be a conservative estimate, since the idle current is supposed to be 8mA, nevertheless that was the value suggested by Severino. For the remaining avionics, and changes in motor velocity a conservative estimation of 3A will be used, and for the joule effect losses 1A is a reasonable value. The safety power loss factor becomes a total of 8A and the total current needed

¹²http://www.inmotion.pt/store/product_info.php?products_id=215

comes up to a total of $i_{hover} = 18.805A$, a slightly higher value however with a good enough margin for unexpected situations.

The type of battery was chosen to be a lithium polymer (LiPo or Li-poly) battery, the most common type of battery used nowadays in a wide variety of different technologies, such as PDAs, laptops, model cars, planes or quadrotors, and even electric urban vehicles. The LiPo batteries are composed of several identical secondary cells in parallel addition, each cell with a voltage of $3.7V$, resulting for the ALIV3 case, to match the motor's voltage requirements, in the need for a three-cell LiPo battery ($11.1V$). The other two characteristics of the LiPo batteries are the nominal capacity ($Cap[mAh]$) and the maximum current discharge rate ($C[h^{-1}]$) given as a ratio of maximum current over the nominal capacity.

To estimate the minimum nominal capacity needed it is only necessary to use the current for hovering ($18.805A$) and the minimum endurance required value.

$$Cap_{min} = I \times Endurance = 18805mA \times \frac{10min}{60} = 3134mAh \quad (4.13)$$

This way the minimum values for the determination of the required battery are found. The possible LiPo battery alternatives must be a three-cell $11.1V$ with maximum current greater than $72A$ and a capacity above $3134mAh$, furthermore must be as light as possible, so it would not compromise the $1.6kg$ total weight estimate.

The maximum current discharge rate limit is determined based on both the maximum current and nominal capacity, and must be above the line of figure 4.3. The usual market LiPo battery alternatives regarding the value of C are always multiples of 5, and the battery choice must respect the C limit illustrated or it will not provide the required maximum current.

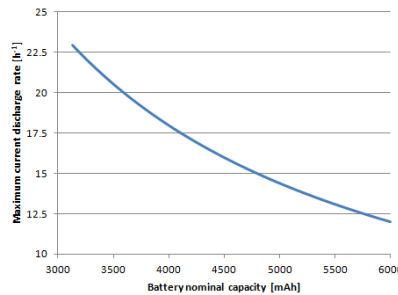


Figure 4.3: Maximum current discharge rate limit

This study indicates that a 20C battery must have a capacity above $3600mAh$ and for a 15C battery the capacity must be greater than $4800mAh$. Considering the previous assessment a study of the batteries weight versus their capacity is made for various maximum current discharge rates (figure 4.4) and the batteries with the best results are more thoroughly compared in table 4.7.

The maximum current is determined by $i_{max} = Cap \times C$ and the endurance is calculated with each battery capacity and the required current for hovering $Endurance = Cap/i_{hover}$. All batteries are very good options and accomplish the desired goals, however one of them, although having a greater penalty in the total weight of the ALIV3, also has the best result for the endurance, being the one with the largest capacity, so the decisive factor was actually the price of the component, and the ZIPPY Flightmax

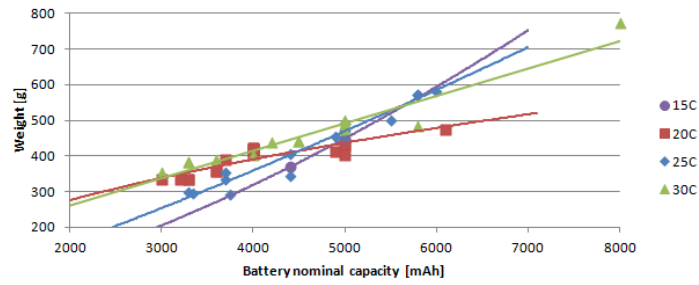


Figure 4.4: Battery capacity versus its weight for various C values (Real values and tendency lines)

5000mAh 3S1P 20C¹³ was the selected battery for the ALIV3.

	Polyquest 3750mAh 3S 25C Lipoly (Version 2)	Polyquest 4400mAh 3S 25C Lipoly (Version 2)	ZIPPY Flightmax 5000mAh 3S1P 20C
			
Capacity [mAh]	3750	4400	5000
C [h^{-1}]	25C	25C	20C
Maximum Current [A]	93.75	110	100
Endurance [min]	11.95	14.04	15.95
Weight [g]	293	345	404
Dimensions [mm]	158 × 49 × 22	169.0 × 48 × 21.5	145 × 52 × 25
Price [€]	38.23	45.83	19.64

Table 4.7: Battery properties

In regular RC plane models the battery is usually directly connected to the motor, yet in ALIV3 due to the four motors and the extra servos that is not executable, because aside from all the four motors, also the servos and remaining electrical components need an electrical input from the battery, and so another battery-related component, the Power Distribution Board (PDB) is necessary to conduct the battery's energy where it needs to be in the amounts each component requires, because the motors work at 11.1V while the servos work in the 4.8V to 6V range and the avionics between 3.3 and 5V. A custom made component to complete this task could be created, however there is an option market that avoids such an endeavour, the Quad Power Distribution PCB¹⁴ described in table 4.8.

¹³http://www.hobbyking.com/hobbyking/store/uh_viewItem.asp?idProduct=8579

¹⁴<http://store.jdrones.com/product.p/quadpdpdb1.htm>

Quad Power Distribution PCB

	Weight [g]	9.5
	Dimensions [mm]	60 × 60 × 3
	Price [€]	10.26

Table 4.8: PDB properties

4.6 Structural Components

In chapter 5 a structural analysis will be performed to all the custom made parts required in the ALIV3, however some structural components do not require such an elaborate design and can be made out of off-the-shelf elements, such as the fixed arm, some swivel arm components and the landing gear skis. For all the arm's alternatives, fixed or both swivel arms, the maximum stress will occur for the fixed arm, where the distance between the embedding point and the force application position is greater. Considering chapter 2 where the arm's span was set at 600mm and a minimum central area of 100mm , the force's arm will be 250mm length. By Beer *et al.* [43] the normal stress (σ) and deflection (w) for a cantilever beam edge is given by:

$$\sigma = \frac{Mz_S}{I} = \frac{Flz_S}{I} \quad (4.14a)$$

$$w = \frac{Fl^3}{3EI} \quad (4.14b)$$

with z_S as the cross section position. It is also important to determine what material can provide the best results, considering that the maximum deflection must be inferior to 5mm and the structural safety factor $SF = \sigma_R / \sigma_{max}$ above 2. Only materials used in RC models will be considered in table 5.1. In the composite materials case (High Tenacity (HT) carbon or glass fibres) the unidimensional longitudinal configuration with an epoxy resin matrix ($V_m = 0.4$) is used. All properties coming from the Matweb database [44]. Aluminium being an orthotropic material, its properties are simplified.

Material	$E_L[\text{GPa}]$	$E_T[\text{GPa}]$	ν_{TL}	ν_{LT}	$G_{LT}[\text{GPa}]$	$\sigma_R[\text{MPa}]$	$\rho[\text{kg}\cdot\text{m}^{-3}]$
Aluminium (6061)	70		0.33		26	124	2700
HT carbon composite	139.80	10.93	0.34	0.23	3.91	1240	1530
E-glass composite	46.20	10.30	0.31	0.72	3.72	1000	2040

Table 4.9: Material properties

Being the lightest, the stronger and the one with the best elastic properties, the carbon fibre alternative proves to be the best, remains only to choose the cross-section for the arms, and the most common market options are tubes (that were considered in all ALIV3 shape explanations so far), rods and strips. Evaluating several market options for the HT carbon fibre, table 4.10 is obtained, with the properties from table 5.1, equations 4.14, an hypothetical maximum force produced by the rotor of 10N and $l = 0.25\text{m}$.

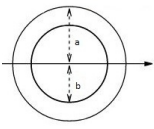
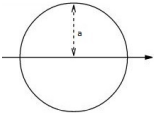
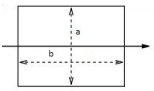
Section	$a[mm]$	$b[mm]$	$I[mm^4]$	$\sigma_{max}[MPa]$	SF	$w[mm]$	$S[mm^2]$
	5	4.5	168.81	74.05	16.75	2.21	14.92
	5	4	289.81	43.13	28.75	1.29	28.27
	3	2.5	32.94	227.70	5.446	11.31	8.64
	2.5	-	30.68	203.72	6.087	12.14	4.91
	10	2	6.67	1875.00	0.661	55.88	20.00

Table 4.10: Arm section determination

The cross section area (S) is shown because the total mass of the arm will be proportional to that same area, and based on this fact and the maximum deflection limit, the ideal arm alternative is a 10 by 9mm in diameter on the cross section, HT carbon tube that shall be used in the fixed arm and both swivel arm alternative connections. The skis, being only a rebalancing mechanism the 5mm rod is the more suited alternative, due to its low weight and ease of construction it allows.

4.7 Extra Components

For advanced mission scenarios obtaining live feed video can be a pre-requisite, however this being an accessory component, an extensive study was not of the uppermost importance, although a micro-camera model was selected as a guideline for future implementations, the CMOS Camera Module - 640x480¹⁵ described in table 4.11.

CMOS Camera Module - 640x480		
	Resolution	640 × 480
	Dimensions [mm]	34 × 34 × 41
	Weight [g]	15
	Price [€]	45.79

Table 4.11: Camera properties

Finally a pair of 10mm inner diameter bearings are necessary, to allow the rotation of the first-servo tube, while keeping the swivel arm perfectly levelled by restraining the lateral motions, originated from vibrations or poor construction tolerances. The bearings are also important to transmit all of the swivel arm's transversal loads to the central board instead of being concentrated at the servo joint. The bearings outer diameter is 22mm and their weight is 9.5mm.

¹⁵http://www.inmotion.pt/store/product_info.php?cPath=17.32&products_id=102

Chapter 5

Design and Construction

The design in any project is an iterative process, where all elements must be combined to achieve a catalytic effect and a perfectly working system. In this process many alternatives for every components are made, and by any means the parts created for this project are absolutely adequate for their role, in theoretical or practical construction terms. Being a first version prototype, the objective was to create a study platform, with space for improvement, but at the same time that worked according to the predetermined requisites, and this final prototype will be discussed ahead; first it is important to introduce both the technical and practical theories behind the laminate composites manufacturing.

5.1 Theoretical principles

5.1.1 Laminated composites

Composite materials exist everywhere, even trees are composites, and can be described as any material composed of at least two elements working together to produce material properties that are different to the properties of each element *per se*. In practice, most composites consist of a bulk material, called the matrix, and a reinforcement, usually in fibre form, added to increase the strength and stiffness of the matrix. Resin systems such as epoxies and polyesters have limited use for the manufacture of structures on their own, since their mechanical properties are not very high when compared to, for example, most metals. However, they have desirable properties, most notably their ability to be easily formed into complex shapes, and these examples are usually used on laminated composites as matrix.

For the fibre role extremely high tensile and compressive strength materials are used such as glass, aramid or carbon, yet fibres alone can only exhibit tensile properties along the fibre's length, and by combining the two totally different material types, exceptional properties can be obtained. The resin matrix spreads the load applied to the composite between each of the individual fibres and also protects the fibres from damage caused by abrasion and impact. The major advantages that composite materials present are high strengths and stiffnesses, ease of moulding into complex shapes, high environmental resistance and low densities, making the composites superior to metals for many applications.

Both glass and HT carbon fibre plain woven fabrics are available for this project; however in the

previous chapter it was determined that the carbon fibre is superior to the glass fibre in every aspect, and because of that it will be the selected material for the parts' construction. The matrix available is epoxy resin and both elements' properties are described in table 5.1.

Material	$E[GP a]$	ν	$G[GP a]$	$\sigma_R[MP a]$	$\rho[kg.m^{-3}]$
HT carbon fibre	230	0.3	50	3200	1750
Epoxy resin	4.5	0.4	1.6	130	1200

Table 5.1: Composite elements properties

A laminate composite plate is nothing more than a superposition of various laminae, and to determine each of the laminae properties the classical laminate theory [45, 46] is used:

$$\begin{aligned}
 \text{Gram weight } [g.m^{-2}]: & \quad gram = \frac{\rho_f V_f}{h_i} \\
 \text{Matrix Volume fraction:} & \quad V_m = 1 - V_f \\
 \text{Density } [kg.m^{-3}]: & \quad \rho = \rho_m V_m + \rho_f V_f \\
 \text{Longitudinal Elasticity } [Pa]: & \quad E_L = V_m E_m + V_f E_f \\
 \text{Transverse Elasticity } [Pa]: & \quad E_T = \left(\frac{V_f}{E_f} + \frac{V_m}{E_m} \right)^{-1} \\
 \text{Torsion Modulus } [Pa]: & \quad G_{LT} = \left(\frac{V_f}{G_f} + \frac{V_m}{G_m} \right)^{-1} \\
 \text{Poisson ratio (LT):} & \quad \nu_{LT} = \nu_f V_f + \nu_m V_m \\
 \text{Poisson ratio (TL):} & \quad \nu_{TL} = \frac{E_T}{\nu_{LT} E_L}
 \end{aligned}$$

The carbon fibre woven available has a gram weight of $205g.m^{-2}$ and each laminae is $0.1667mm$ in thickness, resulting in the laminae properties described in table 5.2, the rupture stress subscripts, T and C refer to traction and compression.

$V_f =$	0.698	$E_L =$	161.9GP a	Rupture Stress (MPa)			
$V_m =$	0.302	$E_T =$	14.26GP a	$\sigma_{Lt} =$	1240	$\sigma_{Lc} =$	1200
$\rho =$	1584kg.m ⁻³	$\nu_{LT} =$	0.330	$\sigma_{Tt} =$	41	$\sigma_{Tc} =$	170
$G_{LT} =$	5.109GP a	$\nu_{TL} =$	0.267	$\tau_{LT} =$		60	

Table 5.2: Laminae properties

These will be the properties of all the laminae of this project, and the golden rule to construct a good laminate composite, is to use a symmetric layout of the laminae, and so from henceforth and when possible, every millimetre in thickness of any component will have a $[0/90/45/-45/90/0]$ layup. Since the material used is a carbon fibre woven, the layup rules dictate that $[0/90/45/-45/90/0]_2 = [0/90/45/-45/90/0]_S$, the 2 means there are two identical layers, while the S means there are two symmetrical layers, because there is no distinction between intertwined layers. Finally it is mandatory to introduce that laminate composites do not fail like metals or other materials, the fibres do not strain hardening due to plastic deformation and the fibres will collapse when the rupture stress is achieved. Since in a laminate, every laminae can have a singular fibre inclination, a good failure criteria is necessary

to determine when the laminate breaks. Several different criteria have been created, and the best alternative for anisotropic composite materials with different strengths in tension and compression is the Tsai-Wu failure criteria:

$$F_i\sigma_i + F_{ij}\sigma_i\sigma_j \leq 1 \quad (5.1)$$

The laminate construction and all the calculations needed for a precise design, below the failure criteria, will be done in ANSYS® [47], a FEM analysis software with proved results and wide acceptance in the aerospace industry.

5.1.2 Finite Element Method (FEM)

The finite element method [48] was first developed by Hrennikoff in 1941 where a continuous domain discretized into a mesh of sub-domains, called elements, to solve a complex elasticity and structural analysis.

The FEM is a numerical technique for finding approximate solutions of partial differential or integral equations. The solution approach is based either on eliminating the differential equation completely (steady state problems), or rendering the partial differential equations into an approximating system of ordinary differential equations, which are then numerically integrated. Due to the discretization of the closed system the most important areas (or volumes in three dimensions) of the system can have a greater refinement of the mesh, while non-important sections can have a coarser mesh, resulting in more precise solutions with less computational effort comparing this method with any other available.

The FEM software used from henceforth is ANSYS® which for laminate composite structural or dynamic analysis suggest the use of SHELL181, a four-node element with six degrees of freedom at each node, three translations and three rotations, perfect for modelling composite shells, and governed by the Mindlin-Reissner shell theory [49]. For the arms' simulation the BEAM188, a cubic two-node beam element (in 3-D), with six degrees of freedom, and based on the Timoshenko [50] beam theory which includes shear-deformation effects, is suitable for analysing slender to moderately thick beam structures such as the ALIV3's arms. Finally a multipoint constraint element, to apply kinematic constraints between nodes is necessary, to simulate connections and to apply forces and moments in a point that does not belong to a structure, and yet the effects from that same force or moment are transmitted to the structure. For this role the MPC184 will be used, an element that behaves as a rigid link/beam.

ANSYS® verification and validation

To verify what shall be the dimension of the elements to use in the following analysis, in order to obtain accurate solutions, a rectangular laminated composite plate with a central distributed load is analysed in ANSYS® and the maximum displacement is validated with the Rayleigh-Ritz and Levy analytical methods [51]. The plate is clamped in one edge and simply supported in the other three, and has a $[0_2/90_2/\pm 30^\circ/\pm 45^\circ]_s$ layup. The composite properties as well as theoretical displacement are shown in appendix F. In figure 5.1 an evolution of the relative error of the maximum displacement (USUM), Tsai-Wu failure criteria and von Mises stress for different element edge sizes is represented.

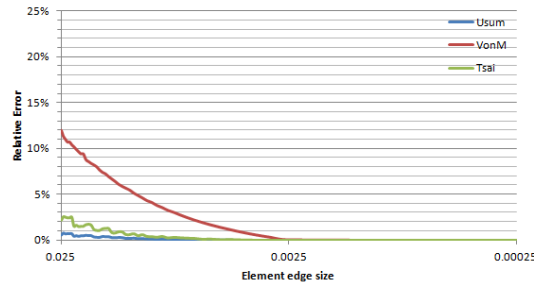


Figure 5.1: ANSYS® convergence

It is conclusive that for an element's edge size of 2.5mm all the maximum displacement, maximum von Mises stress and failure criteria present almost no error at all ($\ll 1$), in relation to an even tighter mesh. The comparison with the analytical results is given in table 5.3.

	ANSYS®	Levy	Rayleigh-Ritz
Maximum displacement [mm]	0.14618	0.14272	0.14244

Table 5.3: Validation of maximum displacement between ANSYS® and the theoretic formulations

ANSYS® presents an error of 2.37% to the Levy method and 2.55% to the Rayleigh-Ritz theory, considerably low, knowing that the theoretic principles do not account for laminae non-planar interactions and so a 2.5mm element edge size is recommended for the following FEM structural analysis.

5.1.3 Laminated composite manufacturing process

To maximise the performance of composite materials, during the cure process an increase in the fibre to resin ratio and removal of all voids is required, and can be achieved by subjecting the material to elevated pressures and temperatures. The best technology to accomplish both requisites is the autoclave, an oven-like structure capable of maintaining high temperatures and pressures during several hours for a perfect cure of the laminate. Many other techniques for composite manufacturing exist being the autoclave the most commonly used in the industry, even to build Formula 1 chassis, however for this project such an advanced technology is not available and the alternative used here is the wet lay-up followed by vacuum bagging.

In the wet lay-up process the epoxy resin is impregnated by hand into the woven fibres and placed in a cast. Then the finished wet laminate is placed inside a vacuum bag. Since true vacuum is very hard to achieve, a compressor is used as a vacuum pump and the part is covered by a slim plastic pierced film and a cotton blanket to reduce drastically the in-bag pressure in order to reduce the excess of resin and prevent voids in the final piece. For the cure process' completion it is necessary to maintain the part in the vacuum bag for approximately six hours. After that the part is ready to any final cutting or material removal process needed for its final completion. The casts are made in extruded polystyrene foam modelled with a computer numerical control (CNC) foam machine, and after the cast in foam is completed, it is cover with duct tape, to prevent the extruded polystyrene from reacting with the epoxy

resin and consequently melt.

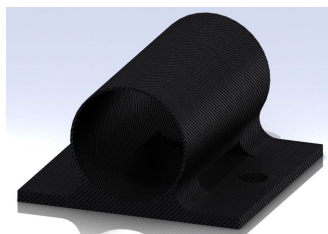
5.2 Structural project

The final design of every component is made based in SolidWorks® and later analysed on an ANSYS® model of the part to be constructed, with a safety factor of 2, which means the Tsai-Wu failure criteria (eq. 5.1) must be inferior to 0.5. The maximum deflection (w_{max}) must be below $5mm$ for integrity and tolerance reasons. The components were envisioned based on the preliminary design assumptions as well as in the dimensions of the off-the-shelf components selected.

5.2.1 Fixed arm

The fixed arm was already decided in the previous chapter to be made of unidimensional carbon fibre tube with a $10mm$ external diameter and $9mm$ of internal diameter, however it is also necessary to attach the motors to the tube and the tube to the main structure, and the best alternative to do so is using a simple embracing plate (figure 2.3(a)). Since this component is merely a junction enabler between the structure, the arm and the motor, a structural analysis is not important. This part consist merely on an hollow cylinder attached to a slim plate, the hollow cylinder is where the arm will enter and the plate is where the connections to motor or central plate will be performed, this connection is simply achieved by the cure process.

The final dimensions of these parts are $12mm$ in height, and $20 \times 20mm$ for the structure connector, while for the motor connector $28 \times 20mm$ is required, due to the motor's diameter. As cast, a $10mm$ diameter foam rod is needed to create the hollow cylinder and a rigid flat surface for the plain connecting area. Three layers of woven fibres (six laminae equal to a $1mm$ thickness) are placed in the flat surface, then the rod cast is placed over them and finally another three layers of woven are placed around the rod and on top of the first layers placed. To expedite the process, and since four of these similar parts are needed, the woven strips should be large enough so that six or more working models can be cut out after cure. The layup used is $[0/90/45/-45/90/0]$ and the projected and real models are shown in figure 5.2.



(a) Projected model



(b) Real model

Figure 5.2: Embracing plate

The embracing plate's connection to the board and motor is done using M3 screws, perpendicularly to the cylindrical shape, with the centre of the holes being $15mm$ apart in the structure connector and

20mm apart in the motor connector. The connection with the arm is glued and fixed by a M3 screw and nut, coming from the centre of the flat surface. The carbon tube needs to be 620mm long, 600mm for the distance between motors, and the other 20mm because the motors are centred in the 20mm embracing plates. The weight of the each part is 3g for the smaller model and 3.5g for the bigger plate.

5.2.2 Swivel arm

Both swivel arm concepts follow the first-servo and second-servo configuration and both alternatives start with a carbon tube connected to the first-servo, stabilized by a bearing at the end of the central area, to take all the transversal loads from the servos. These components are considered to be part of the central area. Both alternatives will use the embracing plate alternative to fix the motor, since the motor in box proved very hard to construct properly, due to poor control in the construction tolerances.

U-arm construction

The U-arm configuration consists of six different components, three of them off-the-shelf, a servo, a motor and a 258mm carbon tube, and three created components, two tube sockets connectors, the arm itself and an embracing plate. The tube sockets were initially envisioned as an acrylic 11mm diameter and height cylinder with an extrude cut of 10mm of both diameter and depth, and an M3 screw opening in the centre of the remaining 1mm thickness face. Then the sockets are glued to the tube and connected to the servo and the arm with the M3 screws and respective nuts. However the CNC available for the manufacturing of such intricate and narrow walls proved inefficient, and a carbon alternative was used instead, but only in the non-servo junction (figure 5.3 (a)). For the servo connections an aluminium hollow tube alternative with a skirt connecting to the servo was also created (figure 5.3 (b)). Enabling a quick assembly and disassembly, this connection uses a 11mm diameter and height tube and two skirts, 180° apart, L-shaped 10mm height and 1mm thickness made from a 25mm aluminium strip bended in 90° angle and connected to each other through the tube by a M3 screw and bolt. The final weight of each socket is 5g and the servo is connected to the arm by four M3 screws and nuts. The aluminium skirt socket is connected to the servo with two small (1.5mm in diameter) screws, whose weight was considered to be part of the servo itself.



(a) Carbon connection



(b) Aluminium skirt connection

Figure 5.3: Tube sockets connectors

Since the selected servo has 20mm of thickness in the head side, the width of the arm must be 30mm. The cast for the arm consists of a 279 × 162 × 100mm parallelepiped with an external quarter

of a 100mm radius circle shape cut in two of the 100mm edges farther apart (5.4). In the middle of the cast, in its upper face, two 10mm in diameter foam rods are inserted, 30mm apart to make a cylinder in the finished piece, to insert the rod from the first-servo. The cast width is 100mm to allow the creation of both arms at the same time and also provide some margin for the cutting of the part.

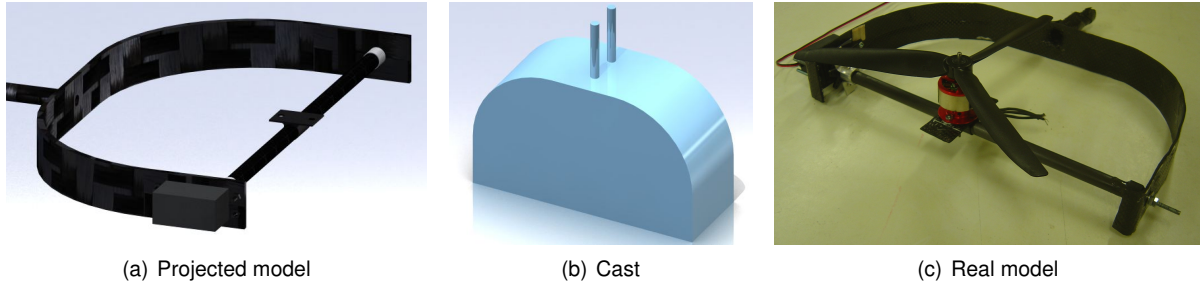


Figure 5.4: U-arm Construction

For the layup it is used a $[0/90/45/-45/90/0]_i$ configuration with i as the thickness in millimetres needed for the arm to respect the structurally sound tolerances required ($SF = 2$ and $w_{max} = 5\text{mm}$). The FEM analysis is made with a 10N force and the maximum torque the servo was estimated to produce, 0.3621N.m (3.69kg.cm), and for the various thicknesses, table 5.4 shows that the best option is $t = 3\text{mm}$. So the exterior dimensions are $285 \times 168 \times 30\text{mm}$ with a curvature of 100mm and a connector for the first-servo tube of 50mm centred in the middle of the arm. The boundary conditions were set in the rod of the first-servo insertion, where all degrees of freedom were restricted. The force and moment of the motor-rotor couple, were applied in its exact position using MPC184 elements.

Thickness (i) [mm]	Tsai-Wu criteria	w_{max} [mm]	Weight [g]
1	15.266	121.8	23.297
2	0.7075	9.168	46.595
3	0.1519	2.761	69.892
4	0.0524	1.233	93.190

Table 5.4: Thickness evaluation for the U-arm

The critical section of the arm is located in the connection with the first-servo (figure 5.5 (b)) as expected, because it is the place where the stress concentrations will be greater. The maximum displacement is located in the arm's non-servo side limit (figure 5.5 (a)).

Finally the embracing plate, where the motor will be placed, is glued and connected with a M3 screw to the tube coming from the second-servo with its centre (where the screw is) located in the intersection of both servo heads' direction. The motor is then fixed with two M3 screws and nuts. Finally the connection with the first-servo rod is also made by an M3 screw for easy replacement and arm switch between U-arm and slim-arm. The total weight of the U-arm is 120g .

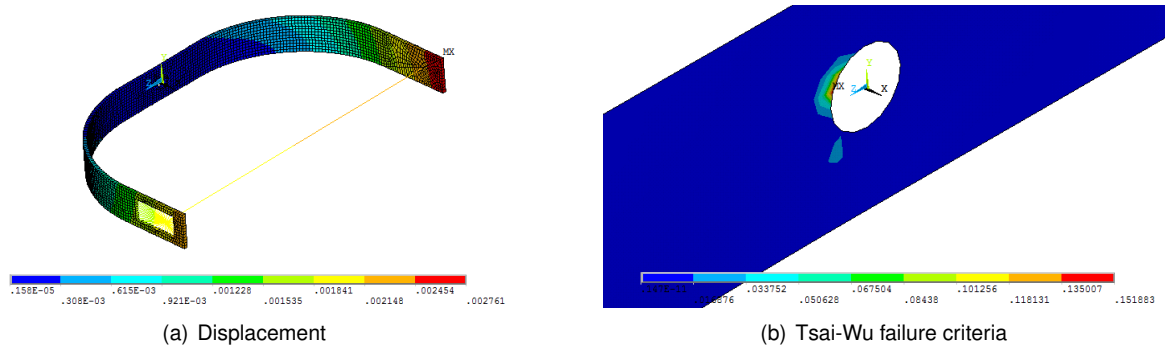


Figure 5.5: U-arm FEM analysis

Slim-arm construction

The slim-arm configuration is simpler than its alternative U-arm configuration and it is constituted by the same motor, rotor, embracing plate and tube socket connectors, however now the motor tube is much smaller ($50mm$) and two new parts are needed, as well as three carbon tubes with $100mm$, $140mm$ and $140mm$ starting the identification from the motor.

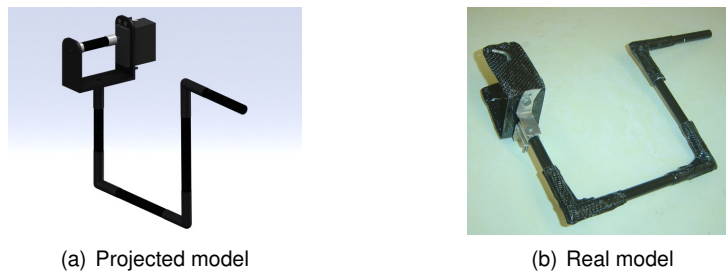


Figure 5.6: Slim-arm construction

The new parts needed are three elbows and a servo support. The elbows are simply a $50 \times 50mm$, 90° L-shaped carbon woven junction for the carbon tubes, made with the same cast as the embracing plate, a foam rod with $10mm$ in diameter, this time cut in a 45° angle and then glued to both cut sections. Both sections must be larger than $50mm$ and a single strip of carbon fibre woven is hand adjusted around the cast, resulting in a final weight of $2g$ for each elbow. For the servo support an analysis similar to the U-arm's arm was conducted, in the motor's position a force of $10N$ and a torque of $0.3621N.m$ was applied to various thicknesses with a $[0/90/45/-45/90/0]_i$ layup (table 5.5) and a $1mm$ thickness proved the best option because it respected all the required tolerances.

Thickness (i) [mm]	Tsai-Wu criteria	w_{max} [mm]	Weight [g]
1	0.0932	1.297	6.882
2	0.0048	0.196	13.765

Table 5.5: Thickness evaluation for the servo support

The cast for the servo support is simply a parallelepiped with $70 \times 60 \times 100mm$ resulting in two parts

with $72 \times 60 \times 30\text{mm}$ after the cut is completed. According to a FEM analysis the maximum displacement occurs above the servo location and the critical area is near the connection with the last tube.

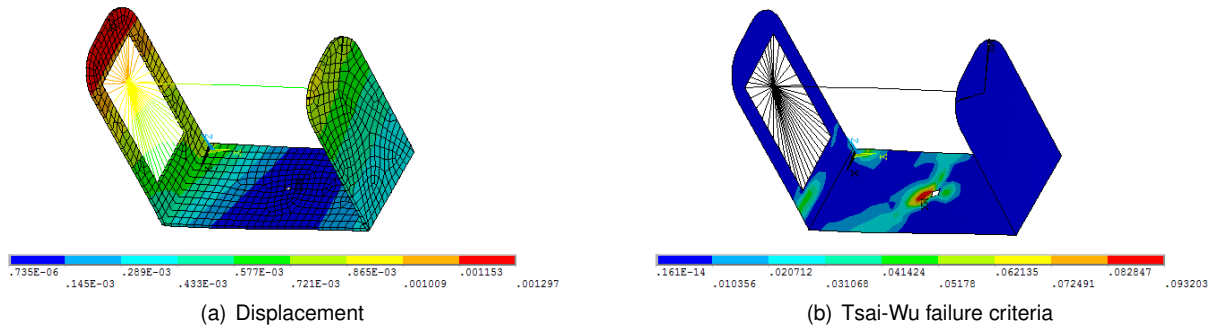


Figure 5.7: Servo support FEM analysis

The connections of the motor and servo are exactly the same as in the U-arm, the elbows are glued to the tubes and the first-servo tube is attached to the first elbow through an M3 screw to allow an easy arm replacement. Finally the servo support is attached with a carbon tube socket connector and an M3 screw at its exact middle in the lower most face. The total weight of the slim-arm is 76g .

5.2.3 Servo board

The servo board is the uppermost component of the central area and it is where the first-servos, the Ardupilot, the magnetometer, GPS and XBee are placed. This board must resist the torsional load of both the first-servos and their weight, as well as the weight from all the other components referred.

In terms of parts' placement, this board is crossed by the fixed arm in the centre of its lowermost section, also where the first-servos must be. In the roof of the board the communication hardware (XBee and GPS) shall be placed, and so does the magnetometer, because the length of the GPS plus the magnetometer, equals roughly the length of the XBee Explorer Regulator (36 to 28.7mm). Finally both Arducopter boards are placed beneath the communication hardware, in the ceiling of the board.

The final dimensions of the servo board are $100 \times 70 \times 45\text{mm}$ with the $70 \times 45\text{mm}$ walls cut out, with the upper face showing a 25mm decrease in each side and a round cut with that same radius in the surrounding faces. Those same faces have cut sections for the insertion of the servo, with the servo supports screwed in the outer wall of the servo board. Finally the lower face is cut to maintain only 20mm near the servo face to allow a connection to the central board. The cast for the construction of this part is a parallelepiped with $120 \times 70 \times 45\text{mm}$. The excess in 20mm (10mm in each side) is to allow a certain degree of error in the layup placement for a later controlled cutting. Both the projected and real models can be seen in figure 5.8, and as described above, the fixed arm crosses the in between servos region, but is not attached to the servo board itself.

The FEM analysis to determine the thickness required (table 5.6) showed that the best option, the one respecting the imposed tolerances was the 1mm alternative, with a $[0/90/45/-45/90/0]$ layup. The boundary conditions were the clamping of all the lower face, in the connection to the central upper board, and the forces and moments from the arm, supported by the servo, were set using MPC184 elements.

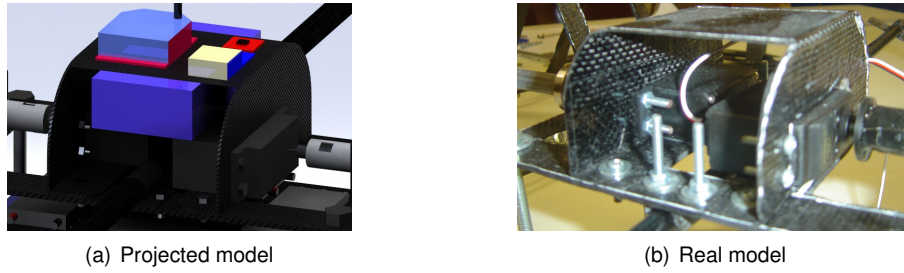


Figure 5.8: Servo board models

Finally the remaining electronic components' weight was set in the upper face. The critical regions are the upper corners of the servo connections, as figure 5.10 (b) suggests, and the maximum displacement is also in this region. Both factors are mainly due to the moment produced by the arm.

Thickness (i) [mm]	Tsai-Wu criteria	w_{max} [mm]	Weight [g]
1	0.0716	0.112	22.543
2	0.0067	0.022	45.087

Table 5.6: Thickness evaluation for the servo board

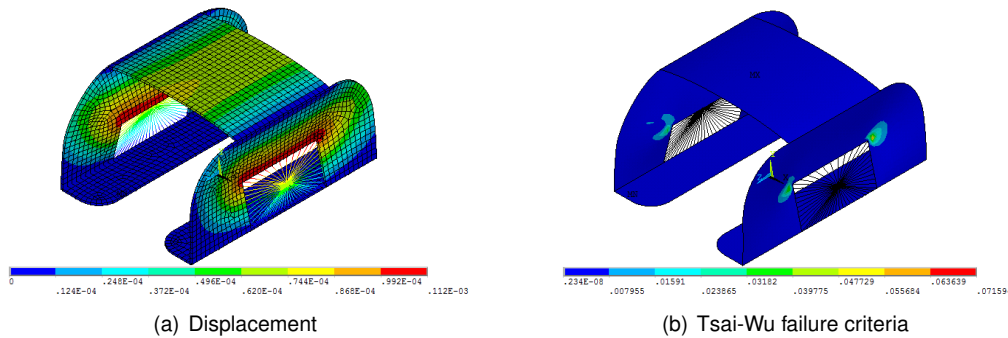


Figure 5.9: Servo board FEM analysis

5.2.4 Electronic board

The electronic board is merely a stand for the placement of the ESC's and to accommodate the battery, and an analysis similar to the ones performed before seems obsolete, however it will be performed nonetheless. The final dimensions of the electronic board are $100 \times 120 \times 30\text{mm}$ and as the servo board the lower face ($100 \times 120\text{mm}$) is cut to maintain 45mm in each side to connect to the lower central plate. The frontal and rear walls ($120 \times 30\text{mm}$) are cut out and the remaining lateral walls ($100 \times 30\text{mm}$) are also cut to allow the placement of the battery, leaving 24mm in each side.

For the FEM analysis the boundary conditions were the clamping of all the lower face, the connection to the lower central board. The weight of the ESC's was placed on the top face. The battery's weight was not considered because it is supported by the lower central board. According to table 5.7, a thickness of

1mm is enough to meet the design requisites, and was the only alternative studied.

Thickness (i) [mm]	Tsai-Wu criteria	w_{max} [mm]	Weight [g]
1	0.00004	0.0221	38.509

Table 5.7: Thickness evaluation for the electronic board

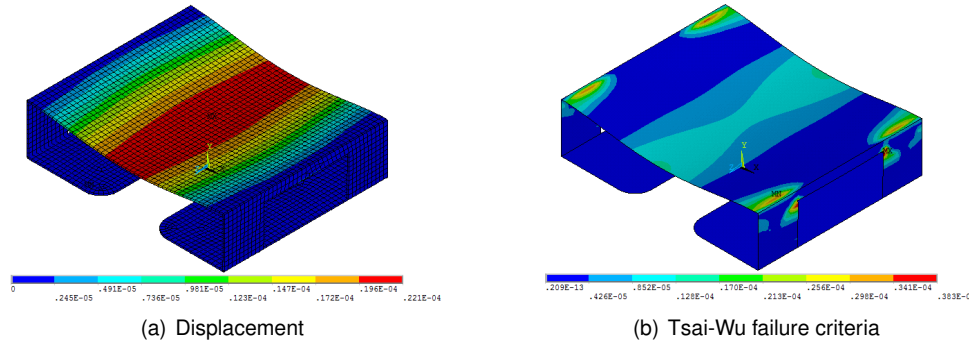


Figure 5.10: Electronic board FEM analysis

The maximum displacement was obtained for the centre of the upper surface, and the Tsai-Wu failure criteria was maximum near the edges of that same section, however, and as expected, the magnitude of the results was negligible.

5.2.5 Central board and remaining central parts

The central section of the ALIV3 is where the heaviest components will be, and where all the structural loads will converge; it must support all the avionics and first-servos weight and withstand the arms' forces and moments, described in all the parts depicted above, finally it must sit on the landing gear in a perfectly steady manner. Its design was based in the one of a building, where all the corners' columns support all the loads, so this central area will consist of two parallel rectangular boards connected by four screws that must hold up all the ALIV3's loads.

The dimension of the boards was decided to be $160 \times 100mm$, the $100mm$ because that was the decided dimension for the fixed arm gap, and the $160mm$ was decided based on the battery size ($146mm$) and the need for a bearing placement for the swivel arm movement. For construction simplification, both boards are constructed simultaneously, and the thickness is decided with a FEM analysis to both boards, regarding the required failure criteria and displacement tolerances.

The boards are also optimized to save weight and all excess boards' area, that do not support any of the avionic components is cut out symmetrically. The first cut is a $60 \times 30mm$ done in the exact centre of the boards to allow the wiring between the ESC's and the Arducopter; a $20mm$ support is maintained on both sides of the central boards for the servo and electronic boards attachments and finally another cut of $60 \times 40mm$ is done on both sides, leaving $15mm$ for the bearing placement. The cast consists of a simple plain and straight $180 \times 240mm$ plate to allow the manufacture of both boards at the same time, followed by a cutting process to finalize their construction.

For the boundary conditions the boards were clamped on the $18mm$ diameter washers used with the column screws and nuts, and the forces and moments applied have all been described previously. For the upper board the servo board and fixed arm reactions are used, while for the lower board the loads consist on the electronic board, battery and landing gear weight. As expected and shown in table 5.8, the biggest loads and displacements occur for the central board and a thickness of $2mm$ is required to respect both the $w_{max} < 5mm$ and Tsai-Wu failure criteria below 0.5 design prerequisites. Since the thickness is $2mm$ the layup used is $[0/90/45/-45/90/0]_S$.

Thickness (i) [mm]	Upper board		Lower board		Weight [g]
	Tsai-Wu criteria	w_{max} [mm]	Tsai-Wu criteria	w_{max} [mm]	
1	1.747	5.669	0.00402	0.228	17.756
2	0.077	0.690	0.00013	0.031	35.512
3	0.015	0.213	0.00003	0.010	53.269

Table 5.8: Thickness evaluation for the central boards

This FEM analysis only regards the upper board, because it was the board with the greater loads applied. From figure 5.11 the greatest displacement is near the centre of the board, in the servo board connection and also in the fixed arm junction. However the critical zone is near the clamping with the washers towards the centre of the plate.

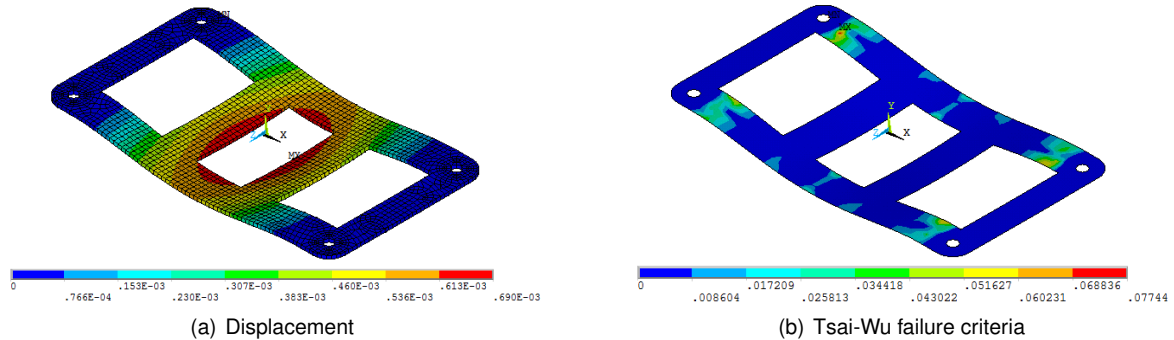


Figure 5.11: Central upper board FEM analysis

For the column screws four stainless steel $80mm$ M6 screws were selected, with nuts and washers in both boards to perfectly clamp the structure. This selection was merely based on market availability, and better alternatives, such as tapping aluminium screws shall be studied in a later iteration of this project, which could lead to a 65.65% decrease in these components weight ($\rho_{Al} = 2700Kg.m^{-3}$, $\rho_{S.S.} = 7860Kg.m^{-3}$). Four screws are needed, each weighting $15g$, an additional eight nuts are required, weighting $2g$ each, finally every one of those contacts with the carbon fibre part requires a washer, to a total of twelve with $2.5g$ each. The total weight of all these components is $106g$.

To attach all the other components M3 screws, nuts and washers are used. 56 screws and nuts are used, however for the servos the washers can only be connected in one side and for that 96 washer are utilized.

From each first-servo comes a 100mm carbon tube to connect the U-arm to the central area, and each of these tubes go through a bearing placed inside two bearing supports. This bearing supports are placed on the edge of the upper board aligned with the first-servos. This part is constructed using a $10 \times 15 \times 40\text{mm}$ acrylic piece and cut on the CNC. The outer diameter of the bearing is 22mm and so two of these pieces are needed for each bearing support. In one of the $40 \times 10\text{mm}$ face a first circular cut with 22mm in diameter is done but just 9mm across and 10.5mm deep, then another circular 10mm in diameter cut is preformed in the hole left by the first cut, this time in the remaining 4.5mm and in just 2mm across. In the $40 \times 15\text{mm}$ face edges a half-circle with 15mm is cut on both sides of the piece. The final part is shown in figure 5.12.



Figure 5.12: Bearing support models

As the figures show, the two pieces in conjunction can restrain the bearing translational movements, allowing the first-servo tube to rotate freely. The attachment to the upper central board is performed with 35mm M3 screws and each one of the four supports weight 5g .

An additional board for the bearings is required, to assure the stabilization of the first-servo tube and with that aim this final central component is created. This component is merely an aid to the bearing supports, and no loads will be applied on it, thus no structural analysis will be performed. The dimensions of this symmetrical board consist on a upper $70 \times 40\text{mm}$ upper sections, followed by a slope of 22.5mm in a 40mm extensions, followed by a 15mm attachment to the bearing supports. This board will have a $[0/90/45/-45/90/0]$ layup with 1mm thickness and the designed and real models are shown in figure 5.13. The cast used must follow the same exact dimensions as described for the part and the part final weight is 9g .

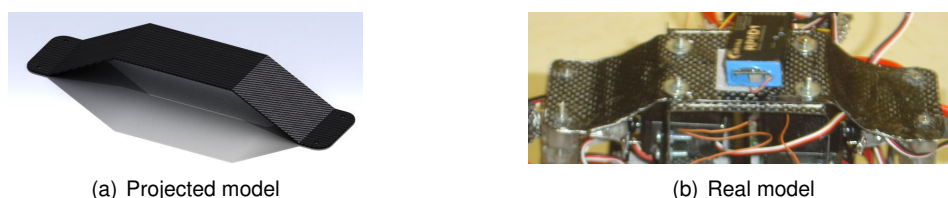


Figure 5.13: Bearing board models

Finally a payload supported was envisioned, however such a support would only be useful for the payload it was designed for, in this case a micro-camera was considered. Such a device was not acquired and as such, the payload support was never constructed, nevertheless its positioning should be below the lower board, in the same holes used for the landing gear site.

5.2.6 Landing gear

The landing gear design must respect the assumptions made in chapter 2 to be the lowermost position, also to prevent any tilting as well as sustain large accelerations on hard landings. It was determined that the landing gear was supposed to have the shape of an inverted V, and from the assumptions and designs of all parts done so far, it was established that the uppermost section of the landing gear will have $40mm$, the width is $20mm$ and the total height is $122.5mm$ to have a $20mm$ margin for a 90° U-arm tilt. The only dimensions left open are the opening angle and the thickness of the landing gear, the first depending on the ALIV3 tilted roll landings and equilibrium studies, and the second coming from a structural FEM analysis, as well as the size of the carbon rod skis coming from tilted pitch landings.

Regarding the ALIV3 pitch angle to define the size of the skis the graphics in figure 5.14 are obtained, both in relation to the centre of mass ($c.g.z = 43.47mm$ above the lower central board, determined using SolidWorks®), while the other c.g. coordinates confirm the ALIV3's symmetry in the xy plane, being located in a projection of the arms' intersection) for the equilibrium analysis, and in relation to the fixed motor positioning to assure that the landing gear is the first component to hit the ground. This initial hypothesis is corroborated by the real measurements executed in the finalized ALIV3 (appendix A) where $c.g.z = 45mm$ (above the lower central board) and both x and y coordinates are exactly in the arm's intersection confirming the ALIV3's symmetry.

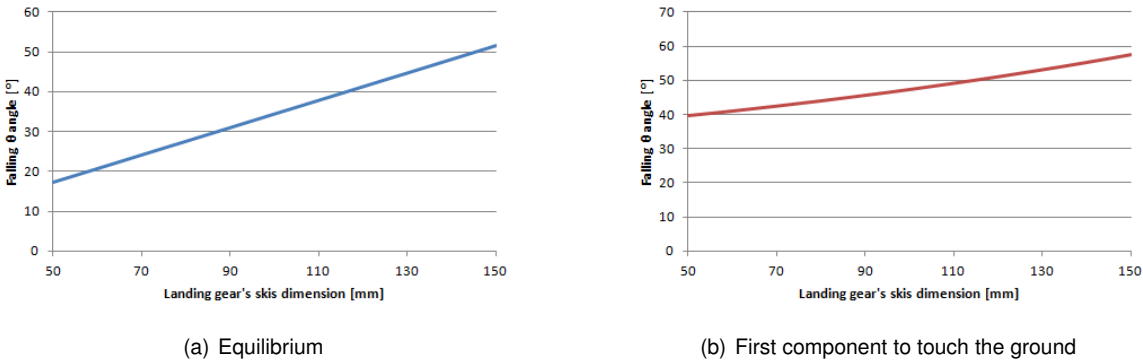


Figure 5.14: Pitch (θ) landing analysis

For the landing gear to be the first component to hit the ground ignoring the skis dimension (figure 5.14 (b)), the falling θ angle must be below 39.56° , however observing (figure 5.14 (a)) is conclusive that the equilibrium is more important, because the landing gear can reach the ground first, but the ALIV3 can pitch and fall. The reasonable angle considered for the construction of the skis, that have been determined to be a $5mm$ in diameter carbon rod, is 30° which lead to an extra $90mm$ on each side of the landing gears legs, to a total of $280mm$ for each ski.

The opening angle is determined with a similar approach as the previous described, this time for the roll (ϕ) angle, and the U-arm is the alternative considered for the analysis, because it is bigger than the slim-arm, and has in a 90° configuration an extra $25mm$ nearer the floor in relation to the slim-arm. Furthermore the slim-arm can be rotated 180° which would force the inversion of the motor, like Pounds *et al.* suggested [22] and thus placing the lowest component of the slim-arm, in this instance the rotor,

much higher than any part of the U-arm.

For the equilibrium analysis (figure 5.15 (a)) and considering again a 30° falling angle, this time with the ALIV3 rolled, a 30° landing gear's angle is the best option and the one decided to be used. In the first component to hit the ground analysis, for an arm neutral position (0°) any landing gear angle prevents a damage to the ALIV3 in a landing roll angle below 30°. For the decided 30° landing gear angle, and with an arm angle of 60°, a 13.65° ALIV3's roll angle is allowed.

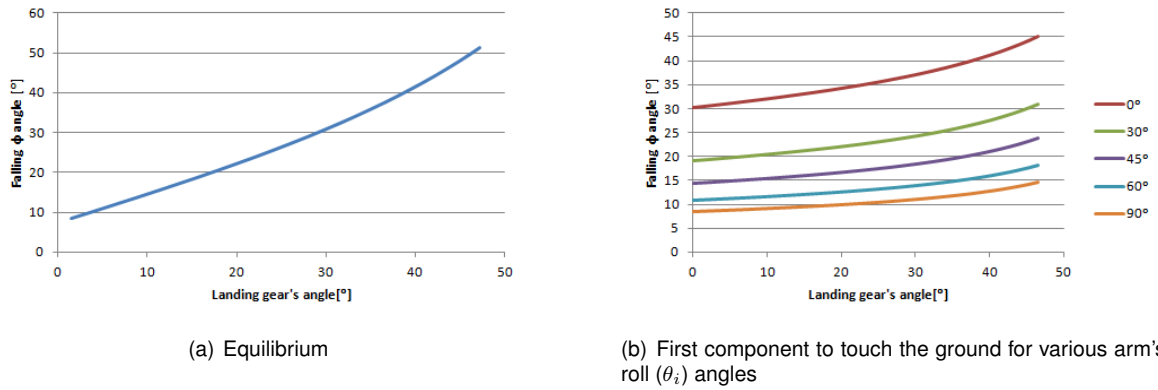


Figure 5.15: Roll (ϕ) landing analysis

The final dimension of the landing gear to be determined is its thickness. And is determined again by a FEM analysis, however this time the study must account for hard landings and a factor representing the acceleration increase, commonly known as \bar{G} must be multiplied to the total weight of the ALIV3 (1.6kg), and the final the landing thickness gear must withstand. The boundary conditions will be simply supported in the landing gear's legs edge but free to move away from each other, and the 16N are applied in the 40mm upper straight section.

By definition of the conservation of momentum [52], the \bar{G} factor is defined as $\bar{G} = \frac{\Delta V}{g\Delta t}$ and simplifying using the equations of motion, for no drag and no initial velocity:

$$\bar{G} = \frac{\sqrt{2h}}{\sqrt{g}\Delta t} \quad (5.2)$$

with h as the initial altitude of the ALIV3, and Δt the time of impact, that according to Fuchs and Jackson [53] can be considered 0.15s. So for a 25m free fall, a reasonably high climb and neglecting the drag effect, the total G will be 15.051. Before construction is necessary to determine the cast used. The cast consists on a 120 × 170 × 80mm, with a 30° cut in both sides of the 120 × 170mm section. In the edge of this cut, where it intersects the 120 × 80mm lower face, two foam 5mm rods are placed to create the skis attachment. Finally the 80mm follow the same rule as the arm's did, to create both legs at the same time and cut out the excess without worries.

Considering this factor and a total weight applied of 8N, because the landing gear is composed of two legs, and just one is analysed, because all loads and stress are symmetric. Table 5.9 is obtain to show the evolution of the design requisites with the thickness and becomes explicit that the best option is to create the landing gear with a three millimetre [0/90/45/-45/90/0]₃ layup.

Thickness (i) [mm]	Tsai-Wu criteria	w_{max} [mm]	Weight [g]
1	26.881	92.76	10.264
2	0.9607	9.483	20.528
3	0.1729	2.759	30.792
4	0.0529	1.162	41.055

Table 5.9: Thickness evaluation for the landing gear

The total weight of the landing gear, consisting of two legs and two skis will be 77g and the critical section, according to the FEM analysis described in figure 5.16 is in the connection to the lower central board, while the maximum displacement occur in the legs edge, the point of contact with the ground.

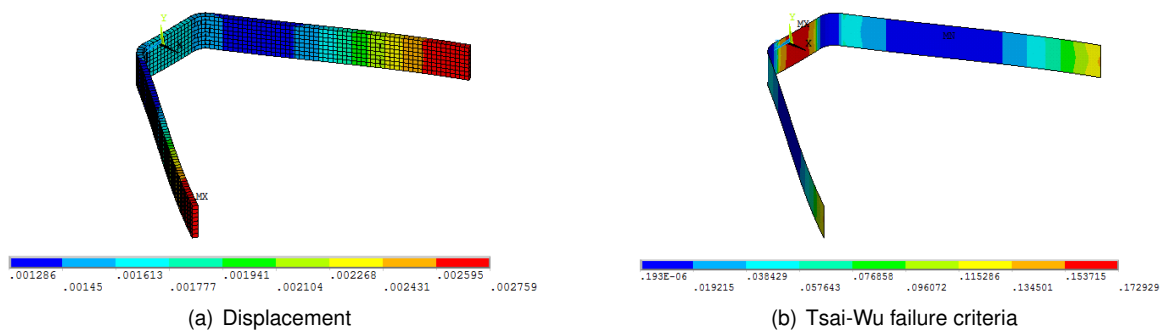


Figure 5.16: Landing gear FEM analysis

5.3 Final design

All parts are now fully designed and constructed, and the only difference between the models are their swivel arms, the remaining components is the same, and both models cannot exist at the same time, the swivel arms must be replaced to use each one of the alternative ALIV3 configurations.

In terms of weight the U-arm alternative theoretically weights 1788.33g, which is 11.77% above the initial weight estimation of 1600g, however the real model only weights 1749g, that reduces the error in relation to 9.31%. The source of this 2.25% difference between theory and reality comes from the laminate construction process, in which the quantity of epoxy resin used was in reality slightly inferior to the quantity studied. If the components were made in an autoclave, this could have been averted, although the possibility of this proportion misshapen was accounted for in the design process with a $SF = 2$ and so no component constitutes a risk for any of the ALIV3 operations. The only effects of this small alteration in resin to fibre proportions result in a *de facto* larger rigidity and a minor Tsai-Wu failure criteria than the projected models, and of course lower weight.

For the slim-arm model the theoretical weight was 1690.34g with an error of 5.65% regarding the initially estimated weight of 1600g. The real model like for the U-arm model and for exactly the same reason presented a total weight of 1660g, 3.74% above the estimation.

This increase in weight regarding the initial estimation is a result of both the quantity of screws, nuts and washers used, especially the M6 ones used for the central boards, as well as the amount of cabling needed to connect the motors to the ESCs, and the weight of the battery. All combined these components weight $658.2g$, or 37.63% considering the U-arm alternative, and so in future versions of the project, aluminium screws, nuts and washers as well as lighter cabling or even a lighter battery, at the expense of endurance, shall be evaluated to reduce weight, nevertheless the current total weights of both version are within the design objectives. Representations of the designed U-arm and slim-arm ALIV3 models and the really constructed U-arm alternative are shown in figure 5.17, and the detailed ALIV3 weight is presented in appendix G.

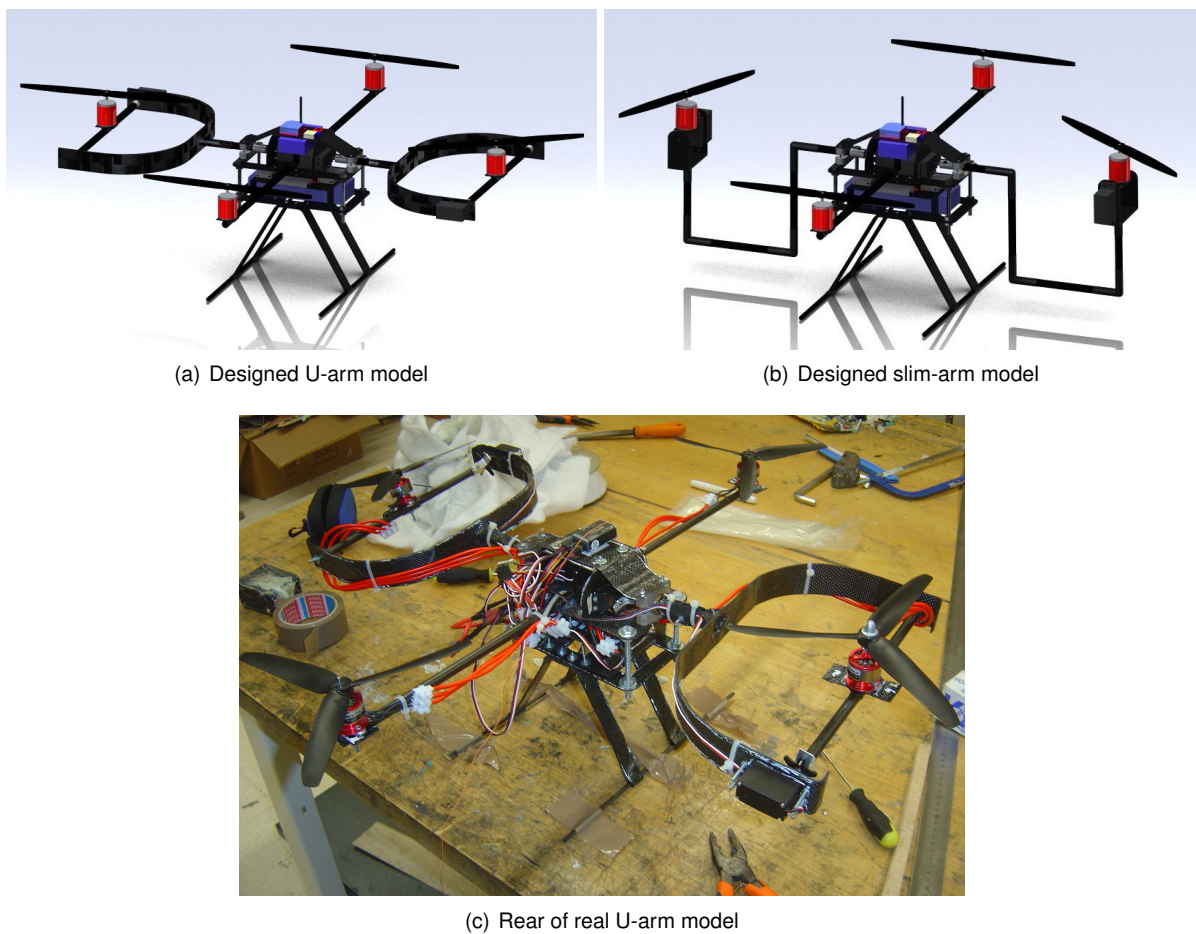


Figure 5.17: ALIV3 final models

The final U-arm model dimensions excluding the rotors, are $620 \times 642 \times 245mm$, for the fixed arm, swivel arm, and total height respectively, or x, y and z -axis of the ABC frame. In the slim-arm model each swivel arm has less $2mm$ resulting in the final dimensions of $620 \times 638 \times 245mm$. Nonetheless the distance between opposite rotors is $600mm$ and each one is 90° apart considering the centre of mass position.

In terms of execution the designed parts proved very tough, and the requests of project were completed in the preliminary operational tests. Real operational tests shall only be conducted when a working control model for the ALIV3 is completed in a future iteration of the project. The current ALIV3 has

undergone very limited testing, fixed to a table with duct tape, nevertheless in one test, mounted with rotors 5, and inferior motors to the ones selected, with all motors working at theoretically the same power, less than half the motor capacity, the duct tape peel off the table and the ALIV3 pitched over the table to a $1.2m$ fall. Inferior rotors and motor were used because the optimum rotor could not have yet been really prototyped, and the selected motors are not yet available.

This accident proves three important aspects of the ALIV3 construction and operability. Firstly it has the power to easily lift itself, with a large margin for the rotor tilting, because if less than half the motor capacity was being used, with inferior components than the ones selected, means that the ALIV3 can be lifted with just two motors. Secondly all parts that were designed to withstand only the weight of the ALIV3, sustained a larger acceleration in collision than the acceleration of a soft regular landing, furthermore the landing was done in an upside-down position with the servo board hitting the floor, instead of the landing gear. Using equation 5.2 this fall \bar{G} 's were equal to 3.30 and so the structure is even sounder than expected. Thirdly the battery, PDB and ESCs connection is working perfectly. It is important to note that the tests were performed with an RC connection, because there was no viable control platform available and no need to use the Ardupilot.

Chapter 6

Performance

This chapter is dedicated to the determination of what ALIV3 arm alternative is the best in terms of aerodynamics, and if the models should be covered, or remain as they are, with all components facing the airflow. The lateral aerodynamics are also evaluated to determine if the forward and lateral motion options were the correct ones or if its preferable to chance those concepts. The forward, lateral and climb motions analysis refer to the x,y and z -axis from the ABC frame respectively. The servo's maximum torque is also tested to determine the maximum rotor's lift for which they will still work properly. Finally flight performances are conducted both for climbing and forward motion.

The cover consists of a 360° revolved ellipse centred $40.5mm$ above the central lower board with the x and y coordinates both zero in the ABC frame (which is centred in the ALIV3's c.g.). The semi-major axis is parallel to the xy plane and equal to $125mm$ while the semi-minor axis, parallel to z is $62.5mm$ long. The cover is to be constructed (if proved useful) in thermoplastic and have a maximum thickness of $1mm$ to save weight, since the objective of its creation is to reduce drag and not increase the total weight more than 5%. The cover is fixed on the bearing supports and the servo board, and is cut in identical halves for easier assembly and disassembly. The upper half must be cut in the crossings of every arm while the lower half must allow the intersection of the landing gear.

6.1 Drag Analysis

For the drag estimation a simplification of both models, covered and uncovered (figure 6.1) is created in SolidWorks[®], and analysed in the Computational Fluid Dynamics (CFD) platform of that same software, Flow Simulation. SolidWorks[®] Flow Simulation solves time-dependent Navier-Stokes equations with the Finite Volume Method (FVM) on a rectangular (parallelepiped) computational mesh.

The first step in the FVM is to divide the domain into a number of control volumes followed by the integration of the differential form of the governing equations over each control volume. Interpolation profiles are then assumed in order to describe the variation of the concerned variable between cell centroids. The resulting equation is called the discretization equation, that expresses the conservation principle for the variable inside the control volume; in this case the total resulting forces. One of the major

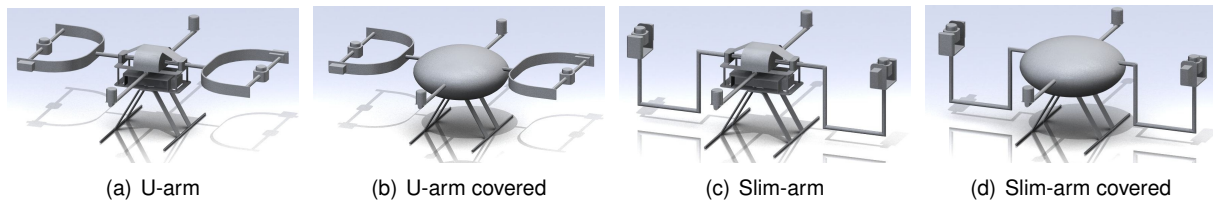


Figure 6.1: ALIV3 simplifications

advantages of the FVM is that the obtained solution satisfies all conservation laws (mass, momentum, energy and species) for each control volume as well as for the whole computational domain, resulting in the advantage that even a coarse grid solution exhibits exact integral balances, yet larger errors than a refined mesh [54].

6.1.1 SolidWorks® CFD analysis verification and validation

To confirm the accuracy of the solutions of the simplified ALIV3s using this method, a cylinder is analysed and the results for the drag coefficient (C_D) are compared with the analytical results, provided by Brederode [30], which suggests that for an infinite cylinder the C_D is 1.2, in laminar flow. Performing the CFD analysis to a small tube (to assure laminar flow in all the domain) the force results are obtained, and using equation 3.14(b) the C_D error is validated in accordance with Berderode's theoretical value. To verify the solution several elements' resolution factors are used and shown in figure 6.2.

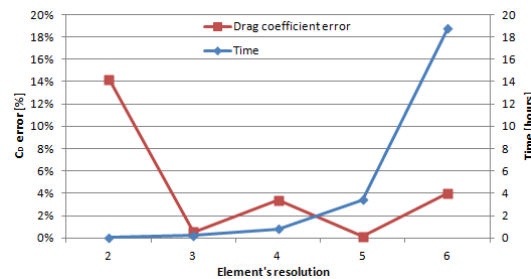


Figure 6.2: SolidWorks® validation and verification

For these results a velocity of $10ms^{-1}$ was used in a standard sea level ISA atmosphere. Good results are just as important as reduced computational time and so an element's resolution factor of 5, that presented an error of 0.15% is selected to be used in the following analysis. Neglecting the 3 resolution factor result, that does not follow the normal convergence tendency, a resolution factor of 5 is the last good solution before a crucial finite element characteristic becomes visible; when the elements used are very small the solution diverges, and the 6 resolution factor illustrates that same notion.

6.1.2 Flight drag analysis

Since the available software proved to be a reliable source for aerodynamic analysis, the four models from figure 6.1 are analysed in a standard sea level ISA atmosphere with a velocity of $10ms^{-1}$ and the results for the drag (in Newtons) are shown in table 6.1.

	 U-arm	 U-arm covered	 Slim-arm	 Slim-arm covered
Forward Flight	1.304 <i>N</i>	1.092 <i>N</i>	1.384 <i>N</i>	1.380 <i>N</i>
Lateral Motion	1.399 <i>N</i>	1.714 <i>N</i>	1.286 <i>N</i>	1.584 <i>N</i>
Climbing	1.596 <i>N</i>	2.376 <i>N</i>	1.313 <i>N</i>	2.436 <i>N</i>

Table 6.1: Drag analysis

One major flaw of this cover is automatically noticeable from these results. The cover was designed to optimize the forward flight, because that is the direction of major importance, and supposedly the most commonly used in flight, and the results illustrate that, at least for the U-arm model. However for lateral motion or for climbing the drag is heavily increased, to a maximum of 89% in the slim-arm climb motion, rendering the present hypotheses of covering the ALIV3 obsolete, even if it has decreased the drag 16.3% for the U-arm alternative in forward flight, the remaining results are very inconvenient, and considering the addition of the weight increase, the final ALIV3 is decided to be uncovered.

Regarding which arm alternative is the best, the slim-arm has an advantage of 8.08% in lateral motions and 17.72% when climbing, however the most important motion is forward flight, in which the U-arm alternative has a 6.14% advantage, that in conjunction with the accentuated asymmetry of the slim-arm leads to the suggestion that the U-arm alternative is the more suited option for a final model. If possible it would be interesting to verify these results with wind tunnel testing of the real ALIV3 models, to corroborate this selection. Also for the U-arm forward direction was accurately selected, with 6.79% less drag than the lateral motion.

6.2 Servo testing

To assure that the servo selection was accurate, both arm alternatives are connected (in turn) to the first-servo and tested with increasing loads to see what is the maximum weight for which they can still tilt efficiently, without damaging themselves or the arm structure. Before testing the real models and to avoid damaging any component, an analysis similar to the one in section 4.2 is conducted, where the maximum servo torque necessary was found, this time to determine the maximum lift the rotor can produce without interfering in the servo performance. A maximum torque of 4.1*Kg.cm* is used, and the results for the first-servo show that the maximum weight to be tested shall not be greater than 989.48*g* for the U-arm model, and 918.35*g* for the slim-arm alternative, bearing in mind that these results are obtained with the selected motor at maximum rotation, and in the test executed the motor was stopped. These values shall never be surpassed in real testing. The values of maximum weight for the second-servo are not considered because in both arm alternatives that value is greater then the first-servo maximums presented above.

For the test, a water bottle is attached to the motor's embracing plate, and the observable qualitative results are shown in table 6.2 as fractions of the normal tilting speed, or in total maximum angle possible (normal tilting angle available is 360°).

Tested weight	Second servo	First servo	
		U-arm	Slim-arm
500g	1	1	1
700g	1	1	3/4
900g	1	3/4 and 60°	1/2 and 40°
980g	3/4	1/2 and 40°	Not tested

Table 6.2: Servo testing

It is noticeable that both arm alternatives are capable of providing a 20% thrust margin (500g), considering hover without any alteration to the arm functionality, and that, as expected, the slim-arm falters for a lower testing weight than the U-arm, confirming that that U-arm alternative is a better option both in terms of aerodynamics and tilting of the arm performance. Still for both models the first-servos start to show some disabilities well before the maximums expected, and this is due to the servo's sockets used, with the aluminium skirt connection allowing an unexpected minimal rotation along that same skirt connection axis. This can easily be averted by connecting two more strips 90° apart from the already existing two (to a total of four), cancelling the new found rotation coming from heavy loads, in the U-arm case, more than two times the force needed for hovering. In this point of the project that is not a mandatory correction and the ALIV3 will remain as it is.

6.3 Flight performance

An estimate of the forward flight and climbing performances is executed to determine if the project meets its predetermined requisites. Resorting to Leishman [20] the power required for climbing (P_c) is a function of the climb velocity (V_c) and is given by:

$$P_c = P_h \left(\frac{V_c}{2v_h} + \sqrt{\left(\frac{V_c}{2v_h}\right)^2 + 1} \right) \quad (6.1)$$

with P_h and the power required for hovering coming from figure 6.3(a) where $V = 0$, and $v_h = \sqrt{a_w T / (\rho A)}$ being the rotor's induced hovering velocity. That same graphic is obtained from the definition of the power required for any helicopter flight, which is given by:

$$P = \sum P_i + \sum P_0 + P_P \quad (6.2)$$

where $\sum P_i$ is the induced power and $\sum P_0$ is the profile power, for every motor. P_P is the parasitic power from the ALIV3's shape. The parasitic power is given by $P_P = DV = \frac{1}{2}\rho S_{model} V^3 C_D$, while the

other factors differ from tilting rotors to fixed ones, because the ALIV3 central core remains in a steady position in all its operations, being the motor-rotor couple what really rotates, and has an angle of attack (α) in relation to the moving flow equal to the arm rolling angle (θ_i). The fixed rotors α is the same as the ALIV3 central core and thus is always zero. For the tilted rotors, the equilibrium equations are:

$$T \cos \alpha = \frac{W}{4} \quad (6.3a)$$

$$T \sin \alpha = \frac{D}{2} \quad (6.3b)$$

$$\Rightarrow \alpha = \arctan \frac{2D}{W} \quad (6.3c)$$

while for the fixed rotors $T = W/4$. The induced power is given by $P_i = kTv_i$, with the rotor's induced velocity (v_i) according to Jackson [55], given by the following expression, that must be solved numerically:

$$v_i^4 + 2V \sin \alpha v_i^3 + V^2 v_i^2 = v_h^4 \quad (6.4)$$

The profile power is calculated with $P_0 = \rho A (\Omega R)^3 C_{P_0}$, with $\Omega = \sqrt{\frac{T}{1/2 \rho A C_T R^2}}$ and the profile power coefficient is:

$$C_{P_0} = \frac{\bar{\sigma} C_{d_0}}{8} \left[1 + K \left(\frac{V \cos \alpha}{\Omega R} \right)^2 \right] \quad (6.5)$$

the empirical constant K is set at 4.7 according to Leishman [20], while the constant k and the blade drag coefficient C_{d_0} are obtained using the C_P equations for hovering:

$$C_P = C_{P_i} + C_{P_0} = \frac{k C_T^{3/2}}{\sqrt{4 a_w}} + \frac{\bar{\sigma} C_{d_0}}{8} \quad (6.6)$$

This expression is an approximation where the blade drag is considered constant along all the blade, which is not accurate, but can be used as a first approximation. Although the results cannot be considered as an exact match to the real situation, they can be used as a comparison between arm alternatives and to confirm if the order of magnitude of the climb and forward power is acceptable. The variables required for the total power calculations are:

C_{P_i}	=	0.0018	C_P	=	0.0022	C_T	=	0.0167	$\bar{\sigma}$	=	0.1396
S_U	=	$0.02201 m^2$	S_{slim}	=	$0.02571 m^2$	A	=	$0.061 m^2$	R	=	$0.139 m$
ρ	=	$1.225 Kg.m^{-3}$	a_w	=	0.61	W_U	=	$17.158 N$	W_{slim}	=	$16.285 N$
C_{D_U}	=	0.967	$C_{D_{slim}}$	=	0.879	k	=	1.3177	C_{d_0}	=	0.0224

All these in conjunction with equation 6.2 result in figure 6.3 where the total power consumed is shown as a function of the respective velocities considered, forward (a) or climbing (b).

The maximum power ceiling illustrated in both figures as 1110W is a direct result from the battery used, that has 11.1V and a maximum current of 100A. The project maximum velocities can be easily achieved with just a fraction of the total power available. The real maximum climb velocity is $21.1 m.s^{-1}$, well above the $5 m.s^{-1}$ the project required, and for the U-arm forward flight $29.4 m.s^{-1}$, instead of $10 m.s^{-1}$. Since these values have some approximations in their genesis, real testing, when a

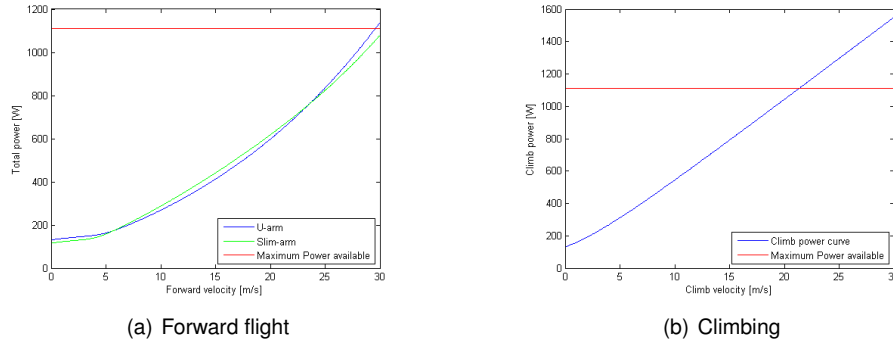


Figure 6.3: ALIV3's required total power

working control for the ALIV3 is completed, should be conducted to confirm the veracity of the results.

In terms of the arm alternatives, as expected (from the drag analysis) for $10m.s^{-1}$ the U-arm model has a better performance, whereas below $5.723m.s^{-1}$ and above $23.491m.s^{-1}$ the slim-arm alternative consumes less power. Although having a greater drag, the slim-arm model is 5.09% lighter than the U-arm and for that reason it has a lower induced and profile power, because it needs to lift less weight and so the rotor can spin slower. For velocities above $5.723m.s^{-1}$ the parasitic power, proportional to the drag, penalizes the slim-arm, and the U-arm is a better option. For very high velocities, well above this project requisites, greater rotor angular velocities are needed which leads to the increase of the induced velocity proportional to the model's weight, and thus the slim-arm becomes again the more economic alternative, as figure 6.4 demonstrates.

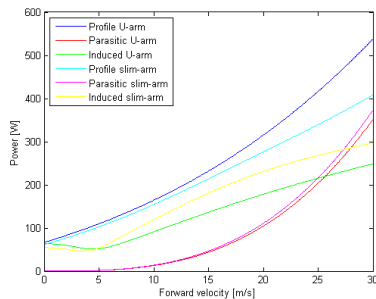


Figure 6.4: Power divisions for both alternatives

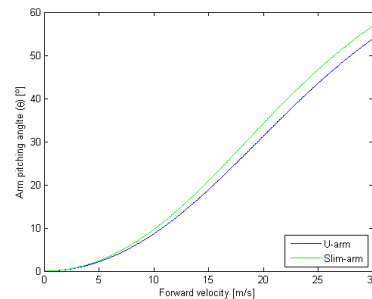


Figure 6.5: First-servo roll angle θ for forward flight

As a final curiosity, figure 6.5 shows the evolution of the roll angle of the arm, created by the first-servo, to achieve a desired forward flight velocity. Since the U-arm model is heavier, the thrust needs to be greater than for the slim-arm alternative, and because of that, its curve is below the slim-arm's.

For all the reasons stated in this chapter the U-arm presents itself as the best alternative, although having a greater weight. It is not so asymmetrical as the slim-arm what will compromise the controllability of the ALIV3, and thus the U-arm alternative is easier to control. The U-arm alternative also has the advantages of a better first-servo performance and better performances at medium flight speeds (above $5.723m.s^{-1}$) and so it is the alternative suggested for future iterations of the ALIV3 project.

Chapter 7

Conclusions

The major achievement of the present work was the construction, for a future control system development, of a quadrotor platform with multiple degrees of freedom, the ALIV3, theoretically capable of moving in all six degrees of freedom maintaining its central core perfectly levelled due to the rotation of two opposed rotors in two directions other than their rotation, and thus having the advantage of drag reduction in comparison with standard quadrotors, because in all translations the surface facing the airflow is independent of its velocity, and can be maximized to reduce forward drag, while for standard quadrotors, its velocity is proportional to a roll or pitch angle of all the quadrotor. This theoretical movement capacity was also fully determined with all translations and transient rebalancing operations fully described for a perfect future control software for the ALIV3's flight operations.

The aim of this project was to design and construct the innovative concept of a quadrotor with two tilting rotors, the ALIV3, with the technical capacity available, and so all the necessary parts were built with an high tenacity carbon fibre laminated composite, with a safety factor of 2 in accordance with the Tsai-Wu failure criteria and a maximum deflection of $5mm$ for every part individually, and all final parts respected this criteria.

A genetic algorithm with the blade element momentum theory was used to create an optimum rotor for the ALIV3's hovering scenario. All the necessary variables for a rapid prototyping process of a real model were determined as well as the rotor's ideal aerofoil. In terms of the off-the-shelf components, several market alternatives for avionics, motors, servos and simple structural components were evaluated and selected according to existent quadrotors, need of the project and price.

Two final models were developed, yet they only differed in the swivel arm's format, and so only one central area and landing gear were created, while two of each arm models were constructed, the U-arm and the slim-arm. The U-arm is the symmetrical U-shaped, stronger swivel arm alternative, while the slim-arm in the lighter and more simply constructed version constructed with three small carbon tubes and connecting elbows. However after construction and testing of both alternatives, the U-arm proved to be the best option for the ALIV3.

The final dimensions of the ALIV3 in the U-arm configuration are $620 \times 642 \times 245mm$ with $600mm$ between opposed rotors and a final total weight of $1749g$.

7.1 Future Work

In a future continuation of this project a revision of the total weight could be important but not mandatory, and so was proved by the small testing accident. Nevertheless the central stainless steel material could be replaced by aluminium to decrease 65.65% of weight in those components alone. In terms of the remaining components an optimization with reduction of material could also be studied, especially in the arm and landing gear. The skirt tube connectors could also be improved in case of necessity, adding two more strips, 90° from the existent ones.

The cover studied in this work was not optimized for any other direction than forward flight, and provided good results, however for the other direction the results were penalized and the cover hypothesis is for that reason eliminated. It would be interesting, as an optimization process to design a cover that would increase the performances in all directions, not just forward flight.

All these aspects are purely accessory, and would only improve the endurance of the ALIV3, the crucial aspect of a continuation of this project is the ALIV3's control implementation, because without it, an aircraft such as this cannot fly, and that is the the most important factor in all aircraft projects.

Finally, and after a true control platform is fully functional, the transition of the ALIV3 to a UAV would be the final iteration of this project.

Bibliography

- [1] J. Gordon Leishman. The bréguet-richet quad-rotor helicopter of 1907. www.enaе.umd.edu/AGRC/Aero/Breguet.pdf, May 2002.
- [2] University of Maryland. The gamera project, 2011.
- [3] Oemichen 1922. http://aviastar.org/helicopters_eng/oemichen.php, February 2011.
- [4] De bothezat 1922. http://aviastar.org/helicopters_eng/bothezat.php, February 2011.
- [5] Markman G. Holder, Steve G. Holder, and William G. Holder. *Straight Up: A History of Vertical Flight*. Schiffer military/aviation history, 2000.
- [6] C.Gablehouse. Helicopters and autogiros, 1969.
- [7] Beating gravity - curtiss-wright x-19a. http://www.unrealaircraft.com/gravity/cw_x19a.php, February 2011.
- [8] Ilan Kroo, Fritz Prinz, Michael Shantz, Peter Kunz, Gary Fay, Shelley Cheng, Tibor Fabian, and Chad Partridge. The mesicopter: A miniature rotorcraft concept - phase 2 interim report. Stanford University, July 2000.
- [9] Haomiao Huang, Gabriel M. Hoffmann, Steven L. Waslander, and Claire J. Tomlin. Aerodynamics and control of autonomous quadrotor helicopters in aggressive maneuvering. In *Proc. of the IEEE International Conference on Robotics and Automation Guidance, Navigation, and Control Conference*, 2009.
- [10] Jorge Miguel Brito Domingues. Quadrotor prototipe. Master's thesis, Instituto Superior Técnico, 2009.
- [11] Bernardo Sousa Machado Henriques. Estimation and control of a quadrotor attitude. Master's thesis, Instituto Superior Técnico, 2011.
- [12] Beating gravity - curtiss-wright x-19a. http://www.uavision.com/index.php?option=com_content&view=article&id=56&Itemid=37&lang=en, February 2011.
- [13] Draganflyer x4 helicopter tech specs. <http://www.draganfly.com/uav-helicopter/draganflyer-x4/specifications/>, October 2010.

- [14] Parrot ar.drone. <http://ardrone.parrot.com/parrot-ar-drone/usa/>, February 2011.
- [15] Arduino-based autopilot for multicopter craft, from quadcopters to traditional helis. <http://code.google.com/p/arducopter/wiki/ArduCopter>, February 2011.
- [16] Frank Colucci. The mono tiltrotor. *Vertiflite*, 57(2):20–23, Summer 2011.
- [17] Wind tunnel testing completed on bell boeing quad tiltrotor. <http://www.helis.com/news/2006/quad-windtunnel.htm>, September 2006.
- [18] Filipe M. S. Pedro. Projecto preliminar de um quadrirotor. Master's thesis, Instituto Superior Técnico, 2009.
- [19] Severino M. O. Raposo. System and process of vector propulsion with independent control of three translation and three rotation axis. *Intellectual Property*, 2010.
- [20] J. Gordon Leishman. *Principles of Helicopter Aerodynamics*. Cambridge University Press, 2000.
- [21] Warren R. Young. *The Helicopters*. "The Epic of Flight". Chicago: Time-Life Books, 1982.
- [22] Paul Pounds, Robert Mahony, Joel Gresham, Peter Corke, and Jonathan Roberts. Towards dynamically-favourable quad-rotor aerial robots. Canberra, Australia, 2004. In Proc. of Australasian Conference on Robotics and Automation.
- [23] Sérgio Eduardo Aurélio Pereira da Costa. Controlo e simulação de um quadrirotor convencional. Master's thesis, Instituto Superior Técnico, 2008.
- [24] Bernard Etkin and Lloyd Duff Reid. *Dynamics of Flight - Stability and Control*. John Wiley and Sons, 1996.
- [25] Aeroquad parts list. <http://aeroquad.com/content.php?114>, April 2011.
- [26] Gabriel M. Hoffmann, Haomiao Huang, Steven L. Waslander, and Claire J. Tomlin. Quadrotor helicopter flight dynamics and control: Theory and experiment. In *Proc. of the AIAA Guidance, Navigation, and Control Conference*, 2007.
- [27] M. Drela. Xfoil: An analysis and design system for low reynolds number airfoils. In *Conference on Low Reynolds Number Airfoil Aerodynamics*. University of Notre Dame, June 1989.
- [28] J. L. Hess and A. M. O. Smith. *Calculation of Potential Flow About Arbitrary Bodies*. Progress in Aeronautics Sciences 8, 1967.
- [29] Mark Drela and Michael B. Giles. Viscous-inviscid analysis of transonic and low reynolds number airfoils. *Aiaa Journal*, 25:1347–1355, 1987.
- [30] Vasco de Brederode. *Fundamentos de Aerodinâmica Incompressível*. IDMEC, Instituto Superior Técnico, 1997.

- [31] E. V. Laitone. Wind tunnel tests of wings at reynolds numbers below 70 000. *Experiments in Fluids* 23, pages 405–409, 1997.
- [32] H. B. Squire, R. A. Fail, and R. C. W. Eyre. Wind-tunnel test on a 12-ft diameter helicopter rotor. *Ministry of Supply, Reports and Memoranda* 2695, 1949.
- [33] J. R. Meyer and G. Falabella. An investigation of the experiment aerodynamic loading on a model helicopter rotor blade. *NACA, Technical note* 2953, May 1953.
- [34] J. H. Holland. Adaptation in natural and artificial systems. *University of Michigan Press*, 1975.
- [35] Kenneth Alan De Jong. *An analysis of the behavior of a class of genetic adaptive systems*. PhD thesis, 1975.
- [36] Alden H. Wright. Genetic algorithms for real parameter optimization. In *Foundations of Genetic Algorithms*, pages 205–218. Morgan Kaufmann, 1991.
- [37] Uic airfoil coordinates database. http://www.ae.illinois.edu/m-selig/ads/coord_database.html, July 2011.
- [38] Paul Pounds and Robert Mahony. *Small-scale Aeroelastic Rotor Simulation, Design and Fabrication*. Canberra, Australia, 2005.
- [39] Antonio DiCesare Kyle Gustafson Paul Lindenfelzer. Design optimization of a quad-rotor capable of autonomous flight. Master's thesis, Worcester Polytechnic Institute, 2009.
- [40] Samir Bouabdallah. Design and control of quadrotors with application to autonomous flying. Master's thesis, École Polytechnique Fédérale de Lausanne, 2007.
- [41] Find a motor. <http://www.flybrushless.com/search>, March 2011.
- [42] J. Peraire and S. Widnall. Mit open course on dynamics, 2008. Lecture L30 -3D Rigid Body Dynamics: Tops and Gyroscopes.
- [43] Ferdinand P. Beer, Jr. E. Russell Johnston, and John T. DeWolf. *Mechanical of Materials*. McGraw-Hill, 4th edition, 2006.
- [44] Matweb, material property data. <http://www.matweb.com/>, February 2011.
- [45] J. N. Reddy. *Mechanics of Laminated Composite Plates and Shells: Theory and Analysis of Materials*. CRC Press, 2th edition, 2003.
- [46] David Roylance. *Laminated Composite Plates*, 2000. Department of Materials Science and Engineering.
- [47] ANSYS Inc. Release 12.1 documentation for ansys, 2011.
- [48] J. N. Reddy. *Introduction to the Finite Element Method*. McGraw-Hill, 1993.

- [49] C. M. Wang, G. T. Lim, J. N. Reddy, and K. H. Lee. Relationships between bending solutions of reissner and mindlin plate theories. *Engineering Structures*, vol. 23:838–849, 2001.
- [50] H. E. Rosinger and I. G. Ritchie. n timoshenko’s correction for shear in vibrating isotropic beams. *Journal of Applied Physics*, vol. 10:1461–1466, 1977.
- [51] Rudolph Szilard. *Theory and Analysis of Plates: Classical and Numerical Methods*. Prentice Hall, 1974.
- [52] R. A. Serway and J. W. Jewett. *Physics for Scientists and Engineers*. Brooks Cole, 2004.
- [53] Yvonne T. Fuchs and Karen E. Jackson. Vertical drop testing and analysis of the wasp helicopter skid gear. *Journal of the American Helicopter Society*, 56(1), January 2011.
- [54] J. C. F. Pereira. *Mecânica dos fluidos computacional*. Instituto Superior Técnico, 2010.
- [55] Doug Jackson. *Aerodynamics of a helicopter rotor in forward flight*, 2000.
- [56] Wayne Johnson. *Helicopter theory*. Princeton University Press, 1980.

Appendix A

Centre of mass

A.1 ALIV

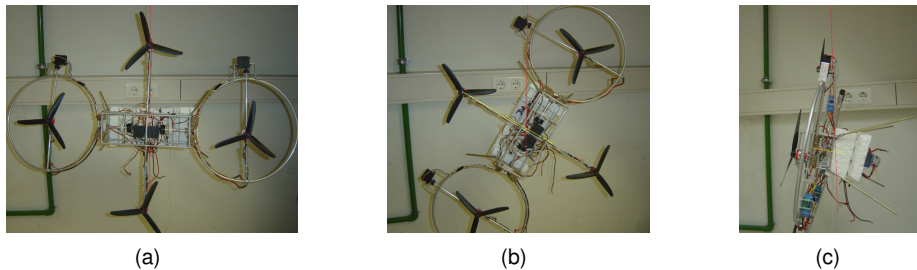


Figure A.1: Severino's ALIV centre of mass determination

This analysis gives the centre of mass coordinates as $x = 37.06mm$, $y = 9.88mm$ in relation to the arms intersection, and so very asymmetrical. The centre of mass' z coordinate is $z = 14.12$ below the main structure. The x , y and z directions respect the ABC frame.

A.2 ALIV3

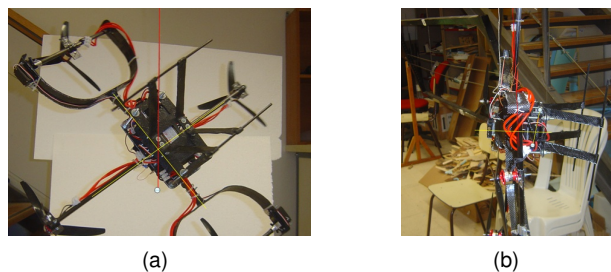


Figure A.2: ALIV3 centre of mass determination

The figures shows the symmetry of the ALIV3, with the x and y coordinates of the centre of mass in the arm's intersection. The z coordinate is located $45mm$ above the lower central board.

Appendix B

BEMT.m

```
%=====
% Implementacao da Blade Element Momentum Theory (BEMT)
%           Filipe Pedro – Maio de 2009
% Revised by: Nelson Fernandes – September 2011
%
% calls function: – C_drag.m and C_lift.m
%=====

clear all;
close all;
clc;

%===== DADOS GEOMETRICOS DO ROTOR: =====
inicio=tic;

%————— new code —————
%% PL = 0.133405 – Rotor optimo
c_tip=0.011260;
afil=0.331147;
theta_root=26.922121;
theta_tip=10.086238;
D=0.278796;
Nb=3;
v_rot_rpm=3879.928843;

root_cut_out=0.01; % porcao ocupada pelo hub e que nao contribui para a sustentacao [m]
R=D/2; % raio do rotor [m]
n_div=150; % numero de divisoes da pa
a_w=0.61; % parametro de contraccao de esteira
v_climb=0; % velocidade de subida [m/s]

v_rot_rads=v_rot_rpm*2*pi/60;
to_rad=pi/180;
to_deg=180/pi;

%===== PARAMETROS DA ATMOSFERA: =====
rho=1.225; % kg/m^2 (nos ensaios exp. foi 1.188)
mu=1.8e-5; % kg/(m s)

%————— end of new code —————

%===== DISTRIBUICOES DA CORDA, TORCAO E SOLIDEZ LOCAL: =====
```

```

r_max=1-(2e-5); % com tip-loss, para r=1 o lambda vem infinito...

dr=(r_max-root_cut_out/R)/n_div;
r=(root_cut_out/R):dr:r_max; r=r';

corda=zeros(n_div+1,1);
theta=zeros(n_div+1,1);
sigma_local=zeros(n_div+1,1);
Re=zeros(n_div+1,1);
for i=1:length(r)
    corda(i,1)=c_tip*(r(i,1)+(1-r(i,1))/afil); % c(r) linear
% corda(i,1)=(a_c*r(i,1)^4 + b_c*r(i,1)^3 + c_c*r(i,1)^2 + d_c*r(i,1) + e_c)/1000;
% divide-se por 1000 pq os coef foram calculados para c(r) em mm

    theta(i,1)=theta_tip*r(i,1)+theta_root*(1-r(i,1)); % torcao linear
% theta(i,1)=a_t*r(i,1)^4 + b_t*r(i,1)^3 + c_t*r(i,1)^2 + d_t*r(i,1) + e_t;

    sigma_local(i,1)=Nb*corda(i,1)/(pi*R);
    d_sigma_e=sigma_local(i,1)*r(i,1)^2*dr;
    Re(i,1)=rho/mu*v_rot_rads*(r(i,1)*R)*corda(i,1);
end

theta=theta*to_rad; % pq a dist. foi calculada em graus...

% ----- new code -----
%===== CALCULO DE PARAMETROS GEOMETRICOS DO ROTOR: =====
A_pa=sum(corda*dr)*R; % multiplica-se por R pq c(r) vai de 0 a 1.
A_disco=pi*R^2;
c_tip=corda(length(r));
c_root_cut_out=corda(1);
sigma_rotor=Nb*A_pa/A_disco; % ou sum(sigma_local*dr)
sigma_e=3*sum(d_sigma_e); % thrust weighted solidity

%===== CALCULO DO LAMBDA (INFLOW) (MAIS F, PHI E ALPHA): =====
v_tip=v_rot_rads*R;
lambda_c=v_climb/v_tip;

% Aproximacao inicial
Cla=2*pi;
F=ones(n_div+1,1);
lambda=zeros(n_div+1,1);
phi=zeros(n_div+1,1);
alpha=zeros(n_div+1,1);
CLA=zeros(n_div+1,1);
for i=1:length(r)
    F(i,1)=1;
    lambda(i,1)=(sqrt(16*a_w^2*lambda_c^2*F(i,1)^2+(16*a_w*Cla*r(i,1)*sigma_local(i,1)*theta(i,1)-8*a_w^2*
        Cla*lambda_c*sigma_local(i,1))*F(i,1)+a_w^2*Cla^2*sigma_local(i,1)^2)+4*a_w*lambda_c*F(i,1)-a_w*
        Cla*sigma_local(i,1))/(8*F(i,1));

    %Iterar.. 1
    phi(i,1)=lambda(i,1)/r(i,1);
    alpha(i,1)=theta(i,1)-phi(i,1);
    CLA(i,1)=C_lift(alpha(i,1)*to_deg,Re(i,1))/alpha(i,1);
    F(i,1)=(2/pi)*acos(exp(-Nb/2*((1-r(i,1))/lambda(i,1))));
    lambda(i,1)=(sqrt(16*a_w^2*lambda_c^2*F(i,1)^2+(16*a_w*CLA(i,1)*r(i,1)*sigma_local(i,1)*theta(i,1)-8*
        a_w^2*CLA(i,1)*lambda_c*sigma_local(i,1))*F(i,1)+a_w^2*CLA(i,1)^2*sigma_local(i,1)^2)+4*a_w*

```

```

        lambda_c*F(i,1)-a_w*CLA(i,1)*sigma_local(i,1))/(8*F(i,1));

%Iterar.. 2
phi(i,1)=lambda(i,1)/r(i,1);
alpha(i,1)=theta(i,1)-phi(i,1);
CLA(i,1)=C_lift(alpha(i,1)*to_deg,Re(i,1))/alpha(i,1);
F(i,1)=(2/pi)*acos(exp(-Nb/2*((1-r(i,1))/lambda(i,1))));
lambda(i,1)=(sqrt(16*a_w^2*lambda_c^2*F(i,1)^2+(16*a_w*CLA(i,1)*r(i,1)*sigma_local(i,1)*theta(i,1)-8*a_w^2*CLA(i,1)*lambda_c*sigma_local(i,1))*F(i,1)+a_w^2*CLA(i,1)^2*sigma_local(i,1)^2)+4*a_w*lambda_c*F(i,1)-a_w*CLA(i,1)*sigma_local(i,1))/(8*F(i,1));

%Iterar.. 3
phi(i,1)=lambda(i,1)/r(i,1);
alpha(i,1)=theta(i,1)-phi(i,1);
CLA(i,1)=C_lift(alpha(i,1)*to_deg,Re(i,1))/alpha(i,1);
F(i,1)=(2/pi)*acos(exp(-Nb/2*((1-r(i,1))/lambda(i,1))));
lambda(i,1)=(sqrt(16*a_w^2*lambda_c^2*F(i,1)^2+(16*a_w*CLA(i,1)*r(i,1)*sigma_local(i,1)*theta(i,1)-8*a_w^2*CLA(i,1)*lambda_c*sigma_local(i,1))*F(i,1)+a_w^2*CLA(i,1)^2*sigma_local(i,1)^2)+4*a_w*lambda_c*F(i,1)-a_w*CLA(i,1)*sigma_local(i,1))/(8*F(i,1));

end

%===== INTEGRACAO NUMERICA DE C.T, C_Pi E C_PO: =====
dCT=zeros(n_div+1,1);
dCPi=zeros(n_div+1,1);
dCPO=zeros(n_div+1,1);
for i=1:length(r)
    dCT(i,1) = F(i,1)*2/a_w*lambda(i,1)*(lambda(i,1)-a_w*lambda_c)*r(i,1)*dr;
    dCPi(i,1) = lambda(i,1)*dCT(i,1);
    dCPO(i,1) = sigma_local(i,1)/2*C_drag(alpha(i,1)*to_deg,Re(i,1))*(r(i,1))^3*dr;
end

C_T=sum(dCT);
C_Pi=sum(dCPi);
C_PO=sum(dCPO);
C_P=C_Pi+C_PO;

%————— end of new code —————
%===== CALCULOS DA PERFORMANCE: =====
disp('Performance: ')
k=C_Pi*sqrt(4*a_w)/C_T^(3/2);
FM=C_T^(3/2)/(sqrt(4*a_w)*C_P);

PL=C_T/(C_P*v_tip);
T=C_T*rho*A_disco*v_tip^2;
P=C_P*rho*A_disco*v_tip^3;
fprintf('Para V_rot = %d rpm:\nT = %f g\nT = %f N\nP = %f W\nPL = %f nCT = %f\nCP = %f\n',v_rot_rpm,T←
    /9.81*1e3,T,P,PL,C_T,C_P)
rpm=0:100:12000; rpm=rpm';
omega=rpm*2*pi/60;
for i=1:length(omega)
    PL_curva(i,1)=C_T/(omega(i,1)*R*C_P);
    T_curva(i,1)=C_T*rho*A_disco*R^2*omega(i,1)^2;
    P_curva(i,1)=C_P*rho*A_disco*R^3*omega(i,1)^3;
end
end

```

Appendix C

GA.m

```
%=====
%                               ALGORITMO GENETICO
%                               Filipe Pedro – Junho 2009
% Revised by: Nelson Fernandes – September 2011
% Cria os ficheiros: – ga_resultados.dat e ga_condicoes.dat
%=====

clear all
close all
clc

%===== PARAMETROS: =====
disp(round(clock))
disp('_____ALGORITMO-GENETICO_____')
n_gen=input('numero de geracoes = '); % numero maximo de geracoes
n_pop=input('tamanho da populacao = '); % numero de individuos na populacao
pop_keep=input('percentagem da pop. a manter [0:1] = '); % percentagem da populacao a manter
n_keep=round(pop_keep*n_pop);
fprintf('=> n_keep = %d\n',n_keep)
if mod(n_keep,2) % verificacao se n_keep par:
    disp('ERRO!!! \n Ajuste pop_keep ou n_pop de forma a n_keep ser par!')
    break
end
taxa_mut=input('taxa de mutacao [0:1] = '); % taxa de mutacao
disp('_____')
metodo_selec=menu('Metodo de Seleccao:', 'Ranking', 'Roulette Wheel', 'Torneio');
metodo_empar=menu('Metodo de Emparelhamento:', 'Adjacent Fitness Pairing', 'Best-Mate-Worst');
metodo_cross=menu('Metodo de Acasalamento:', 'Arithmetic Crossover', 'Intermediate Crossover');
disp('_____')
% vectores com os valores max e min dos parametros (param_1,param_2,...,param_n):
param=['c_tip'; 'lambda'; 't_root'; 'te_tip'; '__DD__'; '__Nb__'; 'rotrpm'];
tipo=['real'; 'real'; 'real'; 'real'; 'real'; 'intr'; 'real']; % todas estas strings tem de ter o mesmo ←
comprimento!!!
param_min=[0,0.3,0,0,0.1,2,2000];
param_max=[0.015,1,30,30,0.279,4,10000];
% restricoes:
T_min=4;
P_max=100;

if length(param_min)~=length(param_max)
    disp('limites de parametros mal introduzidos!')
    break
end
```

```

else
    n_param=length(param_min);
end
disp('Parametro: \t \tTipo:\tGama de valores possivel:\n')
for i=1:n_param
    fprintf('%s \t->\t%s\t[%f : %f]\n',param(i,:),tipo(i,:),param_min(i),param_max(i))
end

disp('_____')
disp('Restricoes:')
fprintf('T_min = %f\nP_max = %f\n',T_min,P_max)
disp('_____')

save('./ga_condicoes.dat','n_gen','n_pop','pop_keep','n_keep','taxa_mut','metodo_selec','metodo_empar',...
    'metodo_cross','param','n_param','tipo','param_min','param_max','T_min','P_max')

%===== ALGORITMO: =====
inicio=tic;
fprintf('\nNumero de avaliacoes a efectuar = %d\nTempo estimado para acabar (1s por avaliacao) = %5.1f ←
    horas\n',...
n_pop+n_gen*(n_pop-n_keep+n_pop*n_param*taxa_mut),(n_pop+n_gen*(n_pop-n_keep+n_pop*n_param*taxa_mut))←
    *1/60/60)
% constituicao da populacao inicial:
for i=1:n_param
    if strcmp(tipo(i),'real') % parametros reais
        pop_inicial(:,i)=(param_max(i)-param_min(i))*rand(n_pop,1)+param_min(i);
    else % parametros inteiros
        pop_inicial(:,i)=round((param_max(i)-param_min(i))*rand(n_pop,1)+param_min(i));
    end
end
disp('\nPopulacao inicial gerada...')

pop=fitness(pop_inicial,n_param,T_min,P_max); % calcula na ultima coluna a 'fitness' de cada cromossoma
disp('...e avaliada!')

% ciclo de geracoes:
fid=fopen('ga_resultados.dat','a');
versao=version;
fprintf(fid,'# Resultados do Algoritmo Genetico (corrido em Octave %s)\n# Geracao | Parametro-1 | ←
    Parametro-2 | ... | Fitness | Media.Geracao',versao)
disp('\nInicio do ciclo de Geracoes...\nProgresso:')
for gen=1:n_gen
    fprintf('%3.1f%% ',gen/n_gen*100)
    pais=seleccao(pop,n_keep,metodo_selec); % seleccao dos cromossomas para o 'mating'

    pais_empar=empar(pais,metodo_empar); % emparelhamento dos pais para o 'mating'

    filhos=crossover(pais_empar,n_pop,tipo,metodo_cross); % 'mating' dos pais
    filhos=fitness(filhos,n_param,T_min,P_max); % determinacao da 'fitness' dos filhos

    % mutacao dos filhos:
    [fit,indice]=min(filhos(:,n_param+1));
    filhos=mutacao(filhos,taxa_mut,tipo,param_min,param_max,T_min,P_max,indice);
% concatenacao dos pais com os filhos:
    pop_nova=pais;
    [dimx,auxxx]=size(filhos);
    for i=1:dimx
        for j=1:n_param+1

```

```

    pop_nova(i+n_keep,j)=filhos(i,j);
end
end
% mutacao total=0, para o codigo corresponder ao original
[fit,indice]=min(pop_nova(:,n_param+1));
pop=mutacao(pop_nova,0,tipo,param_min,param_max,T_min,P_max,indice);

% Determina o melhor e a media da geracao, e guarda no ficheiro ga_resultados.dat:
[fit,indice]=min(pop(:,n_param+1));
fprintf(fid,'\n%d ',gen);
fprintf(fid,'%f %f ',pop(indice,:),mean(pop(:,n_param+1)));
end

disp('\n Calculos concluidos! \n')
telapsed=toc(inicio);
horas=floor((telapsed)/60/60);
minutos=floor(((telapsed)/60/60-horas)*60);
segundos=round((((telapsed)/60/60-horas)*60-minutos)*60);
fprintf('\nO codigo demorou %f horas a correr (%d horas %d minutos %d segundos)\n',(telapsed)/60/60,←
    horas,minutos,segundos);
fprintf(fid,'\n# O codigo demorou %f minutos a correr (%d horas %d minutos e %d segundos)',(telapsed)/60,←
    horas,minutos,segundos);
fclose(fid);

%===== RESULTADOS: =====
disp('\nResultados Finais:\n')
for i=1:n_param
    fprintf('%s \t->\t%f \n',param(i,:),pop(indice,i))
end
fprintf('\nFitness Final = %f\n',pop(indice,n_param+1))

[PL,T,P,C_T,C_P]=f_BEMT(pop(indice,1),pop(indice,2),pop(indice,3),pop(indice,4),pop(indice,5),pop(indice←
    ,6),pop(indice,7),0.61,0,0.01);
fprintf('\nPL = %f\nThrust = %f\nPower = %f\nC_T = %f\nC_P = %f\n',PL,T,P,C_T,C_P);

```

Auxiliary functions

```

% FITNESS
function [m] = fitness(m,n_param,T_min,P_max)
[j,k]=size(m);
for i=1:j
    [PL,T,P]=f_BEMT(m(i,1),m(i,2),m(i,3),m(i,4),m(i,5),m(i,6),m(i,7),0.61,0,0.01);
    % penalizacao por thrust insuficiente:
    if (T<T_min || P>P_max)
        penalidade=0;
    else
        penalidade=1;
    end
    m(i,n_param+1)=-PL*penalidade;
end
end

% SELECCAO: (selecciona os cromossomas que se irao reproduzir)
function [escolhidos] = seleccao(pop,n_keep,metodo)
[linhas,colunas]=size(pop);
[s,indice]=sort(pop(:,colunas));
escolhidos(1,:)=pop(indice(1),:); % elitismo
if metodo==1 % OPCAO 1-> Seleccao por 'ranking'

```

```

    for i=2:n_keep
        escolhidos(i,:)=pop(indice(i),:);
    end
end
if metodo==2 % OPCAO 2-> Seleccao por 'Roulette Wheel'
    soma_fit=0;
    for i=1:n_keep
        soma_fit + abs(pop(i,colunas));
    end
    for i=2:n_keep
        num_rand=rand()*soma_fit;
        soma_parcial=0;
        idd=0;
        while soma_parcial<num_rand
            idd=idd+1;
            soma_parcial + abs(pop(idd,colunas));
        endwhile
        escolhidos(i,:)=pop(idd,:);
    end
end
end
if metodo==3 % OPCAO 3-> Seleccao por 'Torneio'
    for i=2:n_keep
        indiv_1=ceil(rand()*linhas);
        indiv_2=ceil(rand()*linhas);
        if pop(indiv_1,colunas)>pop(indiv_2,colunas)
            escolhidos(i,:)=pop(indiv_1,:);
        else
            escolhidos(i,:)=pop(indiv_2,:);
        end
    end
end
end
end

% EMPARELHAMENTO: (ordena as linhas para o 'mating' - pai,mae,pai,mae,...)
function [emparelhados] = empar(escolhidos,metodo)
if metodo==1 % OPCAO 1-> 'Adjacent Fitness Pairing'
    [linhas,colunas]=size(escolhidos);
    [s,indice]=sort(escolhidos(:,colunas));
    for i=1:linhas
        emparelhados(i,:)=escolhidos(indice(i),:);
    end
elseif metodo==2 % OPCAO 2-> 'Best mate-worst' (os melhores com os piores)
    j=0;
    [linhas,aux]=size(escolhidos);
    for i=1:2:linhas
        emparelhados(i,:)=escolhidos(i-j,:);
        emparelhados(i+1,:)=escolhidos(linhas-j,:);
        j=j+1;
    end
end
end
end

% CROSSOVER (acasalamento): (pega em cada par de pais e da origem a 2 novos cromossomas)
function [filhos] = crossover(pais,n_pop,tipo,metodo)
n_filhos=0;
i=1;
k=1;

```

```

[linhas, colunas]=size(pais);
while n_filhos < n_pop-linhas
    if metodo==1 % OPCAO 1-> 'Arithmetical Crossover'
        for j=1:colunas-1
            if strcmp(tipo(j,:), 'real') % parametros reais
                b=rand();
                filhos(k,j)=b*pais(i,j)+(1-b)*pais(i+1,j);
                filhos(k+1,j)=(1-b)*pais(i,j)+b*pais(i+1,j);
            else % parametros inteiros
                b=rand();
                filhos(k,j)=round(b*pais(i,j)+(1-b)*pais(i+1,j));
                filhos(k+1,j)=round((1-b)*pais(i,j)+b*pais(i+1,j));
            end
        end
        end
        [n_filhos, aux]=size(filhos);
        k=k+2;
        i=i+2;
        if i>linhas
            i=1;
        end
    elseif metodo==2 % OPCAO 2-> 'Intermediate Crossover'
        for j=1:colunas-1
            if strcmp(tipo(j,:), 'real') % parametros reais
                filhos(k,j)=pais(i,j)+rand()*(pais(i+1,j)-pais(i,j));
                filhos(k+1,j)=pais(i,j)+rand()*(pais(i+1,j)-pais(i,j));
            else % parametros inteiros
                filhos(k,j)=round(pais(i,j)+rand()*(pais(i+1,j)-pais(i,j)));
                filhos(k+1,j)=round(pais(i,j)+rand()*(pais(i+1,j)-pais(i,j)));
            end
        end
        end
        [n_filhos, aux]=size(filhos);
        k=k+2;
        i=i+2;
        if i>linhas
            i=1;
        end
    end
end
end

% MUTACAO:
function [pop]=mutacao(pop, taxa_mut, tipo, param_min, param_max, T_min, P_max, indice_melhor)
[linhas, colunas]=size(pop);
n_var_mut=round(linhas*(colunas-1)*taxa_mut);
for i=1:n_var_mut
    crom=ceil(rand()*linhas);
    param=ceil(rand()*(colunas-1));
    if strcmp(tipo(param,:), 'real') % parametros reais
        pop(crom, param)=(param_max(param)-param_min(param))*rand()+param_min(param);
    else % parametros inteiros
        pop(crom, param)=round((param_max(param)-param_min(param))*rand()+param_min(param));
    end
    end
    pop(crom,:)=fitness(pop(crom,:), colunas-1, T_min, P_max);
end
end

```

Appendix D

Tested aerofoils

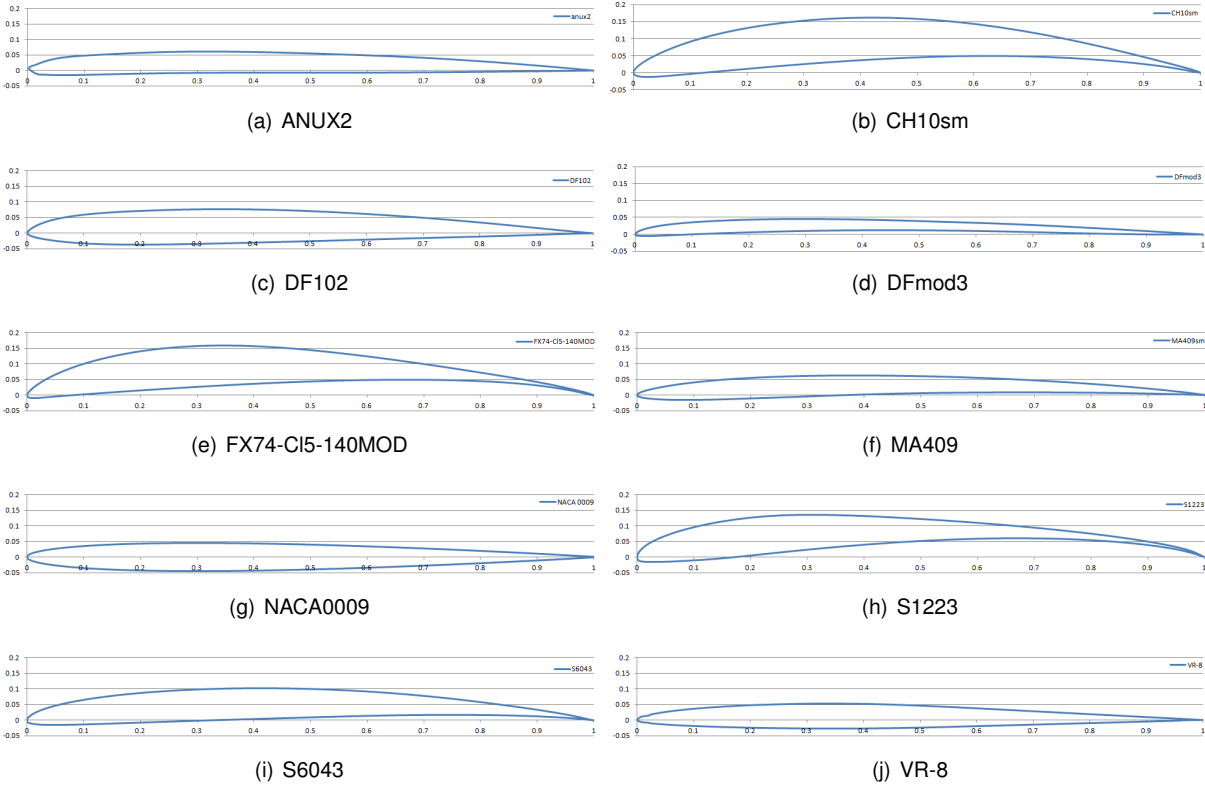


Figure D.1: Tested aerofoils

Appendix E

Servo calculations

Rotation from the inertial frame (X, Y, Z) to the intermediate frame (x', y', z') :

$$\begin{Bmatrix} x' \\ y' \\ z' \end{Bmatrix} = \begin{bmatrix} \cos \phi & \sin \phi & 0 \\ -\sin \phi & \cos \phi & 0 \\ 0 & 0 & 1 \end{bmatrix} \begin{Bmatrix} X \\ Y \\ Z \end{Bmatrix} = [\tilde{T}_1] \begin{Bmatrix} X \\ Y \\ Z \end{Bmatrix} \quad (\text{E.1})$$

Rotation from intermediate frame (x', y', z') to the body-fixed frame (x'', y'', z'') :

$$\begin{Bmatrix} x'' \\ y'' \\ z'' \end{Bmatrix} = \begin{bmatrix} 1 & 0 & 0 \\ 0 & \cos \theta & \sin \theta \\ 0 & -\sin \theta & \cos \theta \end{bmatrix} \begin{Bmatrix} x' \\ y' \\ z' \end{Bmatrix} = [\tilde{T}_2] \begin{Bmatrix} x' \\ y' \\ z' \end{Bmatrix} \quad (\text{E.2})$$

Angular velocities and accelerations, and inertia tensors.

Angular derivatives	U-arm	Slim-arm
$\dot{\psi} = 1220.5 \text{rad.s}^{-1}$	$I_{xx} = 8.785 \times 10^{-3} \text{Kg.m}^2$	$I_{xx} = 6.623 \times 10^{-3} \text{Kg.m}^2$
$\ddot{\psi} = 20000 \text{rad.s}^{-2}$	$I_{xy} = -5.917 \times 10^{-5} \text{Kg.m}^2$	$I_{xy} = 0 \text{Kg.m}^2$
$\dot{\theta} = 7.48 \text{rad.s}^{-1}$	$I_{xz} = -0.113 \times 10^{-5} \text{Kg.m}^2$	$I_{xz} = -0.879 \times 10^{-5} \text{Kg.m}^2$
$\ddot{\theta} = 100 \text{rad.s}^{-2}$	$I_{yy} = 2.939 \times 10^{-3} \text{Kg.m}^2$	$I_{yy} = 0.347 \times 10^{-3} \text{Kg.m}^2$
$\dot{\phi} = 7.48 \text{rad.s}^{-1}$	$I_{yz} = 0 \text{Kg.m}^2$	$I_{yz} = 9.318 \times 10^{-5} \text{Kg.m}^2$
$\ddot{\phi} = 100 \text{rad.s}^{-2}$	$I_{zz} = 9.635 \times 10^{-3} \text{Kg.m}^2$	$I_{zz} = 7.629 \times 10^{-3} \text{Kg.m}^2$

Table E.1: Inertia and angular derivatives for maximum servo torque estimation

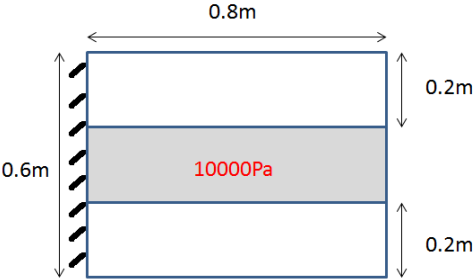
Appendix F

Analytical determination for laminated composites displacement

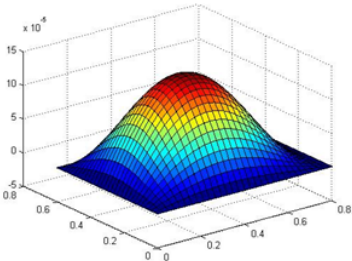
Theoretical displacement for a laminated plate with a $[0_2/90_2/\pm 30^\circ/\pm 45^\circ]_s$ layup. Every laminae has the same thickness and the laminate thickness is $20mm$.

$$\begin{matrix} E_L & = & 60GPa \\ G_{LT} & = & 12GPa \end{matrix} \left| \begin{matrix} E_L & = & 24.8GPa \\ G_{TL} & = & 12GPa \end{matrix} \right. \begin{matrix} \nu_{LT} & = & 0.23 \\ \rho & = & 1500Kg.m^{-3} \end{matrix}$$

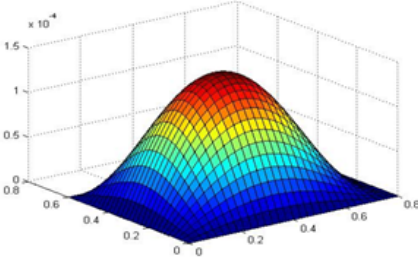
The plate has $0.8 \times 0.6m$ and is subjected to $10000Pa$ and is clamped in one edge and simply supported in the other three (figure F.1(a)).



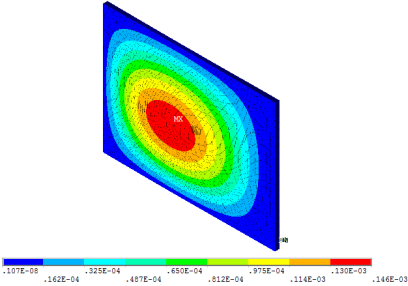
(a) Plate geometry and load position



(b) Levy maximum deformation of $0.14272mm$ in $(x = 0.347mm, y = 0.300mm)$



(c) Rayleigh-Ritz maximum deformation of $0.14244mm$ in $(x = 0.347mm, y = 0.300mm)$



(d) ANSYS® maximum deformation of $0.14618mm$ in $(x = 0.347mm, y = 0.300mm)$

Figure F.1: Laminate plate theoretical analysis

Appendix G

Detailed weight of every component

U-arm

Component	Theoretical model			Real model		
	weight [g]	quantity	total weight [g]	weight [g]	quantity	total weight [g]
M6 screw	15	4	60	15	4	60
M6 nut	2	8	16	2	8	16
M6 washer	2.5	12	30	2.5	12	30
M3 screw	0.5	56	28	0.5	56	28
M3 nut	0.2	56	11.2	0.2	56	11.2
M3 washer	0.25	96	24	0.25	96	24
Central board	35.512	2	71.024	27	2	54
Embrancing plate	3.5	4	14	3.5	4	14
U-arm	63.892	2	127.784	58.5	2	117
Skirt socket	3	4	12	3	4	12
Carbon socket	1	2	2	1	2	2
Bearings	9.5	4	38	9.5	4	38
Servo board	22.543	1	22.543	28	1	28
Electronic board	38.509	1	38.509	21	1	21
Bearing support	5	4	20	5	4	20
Bearing board	9	1	9	9	1	9
Landing gear	30.792	2	61.584	31	2	62
Rotor	11	4	44	11	4	44
Motor	71	4	284	71	4	284
Servo	37.2	4	148.8	37.2	4	148.8
ESC	22	4	88	22	4	88
Ardupilot	60.7	1	60.7	60.7	1	60.7
GPS	8	1	8	8	1	8
magnetometer	5	1	5	5	1	5
Xbee	11	1	11	11	1	11
Battery	404	1	404	404	1	404
PDB	9.5	1	9.5	9.5	1	9.5
Component	$\rho \times Area [g.mm^{-1}]$	Length [mm]	total weight [g]	$\rho \times Area [g.mm^{-1}]$	Length [mm]	total weight [g]
Carbon tubes	0.027975	1316	36.8151	0.027975	1316	36.8151
Cabling	0.017	5000	85	0.017	5000	85
Carbon rods	0.031915	560	17.8724	0.031915	560	17.8724
Total		1788.33g			1749g	

Table G.1: U-arm model detailed weight

slim-arm

Component	Theoretical model			Real model		
	weight [g]	quantity	total weight [g]	weight [g]	quantity	total weight [g]
M6 screw	15	4	60	15	4	60
M6 nut	2	8	16	2	8	16
M6 washer	2.5	12	30	2.5	12	30
M3 screw	0.5	56	28	0.5	56	28
M3 nut	0.2	56	11.2	0.2	56	11.2
M3 washer	0.25	96	24	0.25	96	24
Central board	35.512	2	71.024	27	2	54
Embrancing plate	3.5	4	14	3.5	4	14
Servo support	6.882	2	13.764	6	2	12
Elbow	2	6	12	2	6	12
Skirt socket	3	4	12	3	4	12
Carbon socket	1	2	2	1	2	2
Bearings	9.5	4	38	9.5	4	38
Servo board	22.543	1	22.543	28	1	28
Electronic board	38.509	1	38.509	21	1	21
Bearing support	5	4	20	5	4	20
Bearing board	9	1	9	9	1	9
Landing gear	30.792	2	61.584	31	2	62
Rotor	11	4	44	11	4	44
Motor	71	4	284	71	4	284
Servo	37.2	4	148.8	37.2	4	148.8
ESC	22	4	88	22	4	88
Ardupilot	60.7	1	60.7	60.7	1	60.7
GPS	8	1	8	8	1	8
magnetometer	5	1	5	5	1	5
Xbee	11	1	11	11	1	11
Battery	404	1	404	404	1	404
PDB	9.5	1	9.5	9.5	1	9.5
Component	$\rho \times Area [g.mm^{-1}]$	Length [mm]	total weight [g]	$\rho \times Area [g.mm^{-1}]$	Length [mm]	total weight [g]
Carbon tubes	0.027975	1460	40.8435	0.027975	1460	40.8435
Cabling	0.017	5000	85	0.017	5000	85
Carbon rods	0.031915	560	17.8724	0.031915	560	17.8724
Total		1690.34g			1660g	

Table G.2: Slim-arm model detailed weight